Zeeman Measurements using SO(1_0–0_1) Transition

and

Heterodyne Observations towards the W51 Region

Dissertation

zur

Erlangung des Doktorgrades (Dr. rer. nat.)

der

Mathematisch-Naturwissenschaftlichen Fakultät

der

Rheinischen Friedrich-Wilhelms-Universität Bonn

vorgelegt von

Chau Ching CHIONG

aus

Taipeh, Taiwan

Bonn, September 2003

Angefertigt mit Genehmigung der Mathematisch-Naturwissenschaftlichen Fakultät der Rheinischen Friedrich-Wilhelms-Universität Bonn

1. Referent: Prof. Dr. K. M. Menten
2. Referent: Prof. Dr. U. Klein

Tag der Promotion:

Dedicated to my parents.

Abstract

Understanding the star-forming procedure is one of the most important topic in astrophysics. One of the most unexplored fields in the star-forming theories is magnetic field. Magnetic field is believed to play an important role in regulating the rate of star formation. Among various means of measurements, Zeeman effect is the only direct way to measure the magnetic field strength in the interstellar medium. In the first part of the thesis, Zeeman measurements using the SO(1_0-0_1) transition is chosen to probe magnetic fields towards the dense region. To my knowledge, this is the first attempt to measure the Zeeman effect with this transition. With the latest microwave technology, we set up a receiver aiming at the Zeeman observation with this specific transition. The theories and complete procedure, including the preparatory works, the instrumentation, the difficulties in the measurements, and the data reduction are described in detail in the thesis. Though we detect the magnetic field strength of -2.1 ± 1.5 mG (3σ) after 45.5 hours integration towards DR21(OH) region, we cannot identify the originating cloud of the field. Towards the Orion B region, we can only derive the upper limit.

Magnetic fields can regulate the star formation rate via ambipolar diffusion. This procedure separates the ionized and neutral materials in the interstellar medium. The study of the photodissociation regions (PDRs) is thus another important topic to understand the star formation. In the latter part of the thesis, the CO(4-3) and CI($^3P_1$-$^3P_0$) data of the massive star-forming region W51 using the CHAMP array receiver at the CSO is presented. We separated the complex structure into at least four velocity components. The CO(4-3) line is highly optically thick. Towards the W51**d** dense region, the kinetic temperature is constrained between 65 to 80 K and CO column density between 1 to 2.5×10^{19} cm^{-2} using the LVG approximation for the density range of $n(H_2) = 10^4$ to 10^5 cm^{-3}. The correlation of CI and ^{13}CO is not as striking as other cases. Strong CI emission is found even deep in the cloud cores. It cannot be explained by a single parallel layer PDR model, therefore a time-dependent chemistry model is introduced. The W51 region provides a precious example for the study of PDRs with large areas and large ranges of intensity.

Contents

Chapter 1 Introduction

1.1 Outline of the thesis

In the thesis there are two parts. The first part deals with the Zeeman measurements using the SO(1_0-0_1) transition. The whole procedure will be described in chapter 2 and 3. Chapter 2 describes a preparatory survey of the SO(1_0-0_1) line in order to select the best candidates and positions for the Zeeman measurements. The results on over 50 sources are shown in §2.2. In §2.3 and §2.4, nine sources are selected for further investigations. The Zeeman measurements are presented in chapter 3. The theory, the instrumentation and main difficulties of Zeeman measurements are described in §3.1, §3.2 and §3.3. The data on DR21(OH) and Orion B region are shown and discussed in §3.4.

The second part contains data on the W51 region obtained using CHAMP. After a short introduction in §4.1, the CO(4-3) and CI($^3P_1$-$^3P_0$) observational results are shown in §4.2. The morphology and disussion of the W51 giant molecular cloud are presented in §4.3 and §4.4. In Chapter 5 is a summary of the thesis and future works.

1.2 Magnetic field and star formation

The star formation process is one of the most important topics in modern astrophysics. Though there are still many remaining puzzles in the whole scenario, magnetic fields are believed to play a significant role in the evolution of molecular clouds in most theories of star formation (Mestel & Spitzer, 1956; Mestel, 1966; Mouschovias, 1987; McKee et al., 1993; Shu et al., 1999; and many others). Magnetic fields enter in the theories through the magnetic support of molecular clouds against gravitational collapse, dissipation of angular momentum in accretion disks, and generation of jets and outflows (see reviews by McKee et al., 1993; Mouschovias & Ciolek, 1999).

The magnetic field was first investigated in the context of the star-forming process by Mestel & Spitzer (1956). Strittmatter (1966) calculated the critical mass for gravitational collapse perpendicular to magnetic field. Again ten years later, Mouschovias (1976) carried out the first self-consistent numerical studies of self-gravitating magnetic clouds. In the elemental model of star formation, a non-rotating, non-magnetized, isothermal cloud will collapse from the inside out at the local sound speed due to gravitational force, if the mass of the molecular cloud is more than the critical mass set by Ebert (1955) and Bonner (1956) (Shu, 1977). But the observed low star formation efficiency in molecular clouds shows that there should be some mechanisms in addition to thermal pressure, e.g. rotation, turbulence or magnetic fields, to support the molecular clouds from gravitational collapse and regulate the star formation efficiency. From the observations, rotational rates are too small to support clouds (Myers et al., 1991). The source of supersonic hydrodynamical turbulence is not yet clearly identified, probably from the winds of low-mass stars that form indside clumps (Bertoldi & McKee, 1996). Magnetic fields, however, give the best theoretical explanation. They can support the cloud through magnetohydrodynamical (MHD) waves, and observed field strengths in molecular clouds are large enough to support this scenario. A solution to the problems of conservation of angular momentum and magnetic flux in the collapsing core may be magnetic braking and ambipolar diffusion. Magnetic braking can transfer angular momentum into the ambient medium. The

ambipolar diffusion separates the ionized and neutral gas. The magnetic flux remains mainly in the ionized gas in the envelope so that the neutral gas can contract to form new stars. In theory, outflows accelerated by magnetic field can also transfer angular momentum by losing material (McKee et al., 1993; Shu et al., 1995; Mouschovias & Ciolek, 1999).

1.3 Observation and theory

There are two promising ways to observe magnetic fields. The first is by observing linear polarization of radiation in both thermal dust emission and molecular spectral lines. The former is produced by aligned interstellar dust grains. Elongated interstellar dust grains will be aligned with their minor axes parallel to the magnetic field and dust grains emit excess thermal radtional in the direction perpendicular to the field. It traces the direction of the magnetic field structure projected onto the plane of the sky (David & Greenstein, 1951). In the latter case, the molecule must be immersed in an anisotropic radiation field or the rate of radiative transitions must be at least comparable with the rate of collisional transitions (Goldreich & Kylafis, 1981, 1982). It also provides the plane-of-the-sky component of the magnetic field. Successful observations demonstrate the capability and reliability of polarization measurements (Greaves, 1999; Girard et al, 1999; Lai et al., 2001; Matthews et al., 2002; Siringo, 2003).

The second one is via the Zeeman effect. It arises from the coupling of an atom's or a molecule's magnetic moment with an external magnetic field. The elliptically polarized components are used to detect the magnetic field. For small splitting, only the line-of-sight component of the magnetic field can be derived. Only few molecules are suitable for Zeeman measurements. First successful detections were made 35 years ago using the HI 21cm line (Verschuur, 1968). Most measurements towards the interstellar medium are restricted to low to moderate densities with HI and OH transitions (Crutcher et al., 1999; Brogan & Troland, 2001; Crutcher et al., 1993) or to very high densities with OH and H_2O masers (Brogan et al., 2000; Fiebig & Güsten, 1989). Successful measurements on the dense core gas using suitable molecules like CSS, CN, and SO are still rare (see review by Crutcher, 1999). However, it is exactly this density range ($n \sim 10^3$ to 10^6 cm^{-3}) where most important mechanisms predicted by star-forming theories take place. Without the knowledge of the magnetic field in this range, one cannot test the existing model predictions.

Though magnetic fields are very important in star formation theories, the observational data on its magnitude remains quite restricted. The main problem is that magnetic fields can be measured only by polarized radiation. This detection requires very high sensitivity. Limitations in the instrumentation make high resolution observations towards collapsing cores unfeasible. Without a reliable data base of magnetic field strengths towards star forming regions, we cannot set enough constraints on the physical parameters in different stages of the star formation. In order to understand the physics of the relatively late star formation process and verify against existing models, it is necessary to measure the actual magnetic field strength in those dense molecular cloud cores. The results of measurements of magnetic fields can be checked with the star formation theories in several ways (Crutcher, 1999):

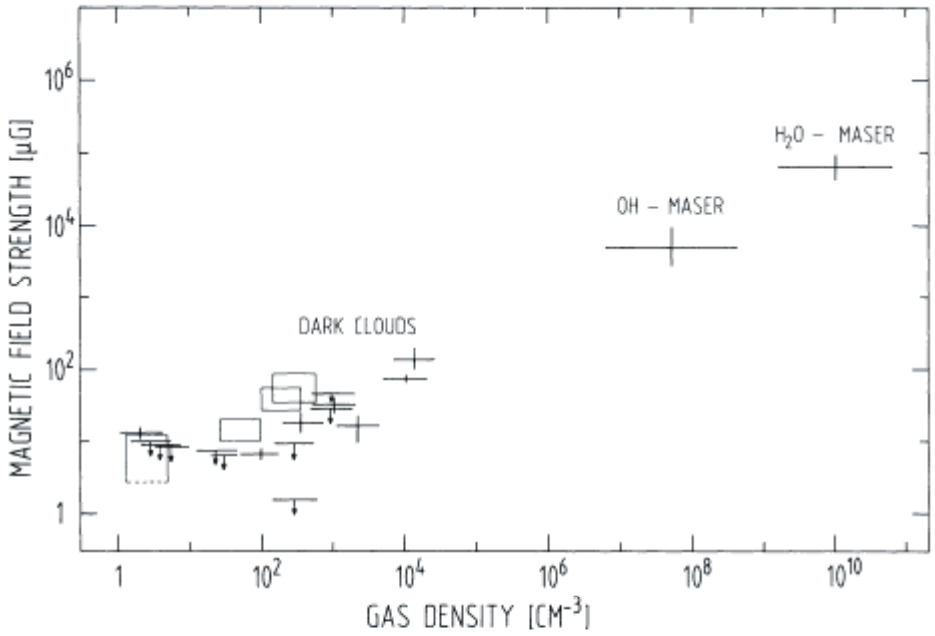

Fig. 1.1. Magnetic field strength $|B|$ vs. density ρ compiled by Fiebig & Güsten (1989). $|B| \sim \rho^{0.5}$.

(1) Alfvén waves and magnetic pressure

From the observational data, the internal cloud velocities are usually supersonic. With the data of magnetic field strengths by observations, one can first check if supersonic motions in the molecular clouds are Alfvénic (Shu, 1992). Outwardly propagating Alfvén waves provide support against gravity. The ratio of thermal to magnetic pressures is a very important parameter in star formation theories, since it affects the structure and evolution of magnetic clouds (Gammie & Ostriker, 1996).

(2) The B - ρ relation

From the predictions from star formation theories, the gas density ρ and magnetic field strength $|B|$ are related by a power law, $|B| \propto \rho^{\kappa}$. With different coefficient κ, one can verify the importance of the magnetic field in the star formation process. From star formation theory developed by Mouschovias (1985), κ is between 1/3 and 1/2 for the cores of contracting, self-gravitating, isothermal clouds with a frozen-in magnetic field.

Fig. 1.1 shows the magnetic field strength versus density compiled by Fiebig & Güsten (1989). They derive a relation $|B| \sim \rho^{0.5}$. But this figure might also mislead us, because the relation only applies to limited cases as described by Mouschovias (1985). For example, the main-line (1665 and 1667 MHz) and satellite-line (1620 MHz) OH maser are associated with HII regions and stars with strong emission in the infrared, respectively. These data from maser observations reveal the role of magnetic fields in processes which follow star formation, but not during star formation (Mouschovias, 1987). The data from diffuse clouds should also be excluded because they are generally not gravitationally bound.

In view of this, Crutcher (1999) reviewed 15 detections of Zeeman measurements in molecular clouds. He selected only the ones in dense regions. With linear regression analysis, the

relation between B_{los} and n is $B_{los} \propto \rho^{0.47 \pm 0.08}$ (Fig. 1.2; Fig.1 in Crutcher, 1999). It seems that the observational data until now are in good agreement with existing models and may exclude the case of $\kappa = 1/3$. But the data are still quite sparse.

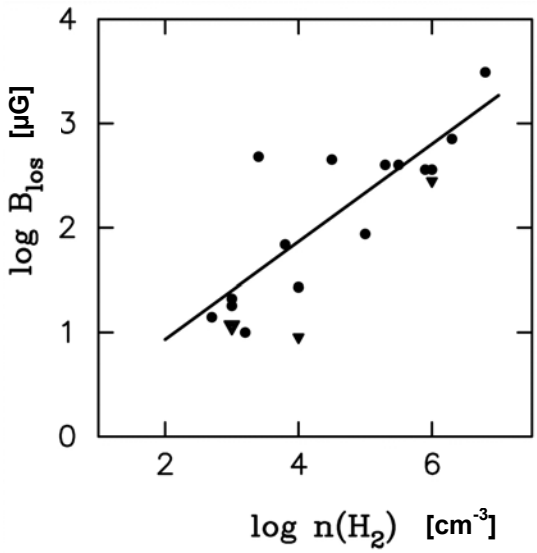

Fig. 1.2. Line-of-sight magnetic field strength vs. cloud density in the dense cores compiled by Crutcher (1999).

(3) The mass-to-flux ratio (M/Φ_B)

This parameter defines to what extent a static magnetic field can support a cloud against gravitational collapse. Mouschovias & Spitzer (1976) derived an expression for the critical value of the ratio, $M/\Phi_B = 0.126/(G)^{0.5}$ for a disk with only thermal support along the field lines, where G is the gravitational constant. With this value, the clouds can be devided into two types. A cloud with initial mass smaller than the critical mass is magnetically subcritical. It can never undergo graviational collapse. A cloud with initial mass larger than the critical mass is magnetically supercritical. It will collapse on relatively short time scales. The evolution of these two types of clouds is quite different. Shu et al. (1987) suggest that magnetically subcritical clouds are associated with low-mass star formation, whereas magnetically supercritical clouds preferentially form high mass stars.

(4) Virial equation and molecular cloud evolution

The virial expressions for the gravitational, kinetic and magnetic energy can be written as $\mathcal{W} = (3/5)aGM^2/R$, $\mathcal{T} = (3/2)M\sigma^2$, and $\mathcal{M} = (1/3)b\,|B|^2R^3$, where a, b are coefficients related to the cloud morphology. At the critical M/Φ_B value in the models, $\mathcal{M} / \mathcal{W} \sim 1$. With virial equation and measured magnetic field strength, one can access the relative importance of $\mathcal{W}$, $\mathcal{T}$ and $\mathcal{M}$ (Tomisaka et al. ,1988; McKee et al., 1993).

1.4 Zeeman measurements using the SO(1_0-0_1) transition

With state-of-the-art technology, it is now possible to perform high efficiency linear polarized mapping using bolometer arrays (Siringo, 2003) and with low noise receivers for Zeeman measurements. The main goal of the first part of this thesis is to show that the SO(1_0-0_1) line is a promising tool for Zeeman measurements and an attempt to increase the available data base by using this line towards the dense core regions. To my knowledge, this is the first time that this transition is used for Zeeman measurements.

1.5 The photodissociation region

Another important topic in star formation research is the study of photodissociation regions (PDRs). PDRs would regulate star formation via ionization and ambipolar diffusion. Systemetic research on PDRs started in the mid-1980 (Tielens & Hollenbach, 1985). PDRs include all interstellar regions where the gas is predominantly neutral but where far-ultraviolet (FUV, 6 eV to 13.6 eV) photons play a significant role in the chemistry and/or the heating. All of the atomic and most of the molecular gas in the Galaxis in PDRs, and they include most of the mass of the interstellar medium (Hollenbach & Tielens, 1997). Emission from PDRs caused by the photons are very important tools for diagnosing the physical conditions towards these regions.

Carbon is the fourth abundanct element in the interstellar medium after hydrogen, helium and oxygen. CO is arguably the most important molecule in astrophysics. Although H_2 is the most abundant molecule in the interstellar medium, CO is more readily observed and has been used extensively as a tracer of molecular gas and star-forming regions. In PDRs, the FUV photons will ionize CO molecules into atomic carbon (C) and oxygen (O), and then ionize atomic carbon to ionized carbon (C^+). Because the dissociation energy of CO is close to the ionization energy of C, the PDR model predicts that there should be a sharp transition layer from CO via C to C^+ (CO/C/C^+) in PDRs (Tielens & Hollenbach, 1985).

Observations of PDRs are often carried out in the far-infrared and sub-millimeter regimes. The rotational lines of CO, and fine-structure lines of [OI] and [CII] are the main coolants of PDRs. For carbon-bearing species, the [CI] 609 μm line has been detected 20 years ago (Phillips et al., 1980; Phillips & Huggins, 1981). A close association between CI emission and PDRs was confirmed towards many sources like the Orion Bar, S140, M17SW (Tauber et al., 1995; Minchin et al., 1993; Keene et al., 1996). PDR models with clumpy structure explained successfully the atomic carbon abundance towards them (Stutzki et al., 1988; Meixner & Tielens, 1993). The fact that [CI] emission often correlates with ^{13}CO low-J emission in spatial extent and line profile may also indicate that the surfaces of PDRs are clumpy (Keene et al., 1996). With clumpy structure and photoionization, the PDRs would regulate star formation via ambipolar diffusion, because the ambipolar diffusion rate strongly depends on the ionization rate (McKee, 1989).

Together with the [CI] 609 μm emission, the CO(4-3) line is also relatively unexplored. CO(4-3) generally traces the warm (T ~ 50 K) and dense (n ~ 10^5 cm^{-3}) region of the molecular clouds. With the new CHAMP (Carbon Heterodyne Array of the MPIfR. Güsten et al., 1998) array at the Caltech Submillimeter Observatory (CSO) covering CO(4-3) and CI($^3P_1$-$^3P_0$) transitions, it provides a very promising tool to investigate the kinematics and morphology towards the star-forming regions. In the second part of the thesis, the results on the W51 giant molecular cloud are presented.

References

Bonner, W. B., 1956, MNRAS, 116, 351.
Brogan, C. L., and Troland, T. H., 2001, ApJ, 550, 799.
Brogan, C., Frail, D. A., Goss, W. M., Troland, T. H., 2000, ApJ, 537, 875.
Crutcher, R. M., 1999, ApJ, 520, 706.
Crutcher, R. M., Roberts, D. A., Troland, T. H., Goss, W. M., 1999, ApJ, 515, 275.
Crutcher, R. M., Troland, T. H., Goodman, A. A., Heiles, C., Kazès, I., Myers, P. C., 1993, ApJ, 175.
David, L. Jr., Greenstein, J. L., 1951, ApJ, 114, 206.
Ebert, R. 1955, Zs. Ap., 217.
Fiebig, D., Güsten, R., 1989, A&A, 214, 333.
Gammie, C. F., Ostriker, E. C., 1996, ApJ, 466, 814.
Girard, J. M., Crutcher, R. M., Rao, R., 1999, ApJ, 525, 109.
Goldreich, P., Kylafis, N. D., 1981, ApJ, 243, 75.
Goldreich, P., Kylafis, N. D., 1982, ApJ, 253, 606.
Greaves, J. S., Holland, W. S., Friberg, P., Dent, W. R. F., 1999, ApJ, 512, L139.
Güsten, R., Ediss, G., Gueth, F., Gundlach, K., Hauschildt, H., Kasemann, C., Klein, T,, Kooi, J., Korn, A., Kramer, I., Leduc, R., Mattes, H., Meyer, K., Perchtold, E., Pilz, M., Sachert, R., Scherschel, M., Schilke, P., Schneider, G., Schraml, J., Skaley, D., Stark, R., Wetzker, W., Wiedenhöver, H., Wiedenhöver, W., Wongsowijoto, S., Wyrowski, F., 1998, Proc. SPIE Vol. 3357, p. 167, Ed. Thomas G. Phillips.
Hollenbach, D. J., Tielens, A. G. G. M., 1997, Annu. Rev. Astron., Astrophys., 35, 179.
Keene J., Lis D.C., Phillips T.G., Schilke P., in *Molecules in astrophysics: probes & processes*: abstract book, IAU symposium 178: 1-5 July 1996, Leiden, The Netherlands. Edited by Ewine Fleur van Dishoeck, pp. 129.
Lai, S.-P., Crutcher, R. M., Girard, J. M., Rao, R., 2001, 561, 864.
Matthews, B. C., Fiege, J. D., Moriarty-Scieven, G., 2002, ApJ, 569, 304.
Matthews, B. C., Wilson, C. D., 2002, ApJ, 574, 822.
McKee, C. F., 1989, ApJ, 345, 782.
McKee, C. F., Zweibel, E. G., Goodman, A., A., Heiles, C., 1993, in *Protostars and Planets III*, ed. E.H. Levy & J. I. Lunine, 327.
Meixner, M., Tielens, A. G. G. M., 1993, ApJ, 405, 216.
Mestel, L., Spitzer, L., 1956, MNRAS, 116, 503.
Mestel, L., 1966, MNRAS, 133, 265.
Minchin, N. R., White, G. J., Padman, R., 1993, A&A, 277, 595.
Mouschovias, T. Ch., Spitzer, L., Jr., 1976, ApJ, 210, 326.
Mouschovias, T., Ch., 1985, A&A, 142, 41.
Mouschovias, T. Ch. 1987, in *Physical Processes in Interstellar Clouds*, ed.: G. E. Morfill and M. Scholer, 453.
Mouschovias, T. Ch., Ciolek, G. E., 1999, in *The Origin of Stars and Planetary Systems*, ed. C.J. Lada & N. D., Kylafis, Dordrecht: Kluwer, pp. 305-339.
Myers, P. C., Goodman, A. A., 1991, ApJ, 373, 509.
Phillips, T. G., Huggins, P., Kuiper, T., Miller, R., 1980, ApJ, 238, 103.
Phillips T.G., Huggins P.J., 1981, ApJ, 251, 533.
Shu, F. H., 1977, APJ, 214, 488.
Shu, F. H., Adams, F. C., Lizano, S., 1987, ARA&A, 25, 23.
Shu, F. H., 1992, in *Gas Dynamics*, University Science Books, pp. 302-316.

Shu, F. H., Najita, J., Ostriker, E. C., Shang, H., 1995, ApJ, 455, L155.
Shu, F. H., Allen, A., Shang, H., Ostriker, E. V., Li, Z.-Y., 1999, in *The Origin of Stars and Planetary Systems*, ed. C. J. Lada and N. D., Kylafis, pp.193-226.
Siringo, G., PhD thesis, Universität Bonn, 2003.
Stritmatter, P. A., 1966, MNRAS, 132, 359.
Stutzki J., Stacey G.J., Genzel R., Harris A.I., Jaffe D.T., Lugten J.B., ApJ, 332, 379, 1988.
Tauber, J. A:, Lis, D. C., Keene, J., Schilke, P, Büttgenbach, T. H., 1995, A&A, 297, 567.
Tielens A.G.G.M., Hollenbach D., ApJ, 291, 722, 1985.
Tomisaka, K., Ikeuchi, S., Nakamura, T., 1988, ApJ, 335, 239.

Chapter 2 Sulphur Monoxide 30 GHz line Survey

In this chapter, an extented survey for emission of the 30 GHz SO $J_K = (1_0\text{-}0_1)$ transition carried out in Effelsberg is described. This is preparatory work for the following Zeeman measurements. In the Zeeman measurements, high intensity and narrow linewidth are preferred, and the source maps obtained in this survey will help us to locate the best positions. Together with existing 13 GHz SO $J_K = (1_2\text{-}1_1)$ line data, one can roughly estimate the densities and temperature towards these sources with the rotational diagram and LVG (large velocity gradient) methods. The information is very important when discussing the role that the magnetic field plays in these clouds if we detect it. Furthermore, since SO emission is generally believed to be enhanced in shock regions, this survey could also help us to learn about the kinematics in these regions.

2.1 Sulphur monoxide – the molecule

The ground electronic state of SO is $X^3\Sigma^-$, each rotational level is split into three spin states, corresponding to the three possible orientations of the electron-spin. The first six spectral transitions of the gaseous free radical sulphur monoxide were measured in the millimeter-wave region between 99 and 160 GHz by Winnewisser et al. (1964). This also marked the beginning of free radical spectroscopy in the millimeter wave region. Tiemann (1974) expanded the microwave measurements to the isotopomers. The molecular constants of $^{32}S^{16}O$ and $^{34}S^{16}O$ from Tiemann (1974) are summarized in Table 2.1.

Table 2.1 Molecular constants of sulphur monoxide.

		$^{32}S^{16}O$	$^{34}S^{16}O$
Rotational constant	**B_0 (MHz)**	21523.5612	21102.7219
Quartic centrifugal distorsion constant	**D_0 (MHz)**	0.034207	0.032877
Electron spin-spin coupling constant	**λ_0 (MHz)**	158258.66	158260.62
Electron spin-rotational coupling constant	**γ_0 (MHz)**	-168.794	-166.178
Dipole moment	**μ (Debye)**	1.55	1.55
g-factor of the electron spin	**g_s**	-2.00201	-2.00216

SO is thought to be formed in interstellar clouds via slow neutral-neutral reactions (Prasad & Huntress, 1982; Leen & Graff, 1988; Pineau des Forêts et al., 1993). Chemical models predict high abundances for molecular clouds with high visual extinction only after a few million years. If the gas is at high temperature or heated by a shock wave, observable SO abundances can be reached on a much shorter time scale and enhanced by several orders of magnitude (Hartquist et al., 1980; Prasad & Huntress, 1982; Mitchell, 1984; Watt & Charnley, 1985; Pineau des Forêts et

al., 1993; Charnley, 1997). The SO abundance falls again at long times because OH and O_2 are underabundant. In order to verify the existing chemical models, many observations on the relative abundances of SO with SO_2, H_2S, and CS towards various molecular clouds have been performed (Swade, 1989; Sahai & Wannier, 1992; Tieftrunk et al., 1994; Wright et al., 1996; Heithausen et al., 1998; Nilsson et al., 2000). The differences of the relative abundance in these species may be related to different cloud ages.

First detected in interstellar space 30 years ago (Gottlieb & Ball, 1973), SO is found in a variety of interstellar environments due to its rotational spectrum. It has been found in molecular clouds associated with HII regions (Gottlieb et al., 1978), dense cores in dark clouds (Rydbeck et al., 1980; Swade, 1989; Carral et al., 1992; Barnes & Crutcher, 1992), around oxygen-rich red giants (Sahai & Howe, 1987; Sahai & Wannier, 1992), in the star forming regions, near outflow and shock regions (Plambeck et al, 1982; Friberg, 1984; Watt et al., 1986; Blake et al., 1987; Martin-Pintado et al., 1992; Turner et al., 1992; Mundy et al., 1992; Schmid-Burgk & Muders, 1994; Chernin et al., 1994; Wright et al., 1996; Codella & Bachiller, 1999; Bachiller et al., 2001), and in the galactic cirrus clouds (Heithausen et al., 1995, 1998). In many cases, one observes SO emission originating from small, hot clumps.

For the lowest transition $J_K = (1_0\text{-}0_1)$ of $^{32}S^{16}O$ and $^{34}S^{16}O$, ν = 30.001539 and 29.678877 GHz (Clark & DeLucia, 1976; Rydbeck et al., 1980), the upper levels E_u are 1.44 and 1.425 K above the ground state, respectively. The Einstein coefficient A of spontaneous emission of the transition is 2.4×10^{-7} s^{-1}. Adapting the collision rates by Green (1994), the critical density is $\sim 8 \times 10^3$ cm^{-3} at 10 K. Therefore the SO transition should trace well cold dense clouds with density 10^4-10^5 cm^{-3}. Though SO emission is generally extended, the observational data on this 30 GHz transition are relatively rare in the literature (Gottlieb et al., 1978; Rydbeck et al., 1980; Tieftrunk, 1993; Tieftrunk et al., 1994; Schmid-Burgk & Muders, 1994; Heithausen et al., 1995, 1998; Codella & Muders, 1997). In this study, we performed an extended survey towards dense cores, active star forming regions, and supernova remnants. ^{34}SO isotopic line observations were carried out towards selected sources as a check on the optical depth of the ^{32}SO line.

2.2 Observations and Results

We observed the 30 GHz SO $J_K = (1_0\text{-}0_1)$ line towards around 50 sources between October 2001 and March 2003 with the MPIfR 100-m telescope in Effelsberg. We used the new "Zeeman receiver" to perform the survey (§3.3). The system temperature was 100-120 K at zenith, including antenna and atmospheric losses. Calibration sources like NGC7027 and W3(OH) were used. The uncertainty in the calibration for ^{32}SO observations is less than 10%. The uncertainty for the sources with low elevation angles (<15°) is expected to be larger. The data are given in terms of the main-beam brightness temperature $T_{mb} = T_a^* / \eta_{mb}$, where T_a^* is the corrected antenna temperature, and $\eta_{mb} = 0.6$ is the main-beam efficiency. Spectra were taken with the 8192 channel autocorrelator as backend. The beamwidth at this frequency is ~30". We detected ^{32}SO 30 GHz emission successfully towards over 40 sources in the survey. The results are listed in Table 2.1 and Fig. 2.1. The data for the ^{34}SO emission are shown in Table 2.2. The uncertainty in the calibration for ^{34}SO data is larger (20%) due to the unstable weather conditions in the summer 2003.

In order to perform the multi-line analyses using $SO(1_0\text{-}0_1)$ and $SO(1_2\text{-}1_1)$ transitions, on the sources where $SO(1_2\text{-}1_1)$ data are also available from Uchida (1994) (Table 2.2), at least a fully-sampled 90×90 $arcsec^2$ on-the-fly map was made. The SO emission was mapped using a grid

spacing of 15". Due to the different beam sizes of the two lines, we took the weighted sum of the on-the-fly map data at 30 GHz (beamwidth ~30") to fit the resolution of 13 GHz survey (beamwidth ~60"). During the procedure, both beams are assumed to be gaussian. In Fig. 2.1, we show the spectra for SO(1_0-0_1) and SO(1_2-1_1) towards 10 sources. The source sizes obtained from the 30 GHz line are listed in Table 2.2. The line parameters of both transitions are listed in Table 2.3.

The spectra of ^{34}SO and ^{32}SO for 11 sources (12 positions) are shown in Fig.2.2. We calculated the optical depth with the integrated intensity ($I_{mb} = T_{mb} \times \Delta V$) by the equation,

$$\frac{I_{32}}{I_{34}} = \frac{\int T_{32}(v)dv}{\int T_{34}(v)dv} = \frac{1-\exp[-\tau_{32}(v)]dv}{1-\exp[-\tau_{34}(v)]dv}, \tag{2.1}$$

and

$$\tau_{32} = R\tau_{34}, \tag{2.2}$$

where R is the ratio of ^{32}S/^{34}S. By adapting the terrestrial ratio R = 22 (Wilson & Rood, 1994) and assuming ^{34}SO transition is optically thin, the results are listed in Table 2.1(b). Wilson & Rood found no variance of this isotopic ratio with the galactocentric distance. The opacity of ^{32}SO(1_0-0_1) transition is large towards AF5124, NGC2071, L183, VLA1623, Rho-O2 and Oph-B. Towards VLA1623, ^{34}SO transition is probably also optically thick. In the cases of W3(OH), NGC2024/Orion B, DR21(OH), ^{32}SO is almost optically thin.

Table 2.1(a). Results from SO(1_0-0_1) 30 GHz line survey. For simplicity, most spectra are assumed to be single Gaussian. The spectrum is decomposed into more than one velocity component only when the signal-to-noise ratio is high or the velocity components are well-separated. The errors are also given.

Source name	R.A. (1950)	Dec (1950)	V_{LSR} (km/s)	T_{mb} (K)	ΔV (km/s)
W3-IRS4(S)	02:21:44.0	61:52:32	-42.6 (0.2)	0.78 (0.15)	4.6 (0.6)
W3-IRS5	02:21:53.0	61:52:21	-39.2 (0.3)	0.62 (0.15)	3.7 (0.6)
W3-3	02:22:06.1	61:50:35	-39.3 (0.3)	0.45 (0.15)	2.7 (0.7)
W3(OH)	02:23:16.5	61:38:57	-46.1 (0.1)	1.10 (0.22)	3.5 (0.2)
L1448NW	03:22:31.1	30:35:04	4.71 (0.06)	0.99 (0.21)	1.1 (0.11)
			4.94 (0.02)	1.64 (0.21)	0.39 (0.05)
L1448N	03:22:31.8	30:34:45	4.42 (0.01)	2.58 (0.33)	0.55 (0.04)
L1448C	03:22:34.4	30:33:35	4.65 (0.02)	1.42 (0.16)	0.68 (0.08)
NGC1333-IRAS4	03:26:05.0	31:03:13	6.92 (0.07)	2.23 (0.32)	0.81 (0.09)
			7.76 (0.02)	2.18 (0.32)	0.74 (0.04)
IRAS03282+3035	03:28:15.2	30:35:14	7.16 (0.07)	0.76 (0.31)	0.81 (0.22)
B1	03:30:12.0	39:57:26	6.57 (0.02)	2.67 (0.33)	0.82 (0.05)
L1498	04:07:55.8	25:01:33	7.70 (0.01)	1.60 (0.08)	0.15 (0.01)
			7.88 (0.02)	0.43 (0.08)	0.53 (0.05)
Tau 16	04:15:01.0	28:16:00	6.55 (0.01)	1.83 (0.15)	0.48 (0.02)
			6.77 (0.02)	0.85 (0.15)	0.45 (0.03)
IRAS04166+2706	04:16:37.8	27:06:29	6.75 (0.04)	0.72 (0.24)	0.50 (0.08)
L1527	04:36:49.6	25:57:21	5.90 (0.04)	0.82 (0.31)	0.54(0.10)
TMC-1C	04:38:31.5	25:55:00	5.20 (0.01)	2.43 (0.10)	0.31(0.01)
TMC-1	04:38:47.0	25:34:00	5.50 (0.03)	0.73 (0.23)	0.33 (0.03)
			6.02 (0.03)	1.28 (0.23)	0.52 (0.07)
TMC-1SE	04:38:50.1	25:32:30	5.52 (0.01)	1.49 (0.1)	0.17 (0.01)
			6.03 (0.01)	1.14 (0.1)	0.47 (0.02)
L1512	05:00:54.4	32:39:37	6.98 (0.03)	1.10 (0.16)	0.18 (0.06)
L1544	05:01:13.1	25:06:35	7.11 (0.01)	2.61(0.4)	0.28 (0.03)
AF5142	05:27:30.0	33:45:40	-3.47 (0.01)	2.16 (0.07)	2.64 (0.01)
OMC1N	05:32:47.0	-05:24:00	10.6 (0.1)	0.21 (0.04)	2.64 (0.25)
OMC1S	05:32:46.0	-05:24:45	8.0 (0.1)	0.82 (0.20)	2.83 (0.22)
OMCN-4	05:32:49.3	-05:21:24	9.5 (0.1)	0.92 (0.34)	1.20 (0.27)
NGC 2024/Orion B	05:39:13.1	-01:57:11	9.85 (0.01)	1.25 (0.03)	0.94 (0.02)
			10.13 (0.01)	0.99 (0.03)	2.51 (0.03)
B35	05:41:56.0	09:10:33	12.38 (0.02)	1.69 (0.10)	0.57 (0.06)
HH 25MMS	05:43:34.0	-00:14:42	10.2 (0.1)	0.62 (0.15)	1.52 (0.17)
NGC 2071SO	05:44:20.7	00:22:20	9.43 (0.01)	5.0 (0.3)	1.07 (0.02)
L1647	05:38:50.0	-07:58:00	4.59 (0.02)	2.17 (0.20)	0.92 (0.03)
S225	06:09:58.2	18:00:17	6.90 (0.14)	0.67 (0.27)	2.40 (0.42)
NGC2264C	06:38:26.0	09:32:00	8.0 (0.1)	1.28 (0.26)	3.7 (0.2)
NGC2264D	06:38:19.0	09:37:32	5.43 (0.03)	2.72 (0.36)	1.82 (0.08)
L134	15:50:55.0	-04:31:00	2.60 (0.01)	3.15 (0.07)	0.43 (0.01)
L183	15:51:32.7	-02:42:51	2.46 (0.01)	3.55 (0.32)	0.41 (0.02)
VLA1623SO	16:23:20.2	-24:16:04	2.98 (0.01)	4.40 (0.26)	0.96 (0.02)
RHO-O2	16:24:08.2	-24:22:18	3.57 (0.03)	6.12 (0.70)	0.96 (0.07)
Oph-B	16:24:08.9	-24:22:41	3.62 (0.03)	6.78 (0.55)	0.98 (0.05)
RHO-Oph1	16:24:16.0	-24:27:00	3.08 (0.06)	1.97 (0.42)	0.48 (0.05)
			3.86 (0.04)	1.00 (0.42)	0.49 (0.09)
RHO-Oph2	16:24:30.0	-24:11:00	3.30 (0.04)	1.43 (0.43)	0.67 (0.06)
L1696A	16:25:28.9	-24:12:07	3.56 (0.03)	1.58 (0.49)	0.46 (0.08)

Source name	R.A. (1950)	Dec (1950)	V_{LSR} (km/s)	T_{mb}(K)	ΔV (km/s)
L1689B	16:31:47.0	-24:57:22	3.45 (0.02)	3.08 (0.45)	0.56 (0.04)
IRAS16293	16:29:20.9	-24:22:13	3.88 (0.02)	2.67 (0.44)	0.68 (0.08)
L43	16:31:44.9	-15:40:46	0.59 (0.02)	2.00 (0.39)	0.42 (0.03)
L204	16:45:00.0	-12:00:00	4.05 (0.03)	1.45 (0.40)	0.55 (0.07)
L63	16:47:19.7	-18:01:13	5.66 (0.02)	2.73 (0.12)	0.38 (0.03)
L483	18:14:50.6	-04:40:49	5.19 (0.01)	3.38 (0.05)	0.34 (0.01)
			5.61 (0.01)	1.30 (0.05)	0.37 (0.02)
M17 SWs	18:17:31.8	-16:15:05	19.4 (0.1)	0.47 (0.14)	1.57 (0.32)
B133	19:03:26.6	-06:57:36	12.0 (0.1)	2.15 (0.35)	0.64 (0.05)
L723	19:15:41.3	19:06:47	10.9 (0.1)	0.58 (0.15)	1.03 (0.21)
W51d	19:21:22.3	14:25:15	59.5 (0.9)	0.78 (0.28)	15.7 (2.3)
W51e2	19:21:26.24	14:24:41.4	55.6 (0.9)	1.5 (0.2)	10.7 (0.8)
W51	19:21:27.0	14:24:39	55.8 (0.1)	1.03 (0.16)	7.36 (0.23)
B335	19:34:34.0	07:27:00	8.23 (0.01)	1.56 (0.20)	0.28 (0.02)
IRAS20050	20:05:02.5	27:20:09	6.2 (0.1)	0.50 (0.13)	1.71 (0.19)
W75N	20:36:50.5	42:27:01	9.8 (0.1)	1.05 (0.26)	3.6 (0.3)
DR21(OH)-RC	20:37:13.0	42:12:00	-4.67 (0.01)	0.52 (0.01)	1.80 (0.01)
			-2.9 (0.01)	1.30 (0.01)	2.90 (0.01)
			0.0 (0.01)	0.18 (0.01)	2.00 (0.01)
DR21(OH)	20:37:13.9	42:12:11	-3.05 (0.21)	1.15 (0.2)	3.4 (0.6)
L1157	20:38:39.6	67:51:33	2.49 (0.14)	1.03 (0.10)	0.61 (0.29)
			2.80 (0.01)	1.57 (0.10)	0.25 (0.05)
L1155C	20:43:00.0	67:41:47	2.70 (0.02)	1.07 (0.19)	0.78 (0.04)
			0.83 (0.02)	0.78 (0.19)	0.36 (0.04)
L1172	21:01:48.6	67:42:13	2.76 (0.02)	0.58 (0.20)	0.19 (0.06)
S140 SO	22:17:42.0	63:04:00	-7.19 (0.03)	1.15 (0.11)	2.45 (0.07)
CEPA	22:54:20.2	61:45:55	-10.57 (0.03)	1.42 (0.13)	2.22 (0.09)
NGC7538D	23:11:38.6	61:10:48	-56.9 (0.04)	1.90 (0.19)	3.89 (0.10)
NGC 7538 SO	23:11:40.9	61:10:48	-56.7(0.03)	1.87(0.13)	3.57 (0.07)
CB224	23:23:48.7	74:01:08	4.03 (0.01)	1.70 (0.11)	0.42 (0.02)
L1262	23:24:05.0	74:00:00	4.0 (0.02)	0.90 (0.26)	0.58 (0.08)

Table 2.1(b). Line parameters of the $^{34}SO(1_0\text{-}0_1)$ transition (Beamwidth = 30"). The column (5) and (6) give the peak intensity (T_{mb}) ratio and integrated intensity (I_{mb}) ratio of ^{32}SO and ^{34}SO lines. The terrestrial ratio of $^{32}S/^{34}S$ is 22. The optical depths of ^{32}SO are calculated from column (6), assuming ^{34}SO is optically thin. Error bars are given.

Name	V_{LSR} (km/s)	Intensity (T_{mb}) (K)	ΔV (km/s)	$\frac{T_{mb}(^{32}SO)}{T_{mb}(^{34}SO)}$	$\frac{I_{mb}(^{32}SO)}{I_{mb}(^{34}SO)}$	τ (^{32}SO)
W3-IRS4(S)*	-42.2 (0.3)	0.071 (0.024)	2.4 (0.6)	18.3^{+13}_{-6}	18.3^{+3}_{-3}	0.4 (0.4)
W3(OH)	-47.4 (0.1)	0.096 (0.030)	1.1 (0.6)	11.5^{+8}_{-4}	34.7^{+2}_{-2}	-0.04 (0.01)
AF5142	-3.2 (0.2)	0.14 (0.04)	3.0 (0.4)	15.4^{+6}_{-4}	14.1^{+2}_{-2}	1.0 (0.4)
NGC2024 / Orion B+	10.0 (0.3)	0.078 (0.025)	1.7 (0.4)	18.3^{+10}_{-5}	21.4^{+4}_{-3}	0.06 (0.3)
NGC2071SO	9.46 (0.01)	0.7 (0.07)	1.0 (0.03)	7.6^{+1}_{-1}	$7.9^{+0.5}_{-0.3}$	2.8 (0.2)
L183	2.40 (0.01)	0.58 (0.09)	0.36 (0.04)	6.1^{+2}_{-1}	$7.0^{+0.6}_{-0.6}$	3.2 (0.4)
VLA1623SO	2.76 (0.01)	1.18 (0.12)	0.70 (0.02)	3.8^{+1}_{-1}	$5.5^{+0.2}_{-0.2}$	$4.4^{+0.1}_{-0.3}$
RHO-O2	3.62 (0.02)	0.68 (0.12)	0.84 (0.04)	9.1^{+3}_{-2}	10.6^{+1}_{-1}	1.8 (0.3)
Oph-B	3.58 (0.02)	0.67 (0.13)	0.84 (0.05)	10.1^{+3}_{-3}	11.7^{+1}_{-1}	1.5 (0.3)
W51e2	55.8 (0.2)	0.08 (0.01)	7.3 (0.5)	19.7^{+5}_{-5}	28.9^{+3}_{-2}	-0.66 (0.2)
DR21(OH)-RC+	-3.3 (0.1)	0.078 (0.005)	3.4 (0.2)	20.5^{+1}_{-1}	$20.9^{+0.5}_{-0.5}$	0.11 (0.05)
S140SO	-7.1 (0.1)	0.09 (0.04)	1.9 (0.3)	12.5^{+13}_{-4}	16.9^{+4}_{-3}	0.6 (0.5)
S140SO*	-7.3 (0.1)	0.14 (0.03)	2.4 (0.3)	20.0^{+8}_{-6}	$17.2^{+2}_{-1.5}$	0.5 (0.2)
NGC7538SO	-56.2 (0.1)	0.16 (0.03)	2.5 (0.3)	11.7^{+4}_{-2}	17.3^{+2}_{-2}	0.5 (0.3)

* At the peak position. Please see Table 2.2 for the coordinate.

+ The ^{32}SO spectrum is fitted by single gaussian for rough comparison.

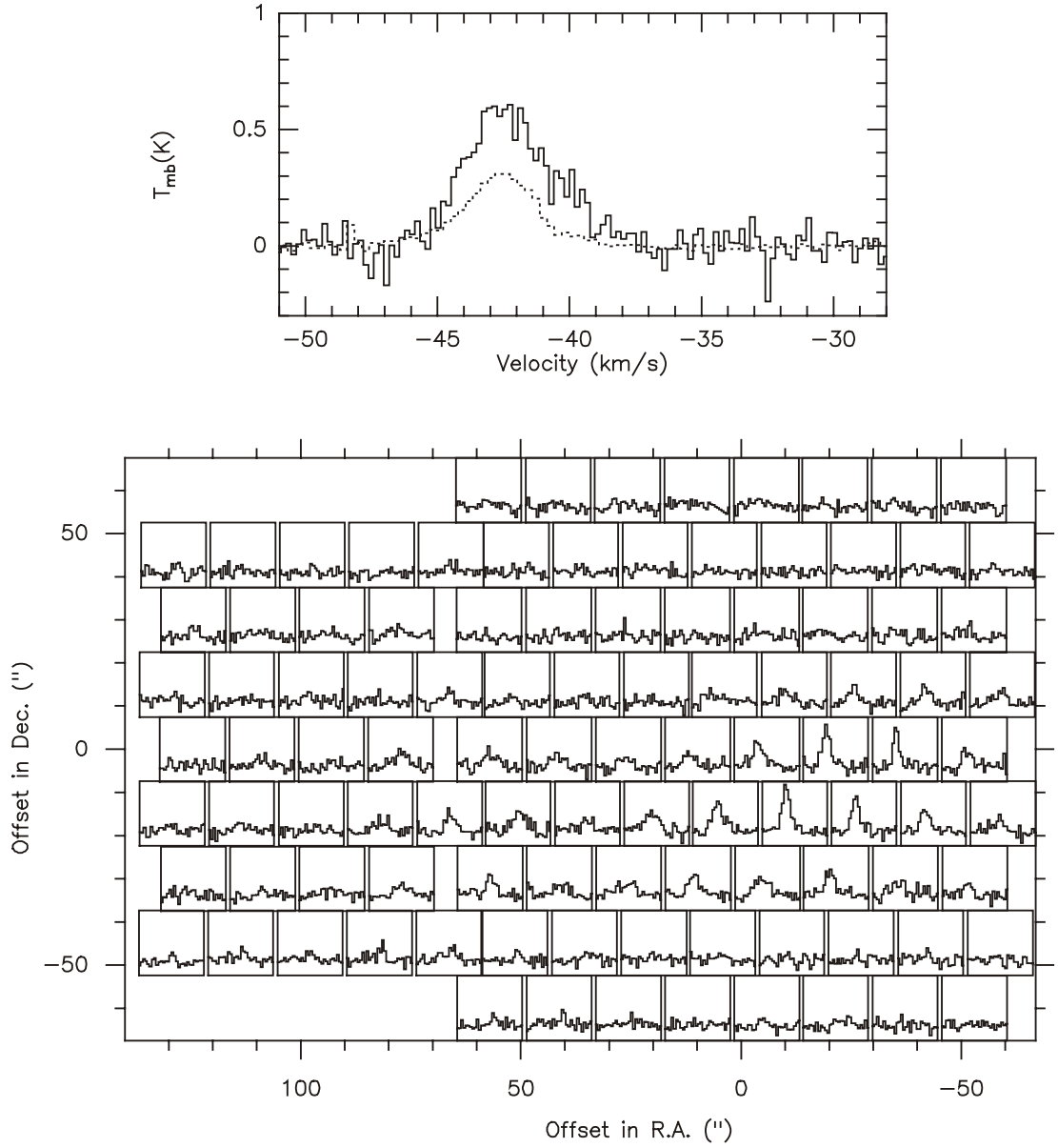

Fig. 2.1(a). Top: S0 30 GHz (solid; smoothed to 60" resolution) and 13 GHz (dashed; x2) spectra towards W3–IRS4(S).
Bottom: 30 GHz map towards W3–IRS4(S) region (in T_a^* scale).

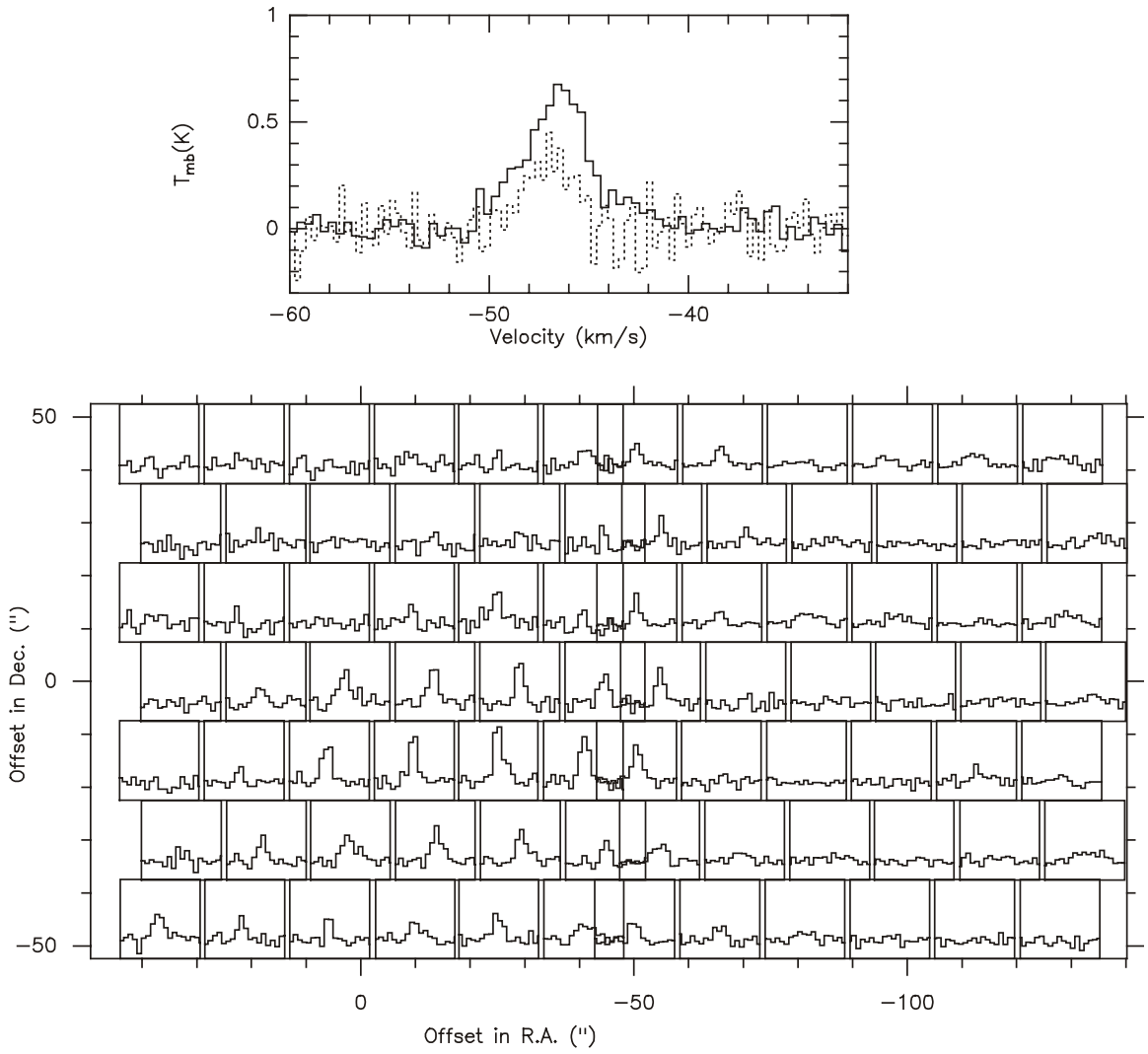

Fig. 2.1(b). Top: SO 30 GHz (solid; smoothed to 60" resolution) and 13 GHz (dashed; x2) spectra towards W3(OH).
Bottom: 30 GHz map towards W3(OH) region (in T_a^* scale).

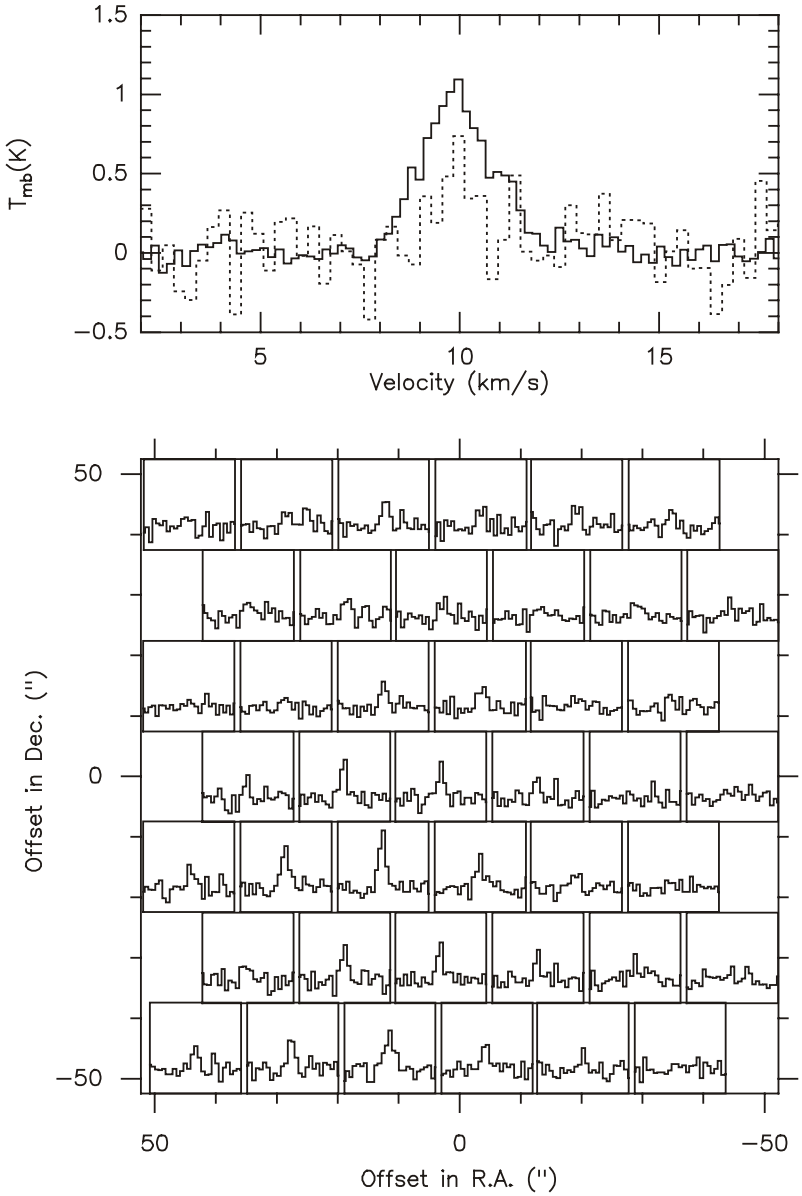

Fig. 2.1(c). Top: SO 30 GHz (solid; smoothed to 60" resolution) and 13 GHz (dashed; x2) spectra towards NGC2024.
Bottom: 30 GHz map towards NGC2024 region (in T_a^* scale).

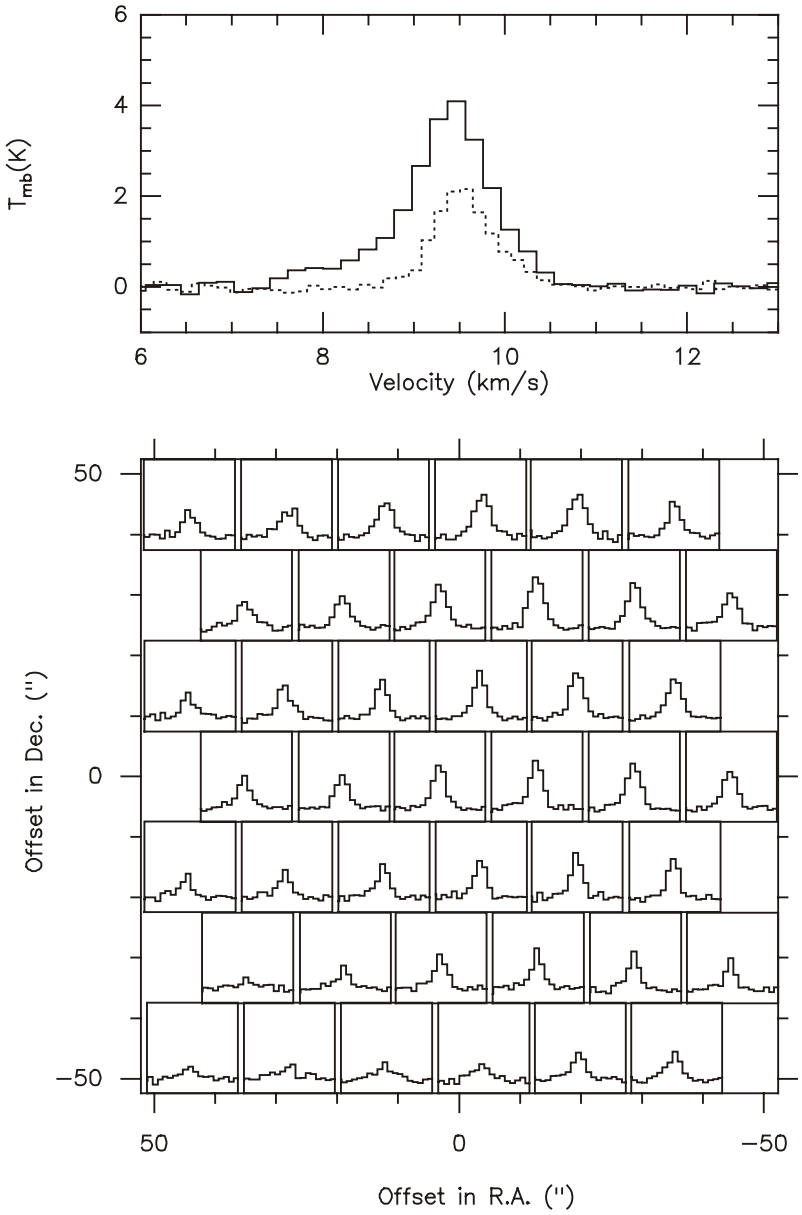

Fig. 2.1(d). Top: SO 30 GHz (solid; smoothed to 60" resolution) and 13 GHz (dashed, x4) spectra towards NGC2071SO.
Bottom: 30 GHz map towards NGC2071SO region (in T_a^* scale).

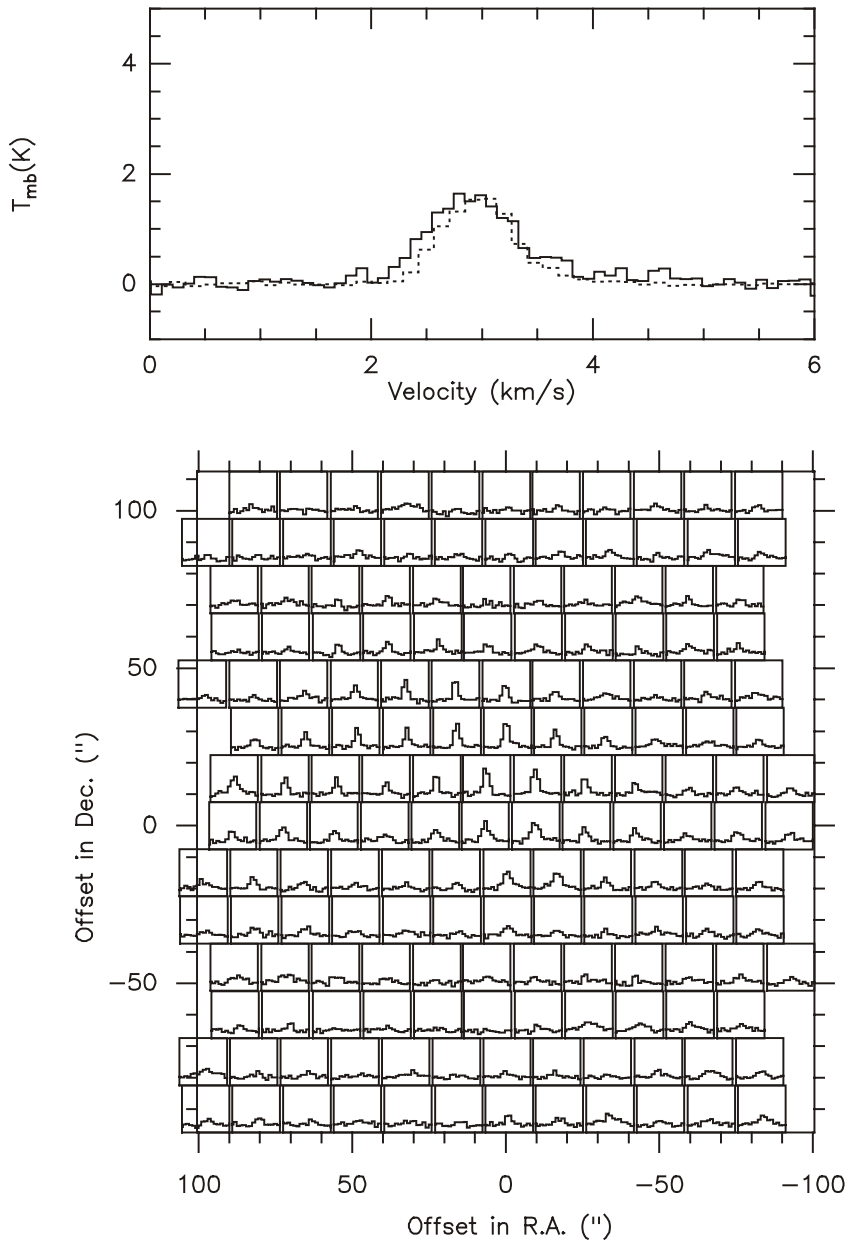

Fig. 2.1(e). Top: S0 30 GHz (solid; smoothed to 60" resolution) and 13 GHz (dashed) spectra towards VLA1623.
Bottom: 30 GHz map towards VLA1623 region (in T_a^* scale).

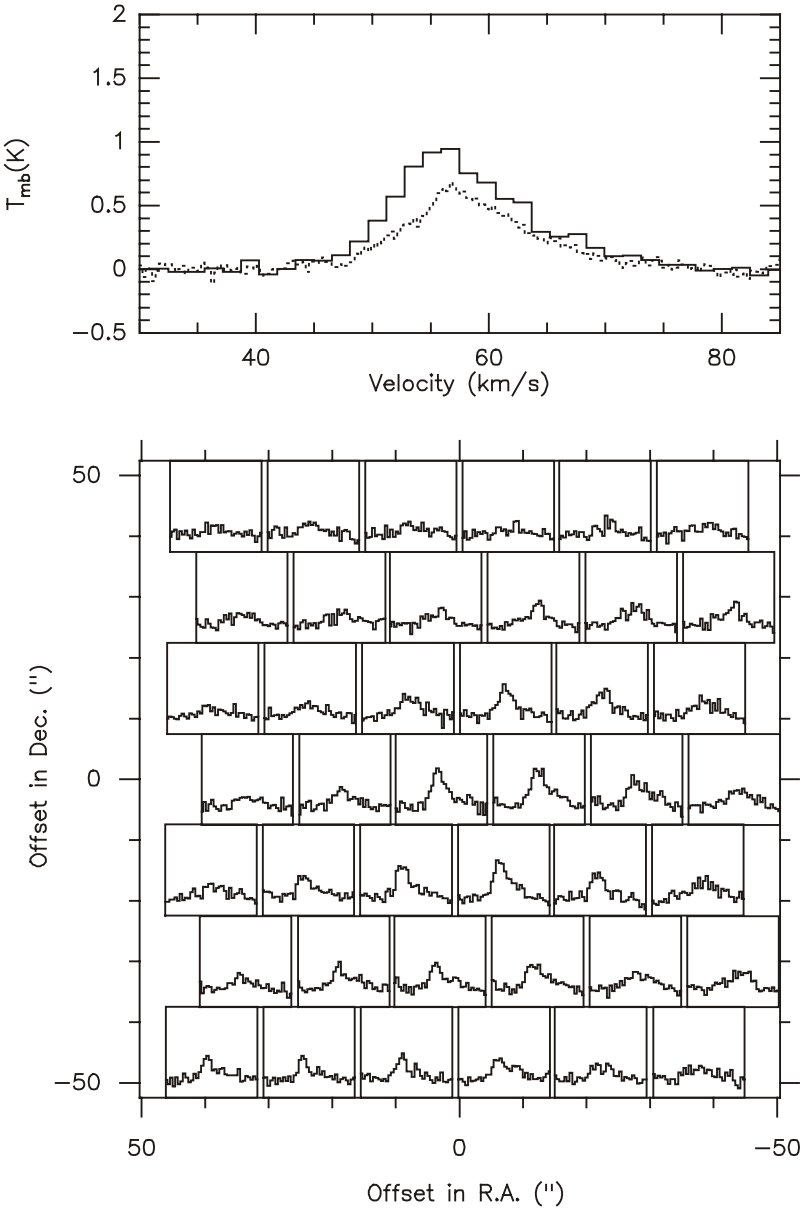

Fig. 2.1(f). Top: SO 30 GHz (solid; smoothed to 60" resolution) and 13 GHz (dashed; x2) spectra towards W51e2.
Bottom: 30 GHz map towards w51e2 region (in T_a^* scale).

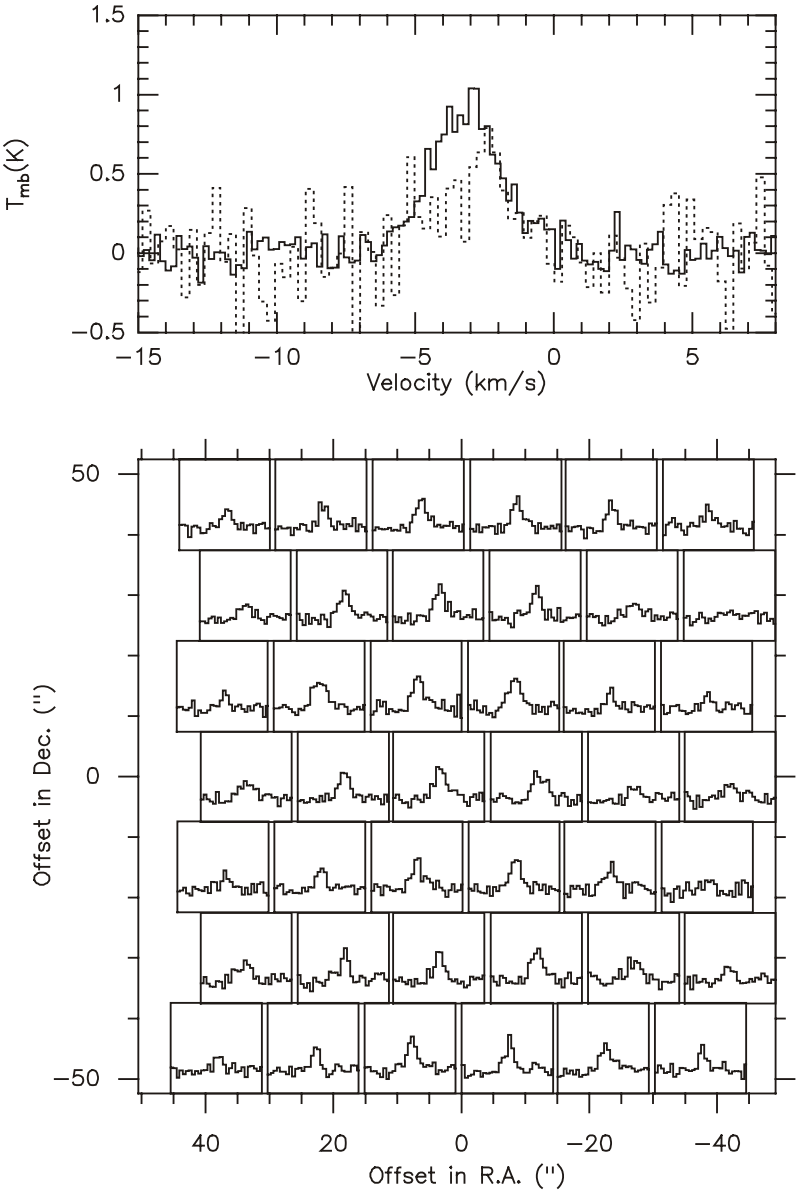

Fig. 2.1(g). Top: SO 30 GHz (solid; smoothed to 60" resolution) and 13 GHz (dashed; x5) spectra towards DR21(OH).
Bottom: 30 GHz map towards DR21(OH) region (in T_a^* scale).

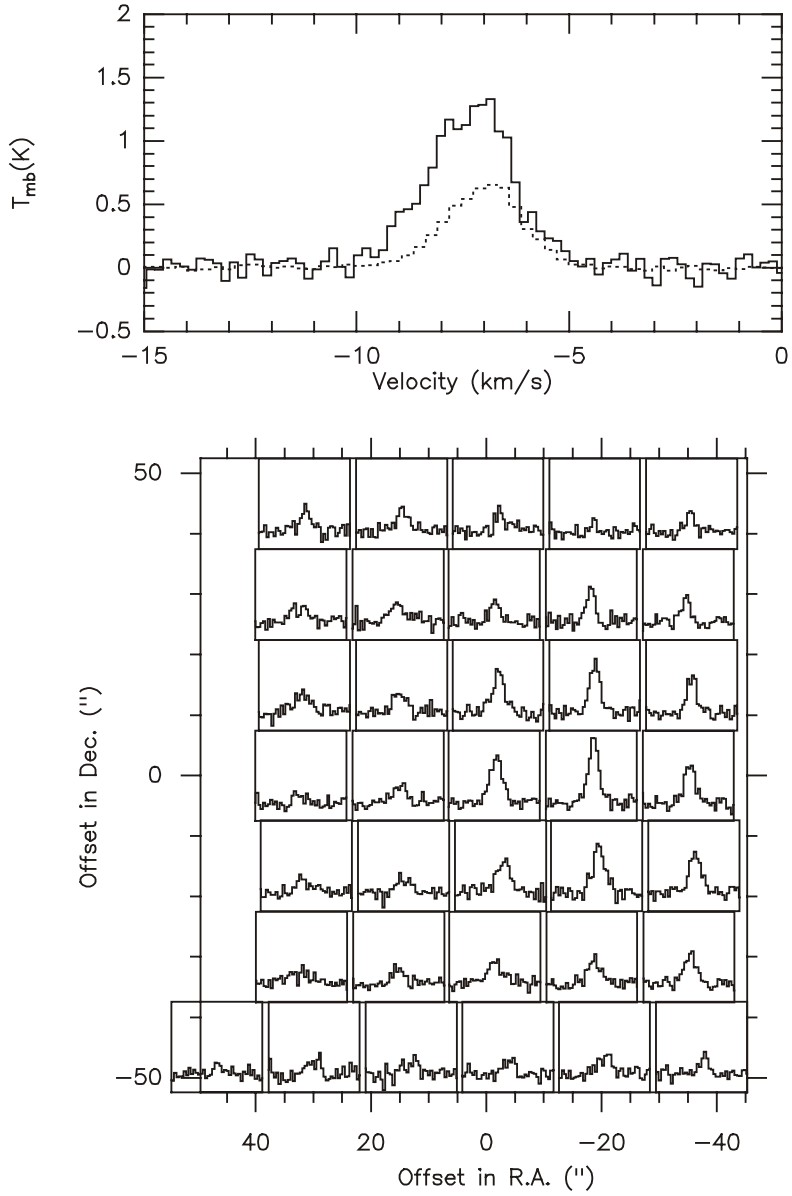

Fig. 2.1(h). Top: SO 30 GHz (solid; smoothed to 60" resolution) and 13 GHz (dashed; x2) spectra towards S140SO.
Bottom: 30 GHz map towards S140SO region (in T_a^* scale).

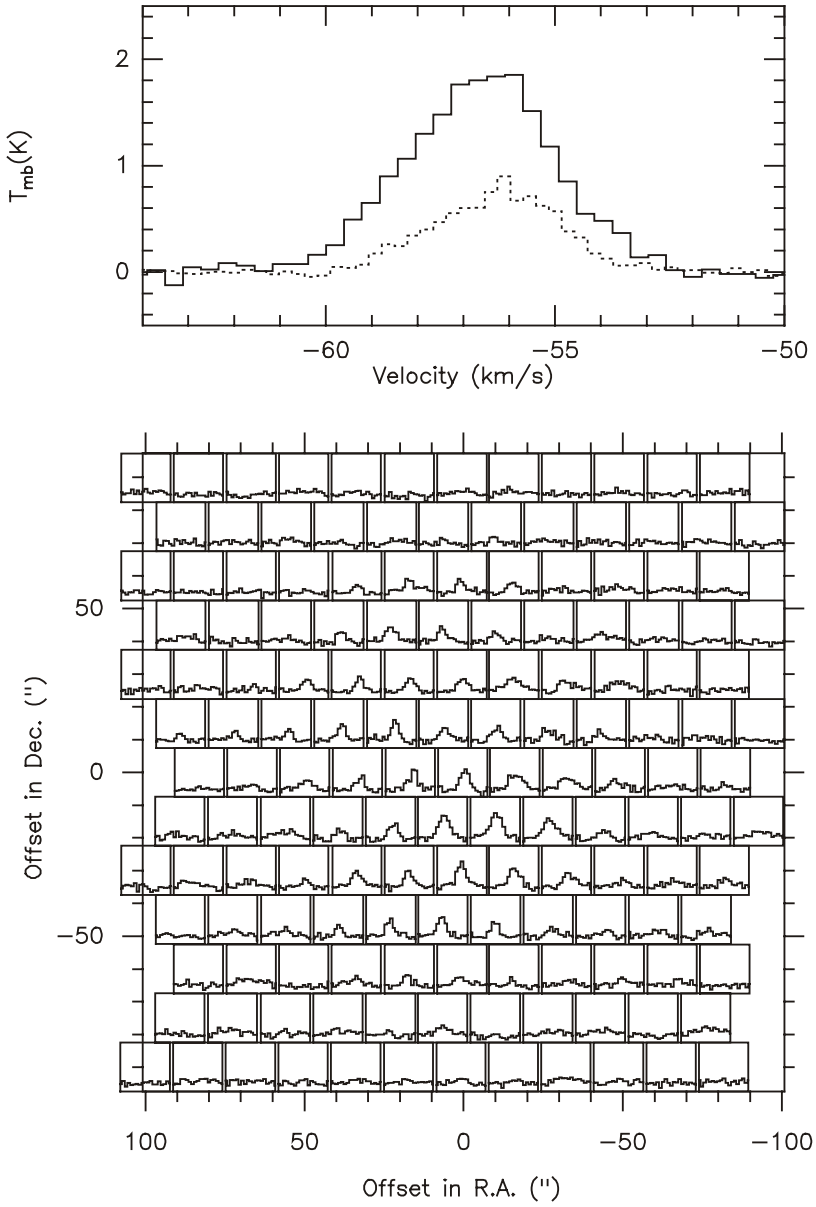

Fig. 2.1(i). Top: SO 30 GHz (solid; smoothed to 60" resolution) and 13 GHz (dashed; x4) spectra towards NGC7538.
Bottom: 30 GHz map towards NGC7538 region (in T_a^* scale).

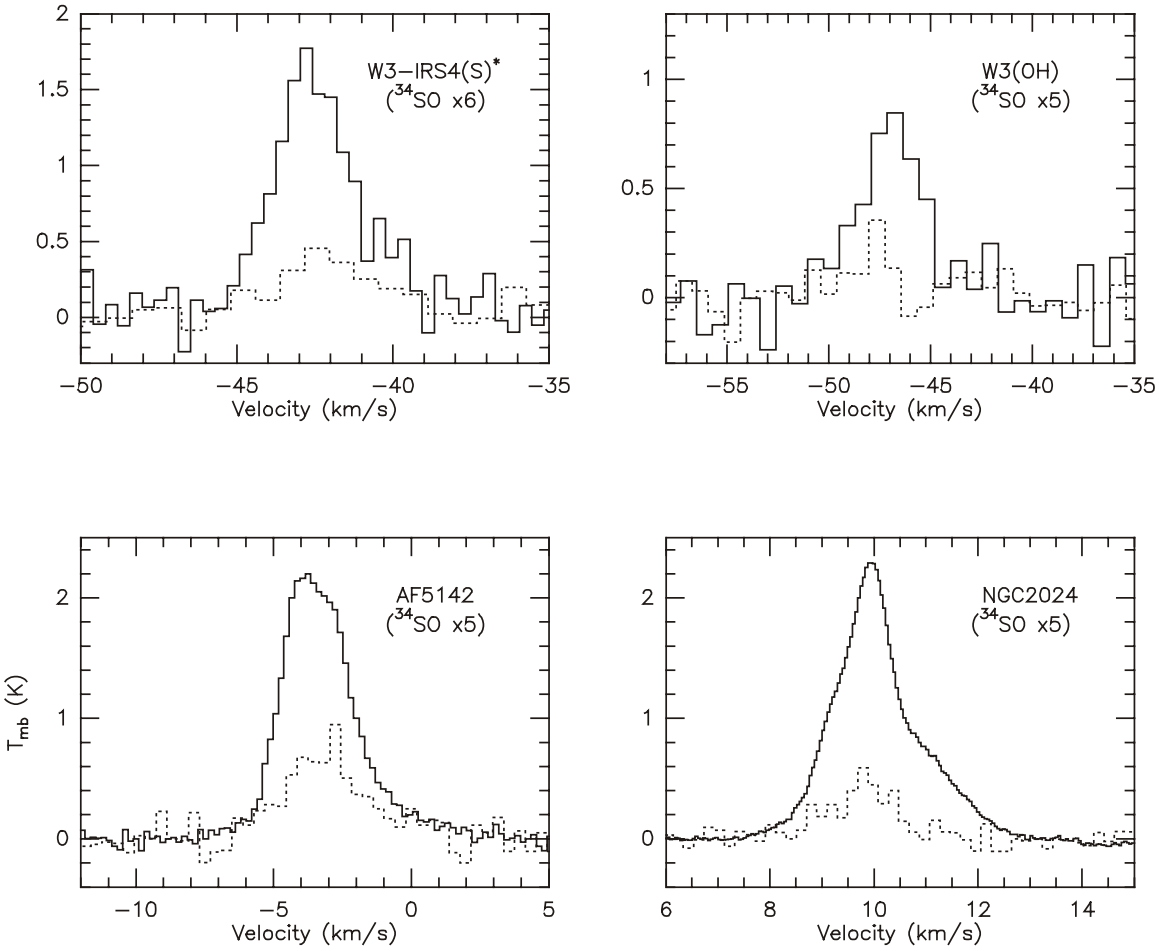

Fig. 2.2. ^{32}SO spectra (solid) and ^{34}SO (dashed) spectra.
*At the peak position. See Table 2.2 for coordinate.

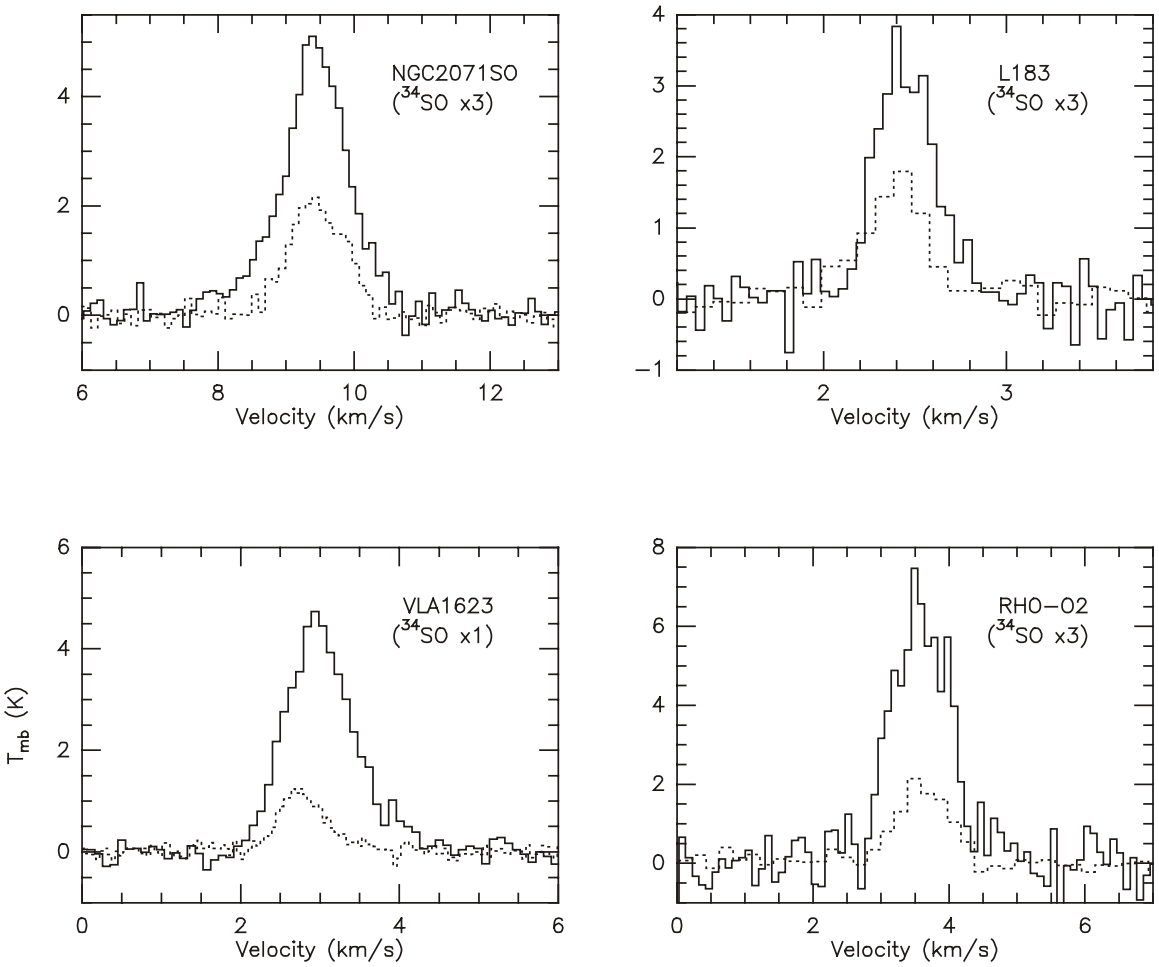
NGC2071SO
(^{34}SO x3)
L183
(^{34}SO x3)
VLA1623
(^{34}SO x1)
RHO−02
(^{34}SO x3)
T_{mb} (K)
Velocity (km/s)

Fig. 2.2. (conti.)

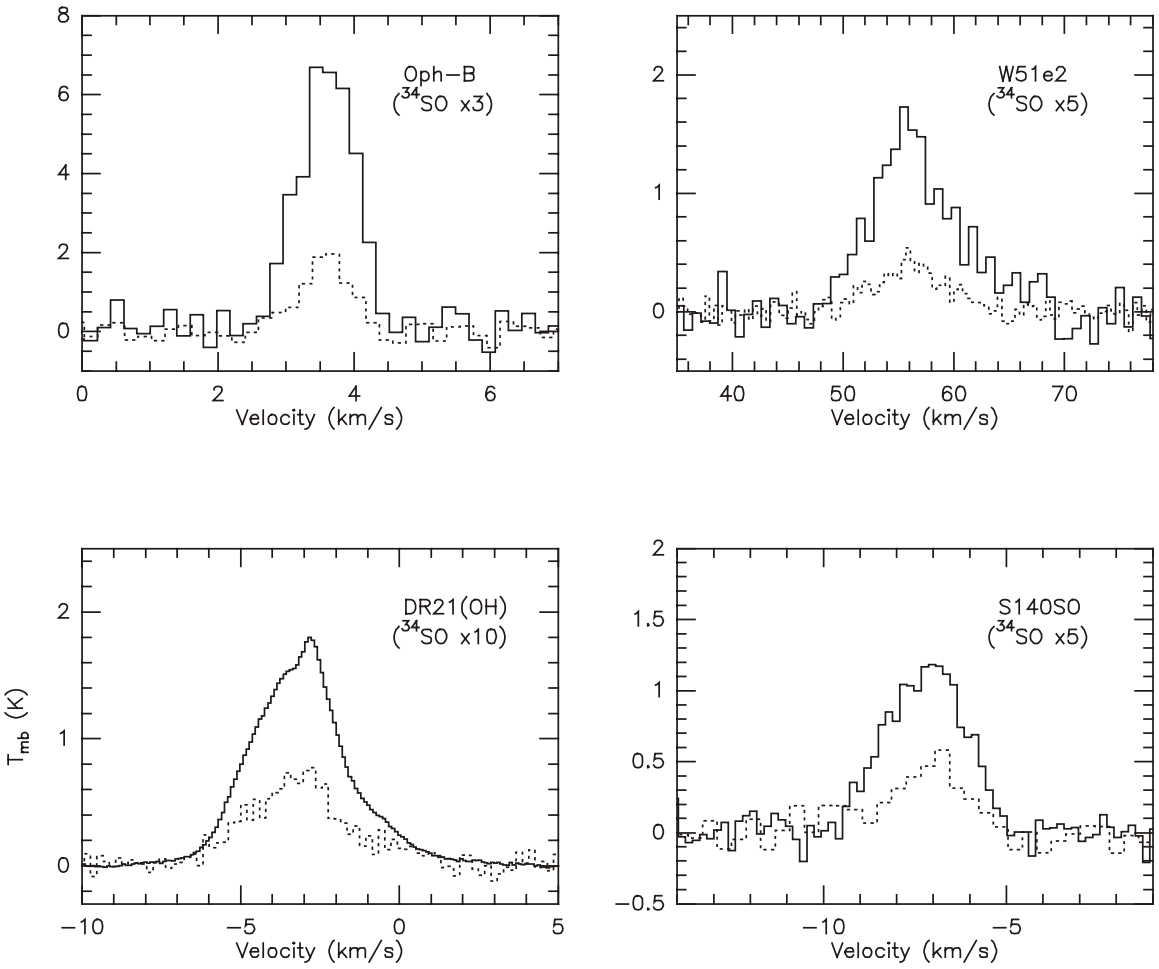
Oph−B
(^{34}SO x3)
W51e2
(^{34}SO x5)
DR21(OH)
(^{34}SO x10)
S140SO
(^{34}SO x5)
T_{mb} (K)
Velocity (km/s)

Fig. 2.2. (conti.)

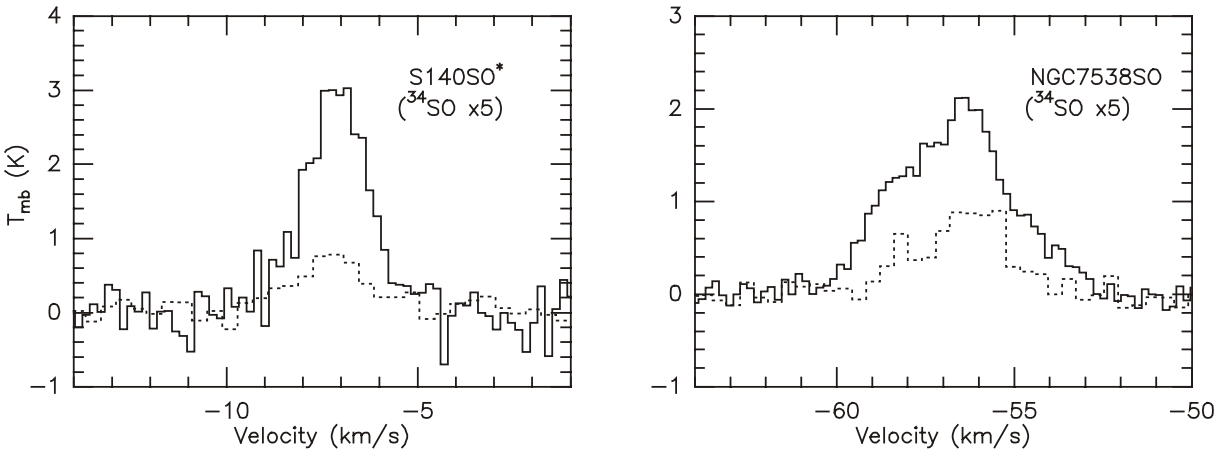
S140SO*
(^{34}SO x5)
T_{mb} (K)
Velocity (km/s)
NGC7538SO
(^{34}SO x5)
Velocity (km/s)

Fig. 2.2. (conti.)

Table 2.2. The peak positions and sizes derived from SO 30GHz observation (error = half beamwidth = 15 arcsec). Source sizes are deconvolved values (FWHM) in arcsec, assuming Gaussian sources and beams. The SO emission of NGC2071SO is extended. We failed to find the peak position.

Source name	α (1950)	δ (1950)	Δα	Δδ
W3-IRS4(S)	02:21:41.7	61:52:17	51	29
W3(OH)	02:23:15.1	61:38:43	49	46
NGC2024/Orion B	05:39:14.2	-01:57:26	38	20
NGC2071SO	-	-	-	-
VLA1623SO	16:23:19.6	-24:15:47	79	65
W51e1/e2	19:21:24.2	14:24:41	31	51
DR21(OH)	20:37:13.0	42:12:00	48	73
S140SO	22:17:40.1	63:04:01	33	45
NGC7538SO	23:11:38.9	61:10:33	70	103

Table 2.3. Line parameters of SO 30GHz and 13GHz transitions (both with 60" resolution).

	30GHz			13GHz		
Name	**V_{LSR} (km/s)**	**Intensity (T_{mb}) (K)**	**ΔV (km/s)**	**V_{LSR} (km/s)**	**Intensity (T_{mb}) (K)**	**ΔV (km/s)**
W3-IRS4(S)	-42.38 (0.06)	0.49 (0.15)	3.05 (0.13)	-42.6 (0.1)	0.16 (0.01)	3.4 (0.1)
W3(OH)	-46.54 (0.06)	0.59 (0.08)	3.56 (0.15)	-47.0 (0.1)	0.17 (0.05)	2.5 (0.4)
NGC2024 / Orion B	9.90 (0.03)	0.94 (0.10)	2.03 (0.07)	9.9 (0.1)	0.32 (0.10)	1.0 (0.3)
NGC2071SO	9.41 (0.01)	3.91 (0.21)	1.12 (0.04)	9.54 (0.01)	0.54 (0.01)	0.78 (0.02)
VLA1623SO	2.90 (0.02)	1.60 (0.14)	0.99 (0.05)	2.96 (0.01)	1.62 (0.02)	0.77 (0.01)
W51e2	55.9 (0.2)	0.90 (0.06)	13.7 (0.5)	57.5 (0.1)	0.23 (0.02)	9.9 (0.2)
DR21(OH)	-3.20 (0.05)	0.93 (0.11)	3.0 (0.1)	-2.7 (0.4)	0.13 (0.06)	4.7 (1.6)
S140SO	-7.31 (0.03)	1.28 (0.10)	2.39 (0.06)	-7.00 (0.02)	0.33 (0.01)	2.1 (0.1)
NGC7538SO	-56.53 (0.05)	1.64 (0.12)	3.21 (0.12)	-56.2 (0.1)	0.21 (0.01)	3.71 (0.05)

2.3 Rotational Temperature Diagrams Method

2.3.1 Introduction

The Rotational Temperature Diagram is a customary technique to analyse the data of an individual molecule with many transitions. This method assumes LTE conditions so that a single rotational temperature (T_{rot}), which is much larger than the background temperature T_{bg}, characterizes the level population of all transitions. If the transitions are all optically thin, it provides a good estimate of the column density of the molecule towards the source and the rotational temperature. With this simple method, one gets a good starting point for the modelling.

2.3.2 The Method

If the line is optically thin and the excitation temperature between two level T_{ex} is much larger than background temperature T_{bg}, the integration of the standard radiative transfer equation shows that (Cummins et al., 1986; Blake et al., 1987; Turner, 1991; Helmich et al., 1994)

$$\frac{N_u}{g_u} = \frac{3kc}{8\pi^3 \mu^2 \nu^2 S} \int T_b d\nu \,, \tag{2.3}$$

where N_u and g_u are the column density and degeneracy of the upper transition state, ν is the transition frequency, μ is the permanent dipole moment, S is the intrinsic line strength, and T_b is the brightness temperature of the observed line.

If we assume LTE, a single rotational temperature T_{rot} describes the population distribution, for the column density of the upper level, we have:

$$\frac{N_u}{g_u} = \frac{N_T}{Q(T_{rot})} e^{-E_u / kT_{rot}} \,, \tag{2.4}$$

where Q(T) is the rotational partition function, N_T is the total molecular column density, and E_u is the energy of the upper transition state. Combining these two equations, and substituting $d\nu=(\nu/c)dv$ to change the integral to Doppler velocities, we get,

$$\log(\frac{3k\int T_b dv}{8\pi^3 \mu^2 \nu S}) = \log(\frac{N_T}{Q(T_{rot})}) - \frac{E_u \cdot \log e}{kT_{rot}} \,. \tag{2.5}$$

This equation shows $\log(3k\int T_b dv / 8\pi^3 \mu^2 \nu S)$ is a linear function of E_u/k, with slope $-(\log e)/T_{rot}$, and intercept $\log(N_T /Q(T_{rot}))$ at $E_u = 0$. This method is referred as "Rotational Temperature Diagram". The rotational temperature determined by the method will be close to kinetic temperature, if collisional excitation dominates. If radiative decay competes with collisional excitation, the rotational temperature will be below the kinetic temperature. To estimate the partition function, Q, we used interpolation and extrapolation from the measured data provided by Pickett et al. (2000). A typical diagram of the method is shown in Fig. 2.3.

When applying this method with several tranistions, in some cases a single linear fit for all data cannot be found. Instead of it, one is forced to use a piecewise linear fit. That implies the emissions from higher and lower levels may originate from different parts of the cloud with two different rotational temperatures characterizing the transitions. Goldsmith and Langer (1999) investigated the method with numerical simulation and found some of this phenomena may come from the effects of line saturation. They introduced the optical depth correction factor C_τ,

$$C_\tau = \frac{\tau}{1 - e^{-\tau}} \,, \tag{2.6}$$

where τ is the optical depth. Therefore N_u in (2.3) becomes,

$$N_u = N_u^{thin} C_\tau \,, \tag{2.7}$$

and (2.5) becomes,

$$\log(\frac{3k\int T_b dv}{8\pi^3 \mu^2 \nu S}) = \log(\frac{N_T}{Q(T_{rot})}) - \frac{E_u \cdot \log e}{kT_{rot}} - \log C_\tau \,. \tag{2.8}$$

Therefore for an optically-thick transition, if we do not realize the fact of line saturation, the data points drawn in Fig. 2.3 will be lower than the real values by the distance of $\log(C_\tau)$. If the opacity τ is large, the difference is more obvious. If the transition is optically thin $\tau << 1$, $C_\tau = 1$, there is no difference between eq. (2.5) and (2.8). Because different transitions have different

optical depths, one usually needs a piecewise linear fit for the uncorrected data in the method. And depending on the data set used, the derived rotational temperature would be either higher or lower than the real value. But the derived column density is generally lower than the real value.

With the modified method considering the effects of the opacity, Goldsmith & Langer (1999) successfully fitted a single rotational temperature for some observed data where more than one rotational temperatures were needed before. But in general, the relative optical depth is hard to determine if the physical conditions are poorly known. Thus in most cases, one can only discuss the effect qualitatively. In our applications the error from the opacity effect would be large, since we have only two points in the diagram.

Turner (1991) discussed the uncertainty of the Rotational Temperature Diagrams, and pointed out the error in $\int T_b dv$ is equal to $\sigma / \sqrt{m}$, where σ is the rms noise in the spectrum and m is the number of channels in the line. The typical 3σ value of $\int T_b dv$ in the data is less than 0.1 K km s^{-1}. It corresponds to less than 10% uncertainty in the rotational temperature calculation. Only in the case of NGC2024, where the spectrum at 13 GHz is noiser, the uncertainty is around ±20%.

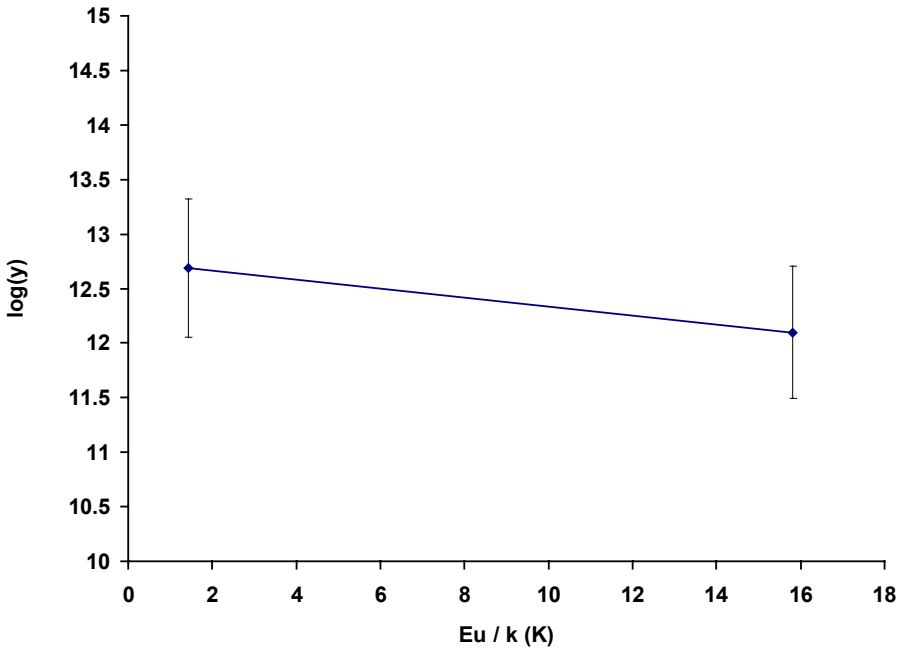

Fig. 2.3. Typical diagram in rotational temperature method, log(y)= $\log(3k\int T_b dv / 8\pi^3 \mu^2 \nu S)$.

2.3.3 Estimating SO column density with Rotational Diagrams Method and LVG program

Together with the $J_K = (1_2\text{-}1_1)$ 13.043811 GHz data obtained in 1993-94 (Uchida 1994; Uchida et al., 2001), we applied the Rotation Temperature Diagrams method to extract the column density of SO molecule and rotational temperature towards each source. At the same time, we tried to fit the intensity ratio of the two lines and the line intensities in LVG (Large-Velocity-Gradient) program using the kinetic temperature measured by ammonia to determine the cloud density $n(H_2)$ and SO column density per linewidth N(SO)/ΔV. The results are shown in Table 2.4. The

opacity effect in the 30 GHz transition was already taken into account in the rotational diagram method.

In Fig. 2.1 and Table 2.3, one can see the V_{LSR} in both transitions agrees with each other in all the sources. Except DR21OH and NGC7538SO, in most cases the linewidth of the 30GHz transition is broader than that of 13 GHz line. We can also see in some cases the 13 GHz line corresponding to only one velocity component in the 30 GHz line profile. From the figures and the rough optical depth estimate of the 30 GHz transition in Table 2.1(b), except for VLA1623SO which is a very special case, we think the 13 GHz line is optically thin.

The upper levels E_u are 1.44 and 15.82 K above the ground state for the 30 and 13 GHz transitions respectively. Considering the finite optical depth, since the 30GHz transition has larger opacity than 13 GHz, we expected the left point (E_u/k = 1.44 K) in the rotational diagram should be shifted upwards more. Therefore we will have a lower rotational temperature after considering the opacity effect. In the calculations, we used the opacity of the 30 GHz transition from Table 2.1(b) and assumed the 13 GHz transition is optically thin.

The rotational temperatures for other cases are all between the kinetic temperature and background temperature T_{bg} = 2.7 K. In most cases, $N(SO)/\Delta v$ from Rotation Diagrams is higher than that from LVG by a factor of 2 to 3. The difference may come from the uncertainty of the kinetic temperature used in LVG, the unknown beam filling factor, and non-LTE excitation condition. For most of the cases discussed here, the estimated $N(SO)/\Delta V$ and the cloud density $n(H_2)$ from the LVG model will be higher, if T_k goes down. The latter two reasons are hard to discuss because we have only data for two transitions and the resolution (60") is relatively low.

For the special case VLA1623SO, the line intensities and line profiles are almost identical from both transitions. There is no solution for VLA1623SO in LVG. It might imply the gas is far from the LTE conditions. And there is a solution in rotational diagram only after considering the opacity correction factor in the 30 GHz transition. But we did not apply the correction in the 13 GHz transition due to the lack of information. This transition is probably also optically thick. One can see from Table 2.1(b), even ^{34}SO might not be optically thin.

In Table 2.5, the column density of molecular hydrogen from different observations are compiled for comparison. We list the molecular hydrogen column densities estimated by $C^{18}O$ or ^{13}CO, which trace the spatial distribution of the gas column density, and mm-wave continuum observations, which trace the cold dust. In most cases we assumed $[^{13}CO]/[H_2] \sim 2.5\times 10^{-6}$, $[C^{18}O]/[H_2] \sim 2\times 10^{-7}$ (Frerking et al., 1982), and a dust mass opacity coefficient $\kappa_\nu = 0.1(\nu/10^{12}\text{Hz})^\beta$ cm^2g^{-1}, ß = 2, unless the authors have specified their values. But the uncertainty in β is large (see review by Henning et al., 1995). The rotational temperature derived from SO was used to derive the column density if the excitation temperature was needed in the calculation. In the last column of Table 2.5, the SO abundance $[SO]/[H_2]$ is also derived. The values only make sense if the SO molecule and the molecular hydrogen coexist in the same region. The assumption may not always be true because the spatial distribution of SO, CO and dust may be totally different in some cases.

In Table 2.6 we compared the molecular hydrogen density from SO lines calculated by the LVG program with the results from other molecules or continuum observations. The different values from various observations may come from the effect of different resolutions or different tracers. Ammonia data which traces more compact regions may give us the upper limit.

Table 2.4. Column density N(SO) from rotation diagrams method and LVG calculations. ΔV is the linewidth.

	Rotation Diagram			LVG		
Source	**T_{rot} (K)**	**N(SO) (10^{14} cm^{-2})**	**N(SO)/ΔV (10^{13} cm^{-2}/kms^{-1})**	**T_k (K) (from NH_3)**	**N(SO)/ΔV (10^{13} cm^{-2}/kms^{-1})**	**n(H_2) (10^4 cm^{-3})**
W3-IRS4(S)	19	1.93	6.3	35-45[a]	1.5 - 1.8	25 - 40
W3(OH)	12	1.38	3.8	25[a]	1.7	40
NGC2024/Orion B	10	1.04	5.1	45[b]	3	25
NGC2071SO	5	1.98	16.8	15-20[c]	7.9	3-5
VLA1623SO	12	4.22	42.7	45[d]	-	-
W51e2	16	7.69	5.6	75[e]	1.6	10
DR21(OH)	12	1.91	6.2	30-35[f]	1.3	2.5
S140SO	11	2.27	9.5	42[g]	2.5	10
NGC7538SO	8	2.62	8.2	25[h]	2.5	2

(a) Tieftrunk et al. (1998a;1998b) (b) Schulz et al. (1991); Gaume et al. (1992) (c) Calamai et al. (1982) (d) Zeng et al. (1984) (e) Ho & Young (1996); Zhang & Ho (1997b) (f) Wilson & Mauersberger (1990) (g) Ungerechts et al. (1986). (h) Jijina et al. (1999).

Table 2.5. Comparison of molecular hydrogen column density from different observations and this survey. The [SO]/[H_2] ratio is calculated in the last column for each source. The last five rows summarize the SO abundance predicted by different models, compiled by van der Tak et al. (in prep.).

Source	**N(H_2) from CO(cm^{-2})**	**N(H_2) from dust(cm^{-2})**	**N(SO) (cm^{-2})**	**[SO] / [H_2] (10^{-9})**
W3-IRS4(S)	1×10^{23} (a) 1.4×10^{23} (b)	1.3×10^{23} (b)	$0.47 - 1.9\times10^{14}$	0.3 - 1.9
W3(OH)	1.2×10^{22} (c)	3×10^{23} (b)	$0.6 - 1.4\times10^{14}$	0.2 - 11
NGC2024 / Orion B	1×10^{23} (d)	1.6×10^{23} (e)	$0.6 - 1\times10^{14}$	0.4 - 1
NGC2071SO	1.3×10^{22} (f)	1.3×10^{22} (g)	$0.6 - 2\times10^{14}$	5 - 15
VLA1623SO	1×10^{23} (h)	1.9×10^{23} (i)	4×10^{14}	2 - 4
W51e2	1.4×10^{23} (j)	7.5×10^{23} (k)	$2.2 - 7.7\times10^{14}$	0.15 - 5.5
DR21(OH)	1.2×10^{23} (l)	3.6×10^{23} (m)	$0.4 - 1.9\times10^{14}$	0.1 - 1.5
S140SO	3.3×10^{22} (n)	7.8×10^{22} (n)	$0.6 - 2.3\times10^{14}$	0.8 - 7
NGC7538SO	3.2×10^{22} (o)	2.5×10^{22} (p)	$1.2 - 2.6\times10^{14}$	4 - 10
Hot cores				4 (q)
PDRs				9 (r)
Dark clouds				20 (s)
Shocks				200 (t)
Low mass protostar				4 (u)
Gottlieb et al. (1978)				0.2 - 0.4
Rydbeck et al. (1980)				20-80
Hot shock region IC443g				0.024 (v)
Low density clouds W49, SgrB2				0.25-0.6 (x)

(a) Roberts et al. (1997) (b) Oldham et al. (1994) (c) Dickel et al. (1980) (d) Mauersberger et al. (1992) (e) Mezger et al. (1988) (f) Aoyama et al. (2001) (g) Mitchell et al. (2001) (h) Wilking & Lada (1983) (i) Motte et al. (1998) (j) Schloerb et al. (1987) (k) Sievers et al.(1991) (l) Wilson & Mauersberger (1990) (m) Richardson et al. (1989) (n) Schwartz et al. (1989) (o) Dickel et al. (1981) (p) Momose et al. (2001) (q) Sources average from Hatchell et al. (1998) (r) Orion Bar: Jansen et al. (1995) (s) L134N: Ohischi et al. (1992) (t) Orion Plateau: Sutton et al. (1995); Minh et al. (1990) (u) IRAS16293-2422: Schöier et al. (2002) (v) Turner et al. (1992) (x) Tieftrunk et al. (1994).

Table 2.6. Comparison of cloud density from LVG calculation with other observations.

Source	$n(H_2)$ from LVG	$n(H_2)$ from the literature	Beam
W3-IRS4(S)	$2.5\text{-}4\times10^5$	2×10^5 from $C^{18}O$ (a)	22"
		8.3×10^4 from dust (a)	16"
		6×10^5 from $C^{34}S$ (b)	17"
W3(OH)	4×10^5	6×10^4 from CS (c)	120"
NGC2024 /	2.5×10^5	1×10^5 from CS (c)	120"
Orion B		2×10^6 from CS (d)	~60"
NGC2071SO	$3\text{-}5\times10^4$	10^4 from NH_3 (f)	2.2'
VLA1623SO	-	3×10^5 from H_2CO (g)	60"
W51e2	1×10^5	1×10^5 from CS (c)	120"
		5×10^4 from dust (h)	30"
DR21(OH)	2.5×10^4	6×10^4 from CS (c)	120"
S140SO	1×10^5	6.4×10^5 from CS (d)	~60"
NGC7538SO	2×10^4	$1 - 2\times10^4$ from CS (j)	33"

(a) Oldham et al. (1994) (b) Tieftrunk et al. (1995) (c) Linke & Goldsmith (1980) (d) Snell et al. (1984) (f) Calamai et al. (1982) (g) Loren et al. (1989) (h) Sievers et al. (1991) (i) Chandler et al. (1993a) (j) Kameya et al. (1986).

2.4 Discussion

Here we discuss the results of the sources where both 30 and 13 GHz data are both available. The $^{34}SO(1_0\text{-}0_1)$ line are observed towards all the sources discussed here. The spectra can be found in Fig. 2.1 and 2.2. The center position of the maps are listed in Table 2.1(a).

2.4.1 W3 complex

The W3 giant molecular cloud complex is a massive and dense star-formation region. The distance of W3 is ~ 2.3 kpc (Georgelin & Georgelin, 1976). Two of the regions, W3 Main and W3(OH), have been studied extensively. On large scale, they form a ridge structure along the interface of the W3/W4 molecular clouds. Thronson et al. (1985) observed this interface and found there is almost no molecular clouds east of the interface near the W4 HII region side, and the clouds to the west of the ridge are undisturbed. Therefore they suggested that the expanding giant W4 HII region triggered the massive star forming activities in these two regions.

▪ W3 Main

Towards this region, a cluster of HII regions ionized by recently formed O and B stars (Harris & Wynn-Williams, 1976) are embedded within the W3 Main molecular cloud. IRS4 and IRS5 are infrared sources associated with the HII regions of W3 Main (Wynn-Williams et al., 1972). They are also associated with maser sources and outflows, and are believed to be the sites of an early stage of high-mass star formation (Tieftrunk et al., 1998b and reference therein). W3-IRS4(S) is a local maximum in the 800 μm map (Oldham et al., 1994). The other maxima in that map are close to IRS5 and IRS4. The center position of W3-IRS4(S) is 17" south of IRS4. This position is also close to the peak positions from the molecular line observations of ammonia (named W3 West in Tieftrunk et al., 1998a), ^{13}CO and HCO^+ (Hayashi et al., 1989), HCN (Wright et al., 1984), $C^{18}O$ (Oldham et al., 1994; Tieftrunk et al., 1995), and $C^{34}S$ (Tieftrunk et al., 1995).

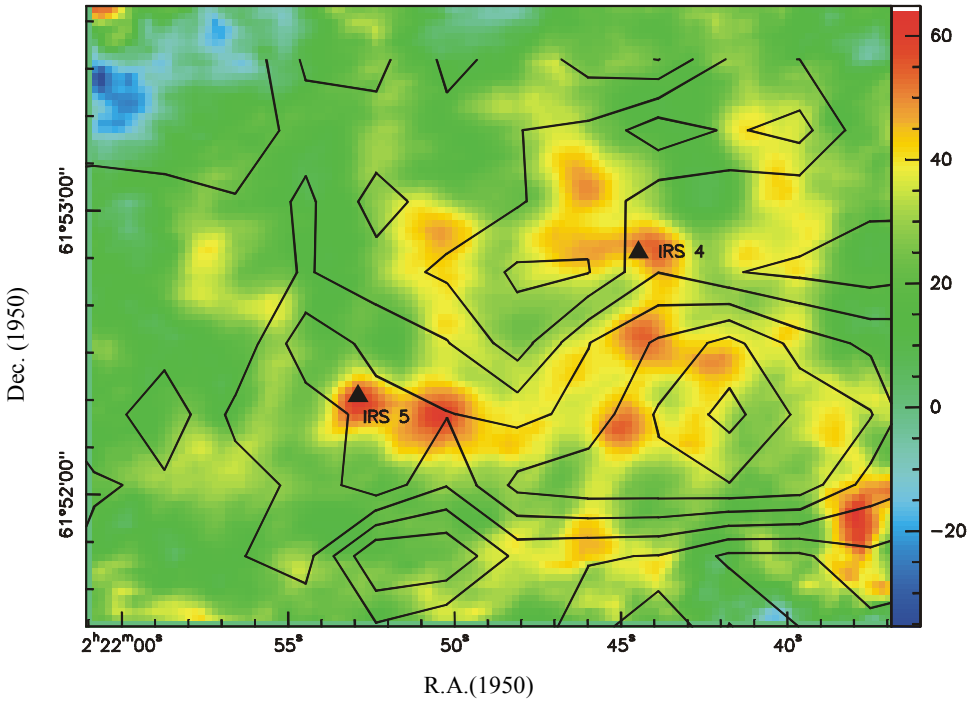

Fig. 2.4. W3 Main region. Color: $\int T_{MB}(^{13}CO)dv$ from Roberts et al. (1997). Contour: $\int T_a^*(SO(1_0 - 0_1))dv$. Contour levels from 0.5 to 2.5 by 0.5 K km/s.

From Fig.2.4, we can see that the prominent position of SO coincides with W3 West. And the spatial distribution of SO 30GHz data towards IRS4/5 region is also similar to the NH_3 (Tieftrunk et al., 1998a,b) and $C^{34}S$ (Tieftrunk et al., 1995), but quite different from ^{13}CO(1-0) (Roberts et al., 1997; Fig. 2.4) and continuum observations at long wavelength (Oldham et al., 1994). From the isotopic measurements, the opacity of ^{32}SO 30 GHz line is moderate (~ 0.4).

The velocity gradients within the region have been detected a long time ago (Lada et al., 1978; Dickel et al., 1980; Thronson et al., 1985; Hayashi et al., 1989, Tieftrunk et al., 1995). On small scales, the center velocity of the spectra changes from – 41 km/s at the western part to – 47 km/s within 70". In declination direction, V_{LSR} changes from – 42 km/s in the north to – 46 km/s in the south again within 70". This gradient is in opposite to the galactic rotation (Tieftrunk et al., 1995). We also detected such a gradient in the SO map, but with different velocity range. It is shown clearly in the position-velocity map along the R.A. direction in Fig. 2.5. There are two separate clouds, the upper one corresponding to IRS4 and lower one to IRS5. The V_{LSR} changes from – 43 km/s on IRS4 to – 40 km/s on IRS5. And the broad line profile of 30 and 13 GHz emission shown in the upper panel in Fig. 2.1(a) may come from such velocity gradient because the beam is large. Though from the lower panel in Fig. 2.1(a), we observed the broad outflow in some pixels, it is hard to extract the outflow from the intrinsic gradient from our data.

Helmich & van Dishoeck (1997) used the JCMT to observe higher level transitions of SO towards the W3 region in the 230 and 345 GHz windows with beamwidths of 21" and 15" at three positions (IRS4, IRS5, W3(OH)). SO is generally optically thick towards these regions. From the rotational diagrams, they derived $N(SO) = 1.4\times 10^{14}$ cm^{-2} on IRS-4 region with T_{rot}= 80K and $n(H_2) = 2\times 10^6$ cm^{-3}. Towards IRS5 region with isotope ^{34}SO and ^{33}SO measurements, the optical depth $\tau > 10$ is derived for the SO transitions at these frequencies. Even ^{34}SO is somewhat optically think in the region. With $S^{18}O$ line data, they derived $N(SO) = 5\times 10^{15}$ cm^{-2} on IRS5. But

in our 1cm data (Fig. 2.4), there is no prominent emission towards IRS4 and IRS5. This might be because Helmich & van Dishoeck observed higher level transitions of SO, and these transitions trace the warmer parts of the clouds. Therefore it suggests that towards these two regions, more gas is at higher temperatures (> 80 K) and denser ($n(H_2) = 2 \times 10^6$ cm^{-3}), whereas towards the W3 West region the temperature is lower (< 50 K) and less dense ($n(H_2)$ = several $\times$ 10^5 cm^{-3}). The kinetic temperature from ammonia data by Tieftrunk et al. (1998a) is also significantly lower than those from other molecular tracers in the literature. These data support our suggestion.

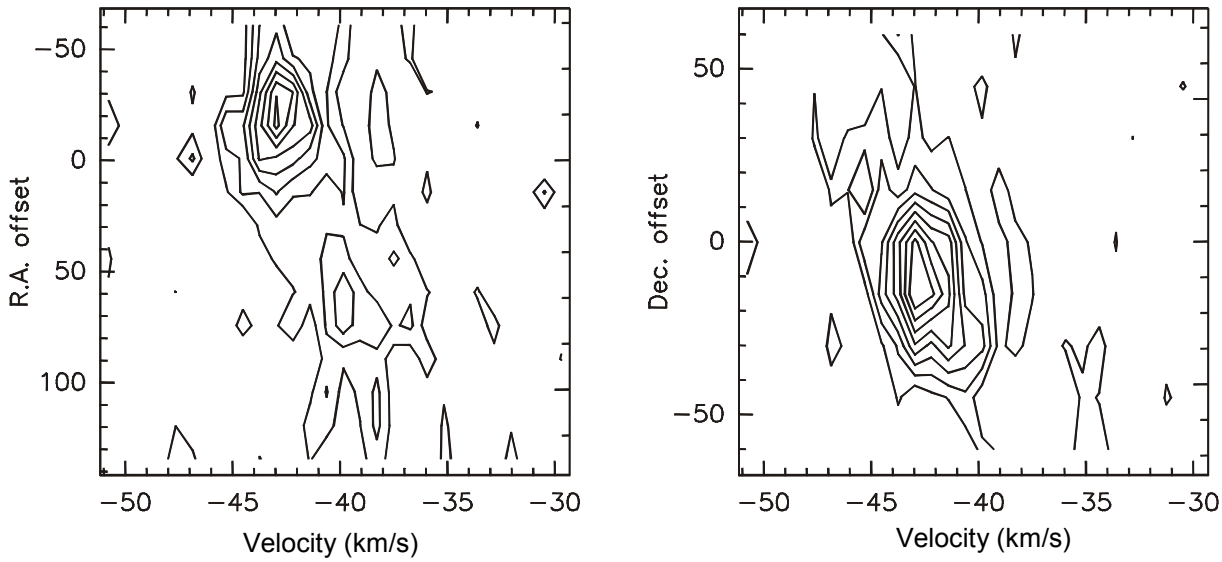

Fig. 2.5. Position-velocity maps of SO 30GHz emission towards W3 Main region. Left: Along the Δ(Dec.) = 0 line. Right: Along the Δ(R.A.) = -16" line. The contour levels are from 0.1 to 0.7 K with interval of 0.1 K. All offset distances are relative to the coordinate in Table 2.1(a).

▪ W3(OH)

W3(OH) region lies 13' southeast of W3 Main. It is named after the bright OH maser emission (Reid et al., 1980) associated with a shell-like ultracompact HII region (Dreher & Welch, 1981). W3(H_2O) is a group of water masers 6" east of W3(OH) (Moran et al., 1973; Genzel et al., 1978). These very dense clouds are well-known active star-forming regions. The central region is presumably the location of a massive star.

Towards the W3(OH) region, the SO spatial distribution is concentrated on the regions south of the OH and H_2O masers, coinciding with the Cloud A in ammonia observation by Wilson et al. (1991). In Fig 2.6 we see the two high velocity wings situated symmetrically from the peak position, with the blue component in the north-east, coinciding with the densest parts W3(OH) center, and the red in the south-west. They may be either associated with the rotation of the large scale molecular gas around W3(OH) and W3(H_2O) UCHII regions (Wilson et al., 1991), or the outflowing gas. With only SO data, we cannot tell which one is more plausible. If they are single cloud in rotation, the mass of the cloud is ~ 1200 $M_\odot$ by assuming that the cloud is in the virial equilibrium and neglecting the magnetic field.

In Fig. 2.1(b), one can see that the 13 GHz line profile is blueshifted with respect to the 30GHz line. It implies that the circumstance where the blue outflow exists is denser than the red counterpart. Therefore we see stronger 13 GHz emission in the velocity range. From Fig. 2.6 one

can see the blue outflow coincides the densest parts around W3(OH) center, whereas the red outflow is in the opposite direction. The peak position is right at the center.

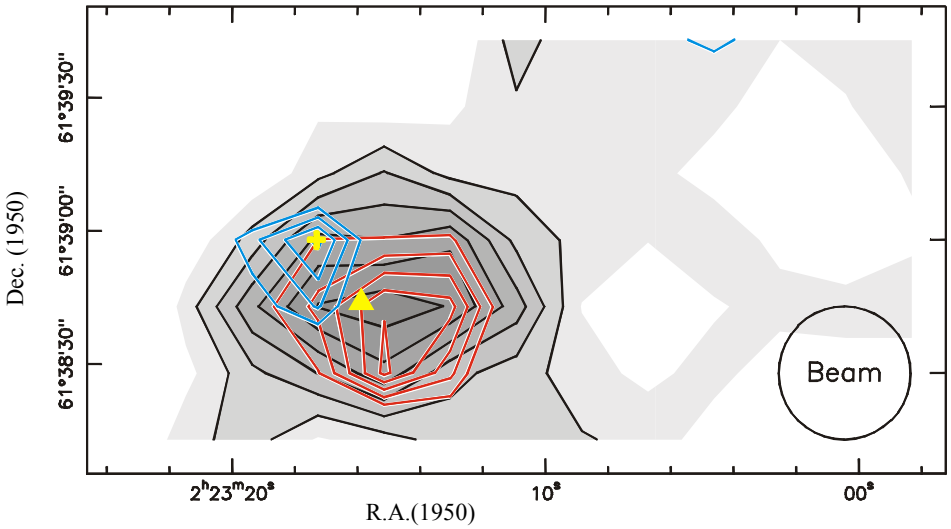

Fig. 2.6. W3(OH) region. Blue (–52 to –48 km/s) and red (–44 to –40 km/s) wings (contour) traced by SO 30 GHz emission overlay on the total integrated intensity (greyscale). All in T_a^* scale. The lowest contour level is 0.5 K km/s with interval of 0.1 K km/s. The peak position is marked by a triangle. W3(OH) is marked by "+".

According to Helmich & van Dishoeck (1997), the higher level SO emissions are also very intense. From ^{34}SO observations, the temperature can be constrained to T_k >100K and n(H_2) > 2×10^6 cm^{-3}. The estimated column density N(SO)= 1.3×10^{15} cm^{-2} is 10 times higher than our result. We cannot account for all the difference in the column density by the difference in beamwidth (15" to 22" at JCMT vs. 30" to 60" at Effelsberg). We suggest that towards the W3(OH) region, there are two different layers with different temperature and density. And the less dense and lower temperature parts of the clouds are traced in our survey.

2.4.2 NGC 2024/ Orion B region

NGC2024 is known to be a prominent site of on-going star formation. It is part of the Orion B Giant Molecular Cloud, situated at a distance of 320 (near edge) to 500 (far edge) pc (Anthony-Twarog, 1982; Brown et al., 1994). It includes a ridge of dense molecular material with a number of protostars with outflows close to the well-known HII region (Sanders & Willner, 1985; Richer et al., 1992; Chernin, 1996). Our center position is 8" southeast of the 1.3mm peak FIR5 (Mezger et al., 1988). FIR5 is supposed to be the driving source of a highly collimated unipolar outflow extended more than 250 arcsec to the south-west (Richer et al., 1992). In addition to this strong outflow, Richer (1990) and Chernin (1996) found three other outflows in the FIR5 and FIR6 region in high resolution observations.

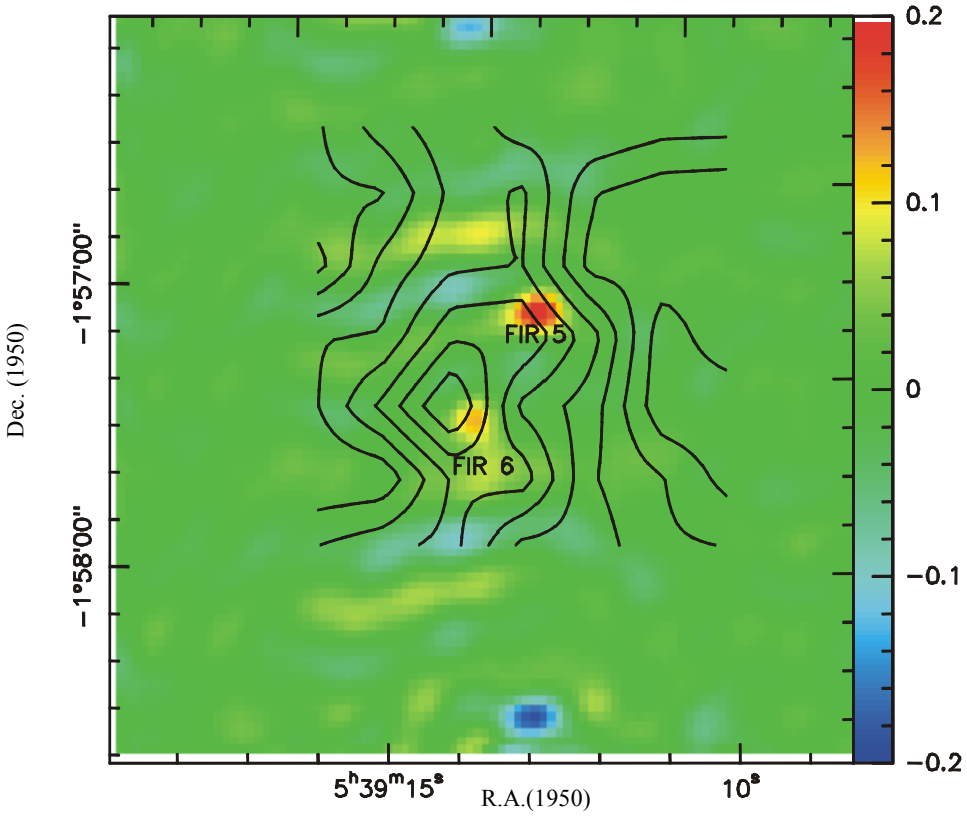

Fig. 2.7(a). NGC2024 region. Color: 2.7mm continuum emission from Wilson et al. (1995) at BIMA. Contours: $\int T_a^*(SO(1_0 - 0_1)dv$, with contour levels from 0.2 to 1.8 by 0.2 K km/s.

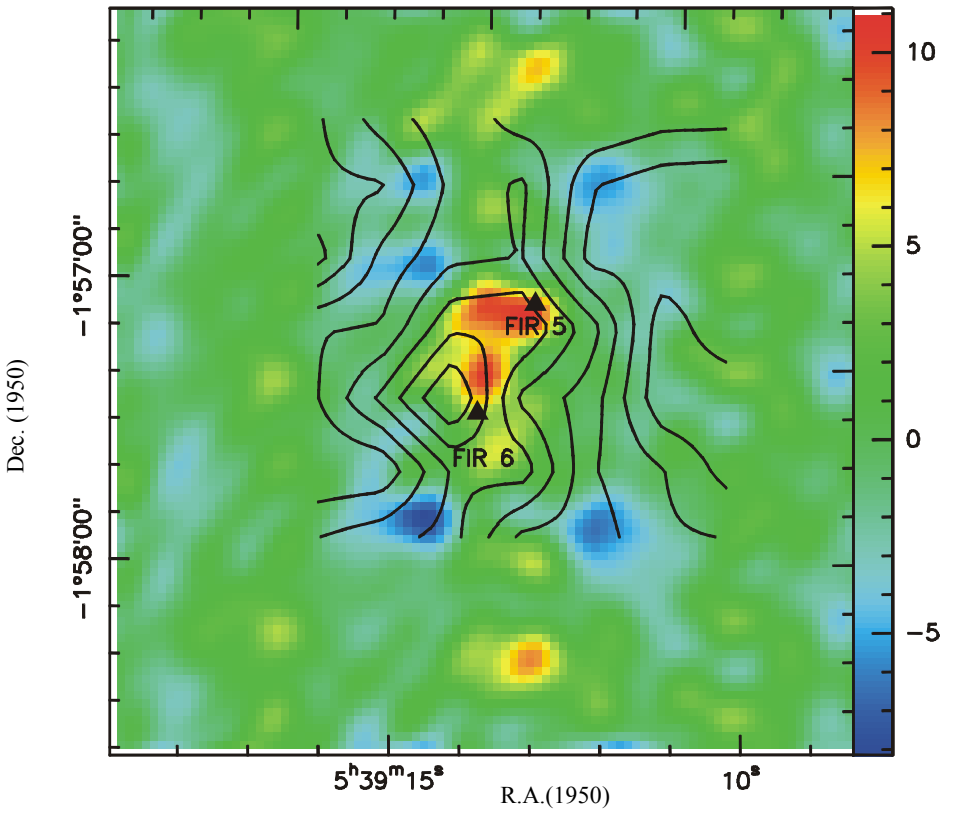

Fig. 2.7(b). NGC2024 region. Color: $\int T_{MB}(C^{18}O)dv$ from Wilson et al. (1995) at BIMA. Contours: $\int T_a^*(SO(1_0 - 0_1)dv$, with contour levels from 0.2 to 1.8 by 0.2 K km/s.

In Fig. 2.7(a) and (b) the SO map is overlaid on the 2.7 mm continuum and $C^{18}O$ data from the BIMA array (Wilson et al., 1995). The sources FIR5 and FIR6 are clearly shown in Fig. 2.7(a) in the continuum map. And the strong collimated outflow is outside the map area at the south-east side. In the SO 30GHz map, the peak emission region is north-east of FIR6, close to the blueshifted outflowing gas in east-west direction. From the map of Chernin (1996), the pixel at the peak position should include the blueshifted outflow and the other two redshifted outflows are included in the pixel 15" west of the peak position. In Fig. 2.1(c) we see only the redshifted outflows are obvious. The spectrum at the peak position is very narrow. It is possible that we subtracted the outflow feature as baseline in the data reduction. Or the region is less dense so that we see weaker SO emission. In the upper panel of Fig. 2.1(c), the 30 GHz spectum smoothed into 60" at the center position shows a broad line profile, whereas the 13 GHz SO emission at the center position seems to be narrower. But it might be because the signal-to-noise ration is low. Since the outflowing gas should included in the 60" beam, it might be the density around the outflow is too low to excite the 13 GHz emission. One needs better S/N data to check this point.

Barnes & Crutcher (1992) observed the higher level SO(2_2-1_1) 86 GHz line towards this region with BIMA array 11" × 7" resolution. This line should trace denser and warmer gas. The spatial distribution of the SO(2_2-1_1) transition is very similar to SO(1_0-0_1) but more compact. And the outflow feature is also absent or hard to distinguish. We suggest the envelope of this region is very cold.

With multiline observations of CS by Snell et al. (1984) (beam ~ 60") and Schulz et al. (1991) (beam ~ 8"), the CS and SO data show good correlations. The density n(H_2) is ~ 2×10^6 cm^{-3} estimated by Snell et al., which is 10 times higher than that derived from the SO data. On the other hand, compared with the results from lower level CS transitions by Linke & Goldsmith (1980) (beam ~ 120"), our density is in good agreement with the. Snell et al. suggest the difference comes from different emission region. It seems that the higher level CS emission comes from denser regions. The SO(1_0-0_1) emission is close to the low level CS emission.

2.4.3 NGC2071

The NGC2071 star-forming region also belongs to the Orion B molecular cloud complex. The distance of NGC2071 is ~390 pc (Anthony-Twarog, 1982). The center position of the observation is offset by (-150",+100") northwest from the reflection nebula NGC2071. The local dominant SO(1_0-0_1) maximum position is reported by Schmid-Burgk & Muders (1994). These authors find that the SO 30GHz emission is extremely extended, around the end of the CO outflow (see Fig.4 in Schmid-Burgk & Muders (1994) for the source size and relative position to the outflow center). The peak position of strong SO 13 and 30GHz emissions is offset from the bipolar outflow axis (Snell et al., 1984). It coincides with the submillimeter source OriBsmm6 identified in the continuum observation by Mitchell et al. (2001) at 850μm.

Only the center 90" ×90" region is included in the survey. The velocity range from 8 to 11 km/s in SO 30 GHz is in good agreement to the outflow traced by ^{13}CO (Snell et al., 1984). Thus we suggest the two emission are associated. In the 30 GHz spectra, one can see broad blue wings in the spectra in Fig. 2.1(d). And the intensity of the wing is very stable through the whole map. The red wings in the 30GHz spectra are narrower, and the intensity is higher to the northern region. But in the 13 GHz spectrum, the redshifted wing is broader. We suggest the density around the redshifted gas is denser than that of the extended blueshifted gas. This implies that the outflowing gas may originate from different sources.

Chernin & Masson (1993) observed the SO(6_5-5_4) 220 GHz line. The emission is more compact and traces closely the bipolar outflow shown in the two regions of CO map. The velocity and spatial distribution are totally different from the low level SO emission. Therefore they are independent. Towards the NGC2071 region, the spatial distributions of CS and SO are very different (Schwartz et al., 1983). The difference is propably due to a temperature effect with distance from the center of the source. The SO low level transitions are unique in this case.

2.4.4 VLA1623

VLA1623 is a compact VLA continuum source and Class 0 protostellar candidate centered on a well-collimated molecular outflow in ρ Oph-A molecular cloud at a distance of 160 pc (Bertiau, 1958; Wilking, 1992). This active low mass star-forming region is one of the closest molecular clouds. It harbours a rich cluster of young stellar objects at various evolutionary stages. Our central position is at the tip of the redshifted molecular lobe of VLA1623 near GSS30 IRS-3 (LFAM1), which is a new low-mass Class 0 protostar according to Motte et al. (1998). Like in NGC2071, the SO(1_0-0_1) emission is concentrated on the edge of the outflow gas, but not along the direction of the outflow. For the large scale distribution and the relative position of the outflow, please see Fig. 3 in Schmid-Burgk & Muders (1994).

The prominent position of the SO 30 GHz line is ~30" north of the center position. Our results from SO show that VLA1623 is a unique region from many aspects. First, the line profiles in 30 and 13 GHz transitions are almost identical. We failed to have a solution in LVG program because the intensity ratio of the two lines is close to one. From the ^{34}SO observation, we derived very high opacity for the ^{32}SO 30 GHz transitions (Table 2.1(b)). Furthermore, the ^{34}SO spectrum is blueshifted from the ^{32}SO line by 0.2 km/s and shows a weak broad redshifted wing in Fig. 2.2. Since ^{32}SO line is optically thick, the difference in velocity in two lines should come from self-absorption in the optically-thick ^{32}SO line. This phenomenon could also explain why we cannot find a solution in LVG program and the results from the rotational diagram is also suspicious. Though ^{32}SO 30 GHz is optically thick, the line is still narrow, especially at the prominent region. In Fig. 2.1(e) one can see a week broad redshifted wing (v > 3.3 km/s) in the spectra through the whole region.

SO is generally enhanced at the interface of outflows and dense cloud. From the large scale, the CO highly-collimated outflow is from the south-east edge in the map to the (-100,0) position at the west edge. We see that the emission of the SO 30 GHz line distributes around the outflow and the prominent position of SO is at the north-east side of it. On small scales, the spatial distribution of SO emission is similar to that of the SO_2 (3_{22}-2_{11}) line with the same resolution performed by Wootten & Loren (1988). The line profile of SO is also similar to that of the SO_2 (3_{13}-2_{02}) and (3_{22}-2_{11}) lines. Since the SO line is narrow and SO_2 is generally believed to be produced via the SO molecule, we think the local SO enhancement would be the result of the interaction of the two outflows, the strong CO outflow and the other outflow centered on the protostar GSS30 as proposed by Wootten & Loren (1988). Tamura et al. (1990) and Zhang et al. (1997) detected successfully the outflows centered on GSS30. This might explain the extremely high opacity of the SO line towards this region. But besides GSS30, there are several infrared sources crowding the region, for example LFAM1 and CRBR12. The latter is propably a Class II candidate as proposed by Comerón et al. (1993). More evidence is needed to make a more clear conclusion on the kinematics of this region.

The situation of VLA1623 is very similar to NGC2071 in many respects. The prominent regions of SO are located near but out of the highly-collimated outflow. The opacity of SO 30

GHz emission is high. One of the high-velocity component exists in the whole area. But towards VLA1623, the gas we observed is denser than NGC2071.

2.4.5 W51e1/e2 region

W51 complex is a giant molecular cloud and massive star-forming region located in the Sagittarius spiral arm at ~7 kpc (Genzel et al., 1981). In the high resolution centimeter observations towards W51, several discrete components are detected in the 6cm band and assigned as W51a to W51g (Martin, 1972). From the IR observations (Wynn-Williams et al. 1972), the peaks IRS1 and IRS2 coincide with W51e and W51d, respectivelyLocated west of W51e by 30", W51e1 and e2 are two small ultra-dense contracting molecular cores with mass ~10^2 $M_\odot$ (Scott, 1978). . In this survey we observed only the W51e region. In our observation we cannot resolve e1 and e2.

As seen in Fig. 2.1(f), the linewidth is wide ($\Delta V > 10$ km/s) as seen in other molecules. The center velocity changes from the SE to the NW region. The velocity range of 30 GHz and 13 GHz lines is similar. The linewidth of the 30GHz line is larger than that of the 13 GHz line, but narrower than that of the CO line (~ 45-75 km/s). One can see in the lower panel in Fig. 2.1(f), the V_{LSR} changes from 53 km/s in the SE to 61 km/s in the NW of the map. Like W3-IRS4(S), the center velocity of SO emission changes within the clouds as the other high density tracer like $C^{18}O$ and $C^{34}S$, reflecting the complicated structure of the cloud.

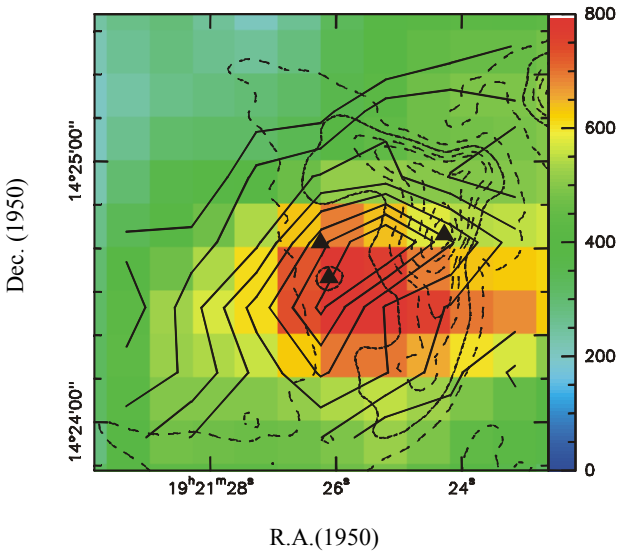

Fig. 2.8. W51e1/e2 region. Comparisons of $\int T_{MB}(^{13}CO)dv$ (color, Okumura et al., 2001), $\int T_a^*(SO(1_0 - 0_1)dv$ (solid contours; contour levels from 4 to 11 K km/s with 1K km/s interval) and 6cm continuum emission (dashed contours, Mehringer, 1994. Contour levels at 0.07, 0.17, 0.31, 0.45, 0.75, 1.05, 1.35 Jy/5" beam). The triangles mark the positions of W51e in the west, W51e1 in the south and W51e2 in the map center.

The spatial distribution of SO is extended around the W51e region. The peak position of the integrated intensity are W51e and W51e1/e2. From the velocity-position map, it seems that two components have different center velocity. The former is V_{LSR} = 58 km/s and the latter V_{LSR} = 53 km/s. Compared with the SO(2_2-1_1) 87 GHz maps by Rudolph et al. (1990), the two SO

transitions (30, 87 GHz) have similar line profiles on W51e2. But the emission of the SO(2_2-1_1) transition is restricted to the W51e1/e2 region and shows little emission towards W51e. This implies the density around W51e1/e2 is higher.

The wide profile could be the result of large beam, as many different clouds blend into one spectrum. Due to the far distance and complicated structure of the region, most star-forming related phenomena here have to be studied at high resolution.

2.4.6 DR21/W75S region

DR21(OH) is a star-forming region at a distance of ~3 kpc in the north-eastern part of the giant Cygnus-X HII complex (Campbell et al., 1982). It contains very dense and highly obscured material and is believed to be at an early evolutionary stage. The survey from CS and ammonia shows a NS ridge structure towards this region (Wilson & Mauersberger, 1990). This region is also referred to as W75S. Our center position is on DR21(OH)M (Mangum et al., 1991). There are several other continuum sources DR21(OH)W and DR21(OH)S in the the map. With high resolution interferometer observations, DR21(OH)M can be resolved into two independent sources MM1 in the north-east and MM2 in the south-west. Both are associated with OH and H_2O masers and separated by 8". They are quite different objects. The V_{LSR} ranges corresponding to MM1 is from – 4.1 to – 9.5 km/s and MM2 is +1.3 to – 4.1 km/s (Woody et al., 1989; Padin et al., 1989; Mangum et al., 1991).

The velocity range of the SO 30 GHz spectrum is between +2 to –7 km/s. And the spatial distribution of the integrated intensity map shows the NS ridge structures too (Fig. 2.1(g)). In contrast to many other transitions like $C^{32}S$(1-0), $C^{32}S$(2-1) and NH_3, which show high opacity and self-absorption features ($C^{32}S$: Chandler et al., 1993b; NH_3: Mangum et al., 1992), we derived low opacity for ^{32}SO emission towards this region (Fig. 2.2). In the 13 GHz line profile, one can see the center velocity is redshifted. The velocity range of the 13 GHz spectrum is similar to that of the MM2 source. It may suggest that the 13 GHz originates from MM2 and the density of MM2 is larger than that of MM1. Therefore it can excite more intense 13 GHz emission than MM1. The suggestion about the density is consistent with the calculations by Mangum et al. (1991).

Compared to CS(1-0), CS(2-1) observations by Chandler et al. (1993b) with beamwidth of 36" and 18" respectively, the peak emission position of SO 30GHz line coincides with CS(1-0), located between DR21(OH)M and DR21(OH)W. The similarity between the $C^{34}S$(2-1) and the SO 30 GHz, both are optically-thin, profiles is striking (see §3.4.5 and Fig. 3.13). It seems they trace the same parts of the cloud, though the critical density of CS(2-1) is much higher than SO(1_0-0_1). It is interesting to investigate this point in the future.

2.4.7 S140SO

S140 is a crescent shaped HII region bordering the edge of the dark cloud L1204. It is a massive star-forming region adjacent to an edge-on photon dominated region, powered by the nearby B0 star HD211880. It lies at a distance of ~ 910 pc (Crampton & Fisher, 1974). The center position of our observation is ~15" north-east of S140-IRS1, or ~10" east of S140-IRS2 (Beichman et al., 1979). It coincides with SMM2, a dense compact core identified by dust continuum emission at 450 μm (Minchin et al., 1995).

The isotopic $^{34}SO(1_0\text{-}0_1)$ line was measured at the peak position. We derived moderate opacity for ^{32}SO line (~ 0.5). The SO emission is extended and one of the local prominent

position is located at the west of the center by ~ 20". This peak position is very close to IRS2. It also at the direction of the redshifted P.A.= 340° CO outflow centered on IRS1, but it is far from the ^{13}CO peaks (Minchin et al., 1993; Weigelt et al., 2002). The velocity range of the SO emissions are between –11 to –4 km/s. In the CS survey by Hayashi et al. (1985) and Zhou et al. (1994), there are blue wings beyond v = –11 km/s, but we do not see them in the spectra. The data from CS(1-0) shows different distribution from that of SO (Hayashi et al., 1985; beamwidth ~ 33"). The SO emission is different from all other molecules in spatial distribution. S140 region is an unusual case.

The spectrum of the SO 30 GHz line is not symmetric. In the mapped region, we see only redshifted (v = –6 to –3 km/s) wing in the spectra but not at the blueshifted side. The center velocity of the 13 GHz emission is redshifted from that of the 30 GHz. This suggests the redshifted emission should originate from denser region, probably from the interaction between the redshifted outflow from IRS1 and the quiescent dense gas.

The SO (2_2-1_1) 86 GHz line observation with ~ 8" beamwidth by Wilner & Welch (1994), it shows similar V_{LSR} and linewidth to the 30 GHz line. No emission was detected related to the outflow velocity either. But the spatial distribution of 86 GHz is limited around the peak position. At this position, they derived N(SO)= 7.6×10^{14} cm^{-2} under LTE assumption and T_{ex}= 67 K. Clearly this transition traces warmer parts of the clouds.

2.4.8 NGC7538SO

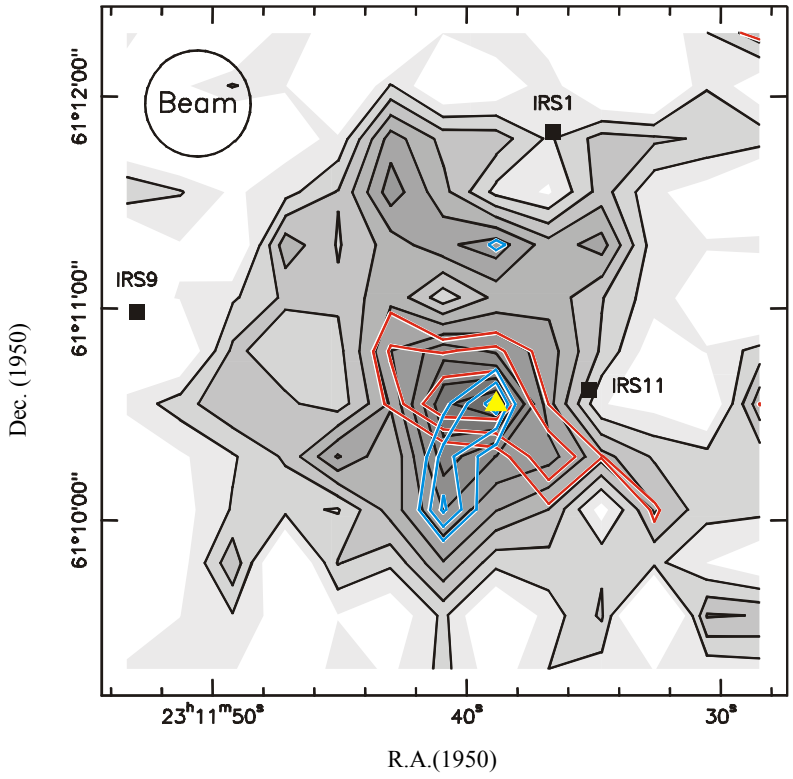

Fig. 2.9. NGC7538 region. Blue (–61 to –58 km/s) and red (–55 to –52 km/s) wings overlay on the total integrated intensity of SO(1_0-0_1) emission (greyscale). All in T_a^* scale. The lowest contour level is 0.9 K km/s for the red and 1.4 K km/s for the blue contours with 0.2 K km/s. The peak position in total intensity is marked by a triangle. The infrared sources IRS1, IRS9, and IRS11 are also shown.

The NGC 7538 molecular cloud is an active site of high-mass star formation. It is situated at a distance of 2.8 kpc in the Perseus arm (Scoville, 1986). It contains several pointlike infrared sources with outflows. Our central position is between three of the remarkable infrared sources IRS 1, IRS9 and IRS11 (Werner et al., 1979). IRS1 and IRS11 also show strong emission in submillimeter survey (Momose et al., 2001).

We have similar resolution to the CS(1-0) observations by Kameya et al. (1986) (~ 30"). We found that the spatial distribution of SO 30GHz resembles that of CS(1-0). The peak of the SO 30GHz emission coincides with the peak **C** in the CS(1-0) map, ~ 20" east of IRS 11 and IRS11(OH) (Forster et al., 1978). The linewidth of the SO 30 GHz line at **C** is comparable to CS (~4.8 kms^{-1}), but we failed to detect the high-velocty gas beyond –50 km/s at the redshifted side and beyond –62 km/s at the bluesfhifted side. The source size derived from the 30GHz observations is also comparable to that of CS(1-0). The SO emission is distributed between the east of IRS1 and IRS11 and the west of IRS9 (Fig. 2.9). Comparing the map of the high-velocity flows (Fig.3 in Kameya et al., 1989), it seems that the SO emission is restricted to an approximatedly circular region confined by the outflowing gas centered on these three sources.

2.4.9 Summary

From the SO(1_0-0_1) survey, we observed that there are two noteworthy properties of the SO 30 GHz emission. The first is that it often arises from cold dense regions, though the critical density of the SO 30 GHz transition is low (n ~ 10^4 cm^{-3}). Towards the W3(OH) region, the W3 Main region, the W51e1/e2 region, the DR21(OH) region, and the NGC 7538 region, the SO 30 GHz line has similar spatial distribution and line profiles to those of high density tracers like ammonia and CS. The second is that the emission is often enhanced towards shock regions, e.g. the NGC 2024 region, the NGC 2071 region, the VLA1623 region, and the NGC 7538 region. One observes extended SO 30 GHz emission towards the shocked regions, and the peak of the SO emission is often near the tip but outside the outflowing gas traced by CO. The optical depth of the SO 30 GHz line is high towards these positions. Combining the two features suggests that the SO molecule originates from shocked regions and stays for long time in quiescent gas. We can then observe its emission if excitation conditions are suitable.

2.5 The abundance of SO

Sulphur chemistry in molecular clouds has been studied by a considerable number of authors (Oppenheimer & Dalgarno, 1974; Hartquist et al., 1980; Prasad & Huntress, 1982; Watt & Charnley, 1985; Herbst & Leung, 1989; Millar & Herbst, 1990; Pineau des Forêts et al., 1993). Theoretical models suggest that in an oxygen-rich environment, the abundance of SO is larger than in a carbon-rich environment, where CS is preferred. But in regions with very high free oxygen abundance, SO is converted into SO_2. Because CS and SO_2 are relatively stable, CS and SO_2 will be the sink of carbon/sulphur atoms and oxygen/sulphur atoms. Therefore it is interesting to measure the relative abundance of these molecules.

To obtain a reliable abundance for a molecule, it is preferable to having data with similar resolution. Then the opacity effect has to be corrected carefully. It is most important to ensure that the compared molecules originate from the same part of the molecular cloud. SO(1_0-0_1) and (1_2-1_1) are low level transitions and generally trace the more dense and cold parts of the clouds as discussed in §2.4. And we have shown that SO is probably produced at the interface between

outflowing gas and the dense clouds (e.g. the shock chemistry models by Pineau des Forêts et al., 1993). These SO molecules may diffuse to the other parts of the cloud. Therefore the abundance would be more reliable if we can also find the correct tracer for molecular hydrogen in a similar environment. In Table 2.5 we chose $C^{18}O$ and continuum observations at mm wavelength as the best tracer for such colder molecular hydrogen. This is another uncertainty when converting $C^{18}O$ to molecular hydrogen density, because the ratio may change in different environment.

Since the sulphur chemistry is still poorly understood, it is hard to discuss the uncertainty in the calculations. Here we tried to compare the results with the others.

In our observations, the SO abundance is $\sim 10^{-10}$ to 10^{-8}. NGC2071SO, NGC7538 and VLA1623 are the sources with the highest SO abundance in the survey, and these sources are also ones with strong outflows. Therefore SO and H_2 may not mix well in the regions and show high abundances. Using the column density of SO data in Gottlieb et al. (1978) together with the estimated values for $n(H_2)$ by other observations, the abundance of SO is 2 to 4×10^{-10} in W3(OH), W51 and DR21(OH) regions. The data by Barnes & Crutcher (1992) on NGC2024 gives us the abundance in the order of several 10^{-9}. The results seems to be consistent. The data complied by van der Tak et al. (2003) are also shown at the end of Table 2.5 as representative cases of various circumstances. The SO abundance for most sources in our survey seems lower.

The low abundance might indicate that most sources we investigated are in relatively "early times" of the evolution phase as predicted by some sulphur chemistry models or there is depletion in oxygen in these sources (Prasad & Huntress, 1982). Besides, the cosmic ray and X-ray ionization would also affect the SO abundance. And there is still a large uncertainty in the SO abundance due to different resolutions in different lines in being compared. With only data of two SO transitions, it is hard to give a definite conclusion.

The relative abundance of SO to H_2S, OCS, CS and SO_2 with the same resolution should be explored later to see if our survey of SO transitions at lower levels is in favor of any existing chemical models. To check with the shock chemistry models (Pineau des Forêts et al., 1993), the SiO abundance should also be measured. These investigations might improve our knowledge about sulphur chemisty.

References

Anthony-Twarog, B., 1982, ApJ, 87, 1213.

Aoyama, H., Mizuno, N., Yamamoto, H., Onishi, T., Mizuno, A., Fukui, Y., 2001, PASJ, 53, 1053.

Bachiller R., Pérez Gutiérrez, M., Kumar, M. S. N., Tafalla, M., 2001, A&A, 372, 899.

Barnes, P. J., Crutcher, R. M., 1992, ApJ, 389, 325.

Beichman, C.,A., Becklin, E. E., Wynn-Williams, C. G., 1979, ApJ, 232, L47.

Bertiau, F. C, 1958, ApJ, 128, 533.

Blake, G. A., Sutton, E. C., Masson, C. R., Phillips T. G., 1987, ApJ, 315, 621.

Brown, A. G. A., de Geus, E. J., de Zeeuw, P. T., 1994, ApJ, 289, 101.

Calamai, G., Felli, M., Giardinelli, S., 1982, A&A, 109, 123.

Campbell, M. F., Hoffmann, W. F., Thronson, H. A. Jr., Niles, D., Nawfel, R., Hawrylycz, M., 1982, ApJ, 261, 550.

Carral, P., Welch, W. J., 1992, ApJ, 385, 244.

Chandler, C. J., Gear, W. K., Chini, R., 1993a, MNRAS, 260, 337.

Chandler, C. J., Moore T. J. T., Mountain, C. M., Yamashita, T., 1993b, MNRAS, 261, 694.

Charnley, S. B., 1997, ApJ, 481, 396.
Chernin, L. M., 1996, ApJ, 460, 711.
Chernin, L. M., Masson, C. R., 1993, ApJ, 403, L21.
Chernin, L. M., Masson, C. R., Fuller, G. A., 1994, ApJ, 436, 741.
Clark, W. W., DeLucia, F. C., 1976, J. Molec. Spectrosc., 60, 332.
Codella, C., Muders, D., 1997, MNRAS, 291, 337.
Codella, C., Bachiller, R., 1999, A&A, 350, 659.
Comerón, F., Rieke, G. H., Burrows, A., Rieke, M. J., 1993, ApJ, 416, 185.
Crampton, D., Fisher, W. A., 1974, Pub. Dom. Ap. Obs. 14, 12.
Cummins, S. E., Linke, R. A., Thaddeus, P., 1986, ApJS, 60, 819.
Dickel, H. R., Dickel, J. R., Wilson, W. J., Werner, M. W., 1980, ApJ, 237, 711.
Dreher, J. W., Welch, W. J., 1981, ApJ, 245, 857.
Forster, J. R., Welch, W. J., Wright, M. C., Baudry, A., 1978, ApJ, 221, 137.
Frerking, M. A., Langer, W. D., Wilson, R. W., 1982, ApJ, 262, 590.
Friberg, P., 1984, A&A, 132, 265.
Gaume, R. A., Johnston, K. J., Wilson, T. L., 1992, ApJ, 388, 489.
Genzel, R., Downes, D., Moran, J. M., Johnston, K. J., Spencer, J. H., Walker, R. C., Haschick, A., Matveyenko, L. I., Kogan, L. R., Kostenko, V. I., Rönnäng, B., Rydbeck, O. E. H., Moiseev, I. G., 1978, A&A, 66, 13.
Genzel, R., Downes, D., Schneps, M. H., Reid, M. J., Moran, J. M., Kogan, L. R., Kostenki, V. I., Matveyenko, L. I., Rönnäng, B., 1981, ApJ, 247, 1039.
Georgelin, Y. M., Georgelin, Y. P., 1976, A&A, 49, 57.
Goldsmith, P. F., Langer W. D., 1999, ApJ, 517, 209.
Gottlieb, C. A., Ball, J. A., 1973, ApJ, 184, L59.
Gottlieb, C. A., Gottlieb, E. W., Litvak, M. M., Ball, J. A., Penfield, H., 1978, ApJ, 219, 77.
Green, S., 1994, ApJ, 434, 188.
Hartquist, T. W., Oppenheimer, M., Dalgarno, A., 1980, ApJ, 236, 182.
Harris, S., Wynn-Williams, C. G., 1976, MNRAS, 174, 649.
Hatchell, J., Thompson, M. A., Millar, T. J., MacDonald, G. H., 1998, A&A, 338, 713.
Hayashi, M., Omodaka, T., Hasegawa, T., Suzuki, S., 1985, ApJ, 288, 170.
Hayashi, M., Kobayashi, H., Hasegawa, T., 1989, ApJ, 340, 298.
Hayashi, M., Murata, Y., 1992, PASJ, 44, 391.
Heithausen, A., Corneliussen, U., Großmann, V., 1995, A&A, 301, 941
Heithausen, A., Corneliussen, U., Großmann, V., 1998, A&A, 330, 311.
Helmich, F. P., Jansen, D. J., de Graauw, Th., Groesbeck, T. D., van Dishoeck, E. F., 1994, A&A, 283, 626.
Helmich, F. P., van Dishoeck, E. F., 1997, AAPS, 124, 205.
Henning, Th., Michel, B., Stognienko, R., 1995, Planet., Space Sci., Vol. 43, Nos. 10/11, 1333.
Herbst, E., Leung, C. M., 1989, ApJSS, 69, 271.
Ho, P. T. P., Young, L., M., 1996, ApJ, 472, 742.
Jansen, D. J., Spaans, M., Hogerheijde, M. R., van Dishoeck, E. F., 1995, A&A, 303, 541.
Jijina, J., Myers, P. C., Adams, F. C., 1999, ApJS, 125, 161.
Kameya, O., Hasegawa, T. I., Hirano, N., Tosa, M., Taniguchi, Y., Takakubo, K., 1986, PASJ, 38, 793.
Kameya, O., Hasegawa, T. I., Hirano, N., Takakubo, K., 1989, ApJ, 339, 222.
Lada, C. J., Elmegreen, B. G., Cong, H.-I., Thauddeus, P., 1978, ApJ, 226, L39.
Leen, T. M., Graf, M. M., 1988, ApJ, 325, 411.

Linke, R. A., Goldsmith, P. F., 1980, ApJ, 235, 437.
Loren, R. B., Sandqvist, Aa. Wootten, A., ApJ, 1983, 270, 620.
Mangum, J. G., Wootten, A., Mundy, L. G., 1991, ApJ, 378, 576.
Mangum, J. G., Wootten, A., Mundy, L. G., 1992, ApJ, 388, 467.
Martin, A. H. M., 1972, MNRAS, 33, 289.
Martin-Pintado, J., Bachiller, R., Fuente, A., 1992, A&A, 254, 315.
Mauersberger, R., Wilson, T. L., Mezger, P. G., Gaume, R., Johnson, K. J., 1992, A&A, 256, 640.
Mezger, P. G., Chini, R., Kreysa, E., Wink, J. E., Salter, C. J., 1988, A&A, 191, 44.
Minh, Y. C., Irvine, W. M., McGonagle, D., Ziurys, L. M., 2000, MNRAS, 316, 152.
Millar, T. J., Herbst, E., 1990, A&A, 231, 466.
Minchin, N. R., White, G. J., Padman, R., 1993, A&A, 277, 595.
Minchin, N. R., Ward-Thompson, D., White, G. J., 1995, A&A, 298, 894.
Mitchell, G. F., 1984, ApJ, 287, 665.
Mitchell, G. F. Johnstone, D., Moriarty-Schieven, G., Fich, M., Tothill, N. F. H., 2001, ApJ, 556, 215.
Momose, M., Tamura, M., Kameya, O., Greaves, J. S., Chrysostomou, A., Hough, J. H., Morino, J.-I., 2001, ApJ, 555, 855.
Moran J., M., Papadopoulos, G. D., Burke, B. F., Lo, K. Y., Schwartz, P. R., Thacker, D. L., 1973, ApJ, 185, 535.
Motte, F., André, P., Neri, R., 1998, A&A, 336, 150.
Mundy, L. G., Wootten, A., Wilking, B. A., Blake, G. A., Sargent, A. I., 1992, ApJ, 385, 306.
Nilsson, A., Hjalmarson, Å., Bergman, P., Millar, T. J., 2000, A&A, 358, 257.
Ohishi, M., Irvine, W. M., Kaifu, N., 1992, in IAU 150, Astrochemistry of Cosmic Phenomena, 171.
Okumura, S.-I., Miyawaki, R., Sorai, K., Yamashita, T., Hasegawa, T., 2001, PASJ, 53, 793.
Oldham, P. G., Griffin, M. J., Richardson, K. J., Sandell, G., 1994, A&A, 284, 559.
Oppenheimer, M., Dalgarno, A., 1974, ApJ, 187, 231.
Padin, S., Sargent, A.,I., Mundy, L. G., Scoville, N. Z., Woody, D. P., Leighton, R. B., Masson, C. R., Scott, S. L., Seling, T. V., Staphelfeldt, K. R., Terebey, S., 1989, ApJ, 337, L45.
Pickett, H. M., Poynter, R. L., Cohen, E. A., Delitsky, M. L., Pearson, J. C., Müller, H. S., "Submillimeter, Millimeter, and Microwave Spectral Line Catalog", May, 2000. (http://spec.jpl.nasa.gov)
Pineau des Forêts, G., Roueff, E., Schilke, P., Flower, D. R., 1993, MNRAS, 262, 915.
Plambeck, R. L., Wright, M. C. H., Welch, W. J., Bieging, J. H., Baud, B., Ho, P. T. P., Vogel, S. N., 1982, ApJ, 259, 617.
Prasad, S. S., Huntress, W. T. Jr., 1982, ApJ, 260, 590.
Reid, M. J., Haschick, A. D., Burke, B. F., Moran, J. M., Johnston, K. J., Swenson, G. W. Jr., ApJ, 1980, 239, 89.
Richardson, K. J., Sandell, G., Krisciunas, K., 1989, A&A, 224, 199.
Richer, J. S., 1990, MNRAS, 245, 24p.
Richer, J. S., Hills, R. E., Padman, R., 1992, MNRAS, 254, 525.
Roberts, D. A., Crutcher, R. M., Troland, T. H., 1997, ApJ, 479, 318.
Rudolph, A., Welch, W. J., Palmer, P., Dubrulle, B., 1990, ApJ, 363, 528.
Rydbeck, O. E. H., Irvine, W. M., Hjalmaron, Å., Rydbeck, G., Elldér, J., Kollberg, E., 1980, ApJ, 235, L171.

Sahai, R., Howe, J., 1987, in *Late Stages of Stellar Evolution*. Proceedings of the Workshop held in Calgary, Canada, from June 2-5, 1986, pp. 176. Editors, S. Kwok, S.R. Pottasch.
Sahai, R., Wannier, P. G., 1992, ApJ, 394, 320.
Sanders, D. B., Willner, S. P., 1985, ApJ, 293, L39.
Schloerb, F.P., Snell, R.L, Schwarz, P.R., 1987, ApJ, 319, 426.
Schöier, F. L., Jørgensen, J. K., van Dishoeck, E. F., Blake, G. A., 2002, A&A, 390, 1001.
Schwartz, P. R., Waak, J. A., Smoth, H. A., 1983, ApJ, 267, L109.
Scott, P. F., 1978, MNRAS, 183, 435.
Scoville, N. Z., Sargent, A. I., Sanders, D. B., Claussen, M. J., Masson, C. R., Lo, K. Y., Phillips, T. G., 1986, ApJ, 161, 130.
Schmid-Burgk, J., Muders, D., 1994, ASP Conf. Ser., 57, 74.
Schulz, A., Güsten, R., Zylka, R., Serabyn, E., 1991, A&A, 246, 570.
Sievers, A. W., Mezger, P. G., Gordon, M. A., Kreysa, E., Haslam, C. G. T., Lemke, R., 1991, A&A, 251, 231.
Snell, R. L., Mundy, L. G., Goldsmith, P. F., Evans II, N. J., Erickson, N. R., 1984, ApJ, 276, 625.
Sutton, E. C., Peng, R., Danchi, W. C., Jaminet, P. A., Sandell, G., Russel, A. P. G., ApJS, 97, 455.
Swade, D. A., 1989, ApJ, 345, 828.
Tamura, M., Sato, S., Suzuki, H., Kaifu, N., 1990, ApJ, 350, 728.
Thronson, H. A., Lada, C., Hewagama, T., 1985, ApJ, 297, 662.
Tieftrunk, A., 1993, Diploma Thesis, Uni. Bonn.
Tieftrunk, A., Pineau des Forêts, G., Schilke, P., Walmsley, C. M., 1994, A&A, 289, 579.
Tieftrunk, A., Wilson, T. L., Steppe, H., Gaume, R. A., Johnston, K. J., Claussen, M. J., 1995, A&A, 303, 901.
Tieftrunk, A., Megeath, S. T., Wilson, T. L., Rayner, J. T., 1998a, A&A, 336, 991.
Tieftrunk, A., Gaume, R. A., Wilson, T. L., 1998b, A&A, 340, 232.
Tiemann, E., 1974, J. Phys. Chem. Ref. Data, 3, 259.
Turner, B. E., 1991, ApJS, 76, 617.
Turner, B. E., Chan, K.-W., Green, S., Lubowich, D. A., 1992, ApJ, 399, 114.
Uchida, K. I., 1994, unpublished data.
Uchida, K. I., Fiebig, D., Güsten, R., 2001, A&A, 371, 274.
Ungerechts, H., Walmsley, C. M., Winnewisser, G., 1986, A&A, 157, 207.
Van der Tak, F., Boonman, A. M. S., Braakman, R., van Dishoeck, E. F., 2003, in preparation.
Watt, G. D., Charlney, S. B., 1985, MNRAS, 213, 157.
Watt, G. D., Millar, T. J., White, G. J., Harten, R. H., 1986, A&A, 155, 339.
Weigelt, G., Balega, Y. Y., Preibisch, T., Schertl, D., Smith, M. D., 2002, A&A, 381, 905.
Werner, M. W., Becklin, E. E., Gatley, I., Matthews, K., Neugebauer, G., Wynn-Williams, C. G., 1979, MNRAS, 188, 463.
Wilking, B. A., 1992, *Star formation in the Ophiuchus molecular cloud complex*. In *Low Mass Star Formation in Southern Molecular Clouds*, ed. B. Reipurth, ESO Scientific Rept. No. 11, pp. 159-196.
Wilking, B. A., Lada, C. J., 1983, ApJ, 274, 698.
Wilner, D. J., Welch, W. J., 1994, 427, 898.
Wilson, T. L., Mauersberger, R., 1990, A&A, 239, 305.
Wilson, T. L., Johnston, K. J., Mauersberger, R., 1991, A&A, 251, 220.
Wilson, T. L., Rood, R. T., 1994, ARA&A, 32, 191.

Wilson, T. L., Mehringer, D., M., Dickel, H. R., 1995, A&A, 303, 840.
Winnewisser, M., Sastry, K. V. L. N., Cook, R. L., Gordy, W., 1964, J. Chem. Phys., 41, 1687.
Woody, D. P., Scott, S. L., Scoville, N., Z., Mundy, L. G., Sargent, A. I., Padin, S., Tinney, C. G., Wilson, C. D., 1989, ApJ, 337, L41.
Wootten A., Loren, R., B., 1988, in Symposium on the Physics and Chemistry of Interstellar Molecualr Clouds, ed. G. Winnewisser & J. T. Armstrong (Berlin: Springer), 178.
Wright, M. C. H., Dickel, H. R., Ho, P. T. P., 1984, ApJ, 281, L71.
Wright, M. C. H., Plambeck, R. L., Wilner, D. J., 1996, ApJ, 469, 216.
Wynn-Williams, C. G., Becklin, E. E., Neugebauer, G., 1972, MNRAS, 160, 1.
Zeng, Q., Batrla, W., Wilson, T. L., 1984, A&A, 141, 127.
Zhang, Q., Wootten, A., Ho, P. T. P., 1997, ApJ, 475, 713.
Zhang, Q., Ho, P. T. P., 1997, ApJ, 488, 241.
Zhou, S., Butner, H. M., Evans II, N., J., Güsten, R., Kutner, M. L., Mundy, L. G., 1994, ApJ, 428, 219.

Chapter 3 Zeeman Measurements using SO(1_0-0_1) Transition

3.1 Introduction

The influence of magnetic fields on the evolution of dense cloud cores as potential sites of future star formation is still difficult to evaluate quantitatively. While there are discussions in the theoretical literature about the characteristics of magnetized clouds, the data base in support of this scenario remains quite restricted (Mestel & Spitzer, 1956; Mestel, 1966; Mouschovias, 1987; McKee et al., 1993; Shu et al., 1999; and many others). In order to understand the physics of the relatively late star formation process and verify against existing models, it is necessary to measure the actual magnetic field strength in those dense molecular cloud cores.

The only direct technique to determine the magnetic field strength is via measurement of the Zeeman splitting of atomic or molecular lines. The Zeeman effect is the splitting of spectral lines into multiple components due to the application of an external magnetic field, when the magnetic field removes the degeneracies in atomic or molecular quantum levels. The split lines are circularly and oppositely polarized, whereas the unsplit line is linearly polarized. The electric vectors of split lines will rotate in the plane perpendicular to the magnetic field direction, and the electric vectors of the linearly polarized line will be in the direction of the field. In the general case with arbitrary viewing angle, one will observe elliptical polarization for the split lines.

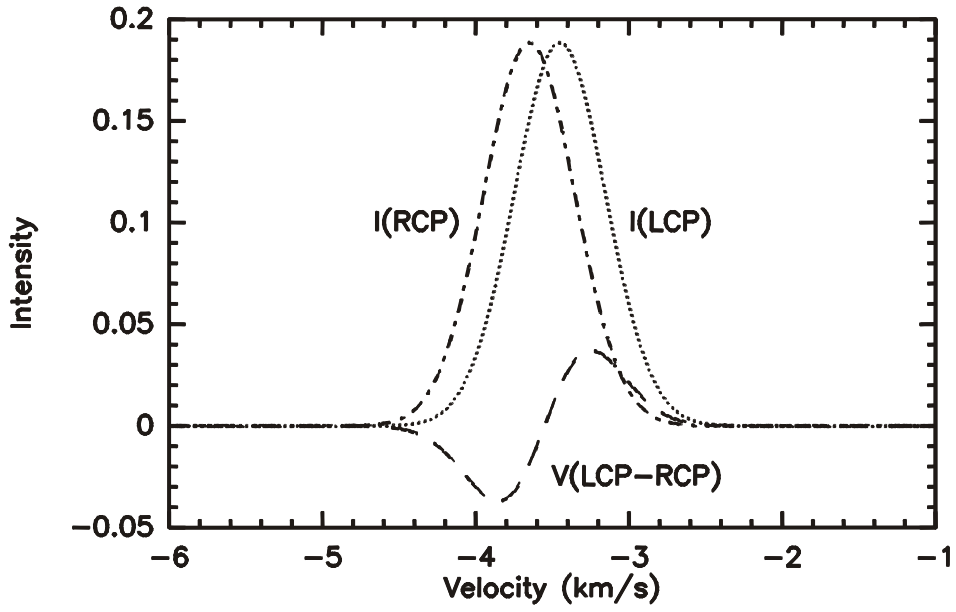

Fig. 3.1. Simulated Gaussian signals without noise to show the Zeeman spectra with splitting between LCP and RCP channels. The long dashed lines shows the resulting V signal.

In practice, the signals can be separated with a polarizer into two independent categories, the right- and left-handed circularly polarized signals (RCP, LCP). If the splitting is large enough, the three Zeeman components (RCP, LCP, linear polarized) are well-separated, the total magnetic field strength can be deduced from the spectra directly. Otherwise, only the line-of-sight component can be obtained by matching the Stokes-V profile (the difference between RCP and LCP signals) with the derivative of Stokes-I signal (the sum of RCP and LCP signals). In

astrophysical Zeeman measurements, the large splitting case where one can deduce the total field is very rare, except for OH masers measurements (Sault et al., 1990; Crutcher, 1999).

Some suitable atoms or molecules for the astrophysical Zeeman measurements are HI, OH, H_2O, CSS, CN, and SO (Brogan & Troland, 2001; Brogan et al., 1999, 2000; Claussen et al., 1997; Güsten et al., 1994; Fiebig & Güsten, 1989; Crutcher et al., 1993; Shinnaga et al., 1999; Levin et al., 2001; Clark et al., 1978; Uchida et al., 2001). Due to the different chemical properties and origin of these molecules, they give us magnetic field strengths from different environments (density, temperature etc.) in molecular clouds. Among them, CCS, CN and SO are thought to be the only radicals having suitable transitions from dense core gas ($n \sim 10^{3\text{-}6}$ cm^{-3}) (see reviews in Heiles et al., 1991; Crutcher, 1999; Fiebig, 1990).

So far, most successful Zeeman measurements are restricted to low to moderate densities. For example, the 21 cm HI line probes regions with a density of $\sim 10^{1\text{-}2}$ cm^{-3}, and the 1665/1667 MHz OH line traces $\sim 10^{3\text{-}4}$ cm^{-3} regions. For dense clouds, where magnetic fields are believed to be stronger, sensitivity in the measurements is reduced due to the typically higher observing frequencies involved. Therefore fewer successful measurements are reported on dense regions. Towards warm massive clouds, from the mm-lines of CN, fields of order 100 μG have been derived (Crutcher et al., 1996, 1999). Former CCS and SO experiments targeted at low mass cold cores (Uchida et al., 2001) have revealed upper limits only (with the exceptional case of the shocked gas layer in W3(OH), Güsten et al., 1994). The results by Uchida et al. (2001) are clearly sensitivity limited, i.e. the physical (g-factor) and technological (amount of observing time) limits are reached. Due to the technical limitation and the small value of the g-factor, not much more can be expected from CCS, though it traces nicely the low temperature cloud cores.

There are new perspectives for SO. In a recent paper Shinnaga & Yamamoto (2000) have revisited the quantum mechenical coupling for this molecule and derived for the 30 GHz SO(1_0-0_1) transition a very favorable g-factor of 0.622, corresponding to a Zeeman splitting of $2\Delta\nu\ B^{-1}$ =1.740 Hz μG^{-1}, this is orders of magnitude higher than what was calculated before (Zeeman splitting $<10^{-3}$, Bel & Loroy, 1989). Then we found an almost forgotten laboratory measurement by Solomon et al. (1968) in the literature. This paper is neither mentioned in Shinnaga & Yamamoto (2000), nor in Bel & Loroy (1989), and excitingly the results from the measurements agree with Shinnaga's calculation very well. This makes sensible Zeeman observations of this transition very attractive.

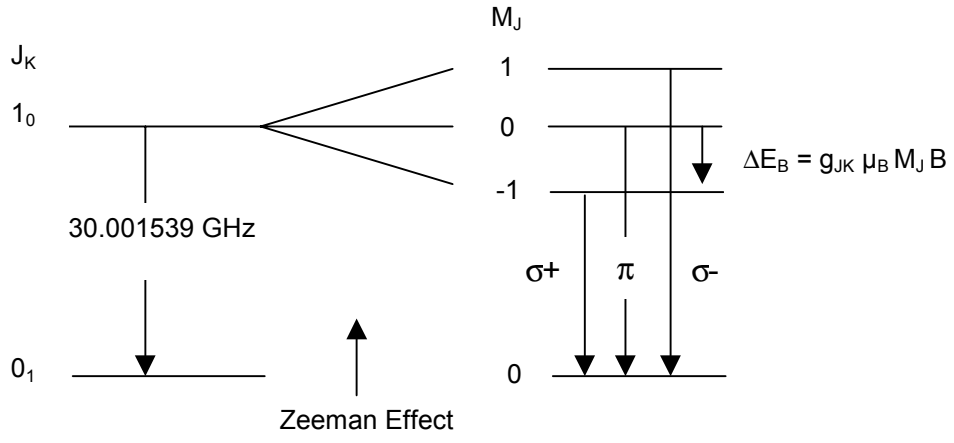

Fig. 3.2. SO term scheme of $J_K = 1_0$-0_1 transition. g_{JK} is the g-factor of the transition, μ_B is the nuclear magneton, M_J is the magnetic quantum number, and B is the magnetic field strength. σ± correspond to circular polarized emission components, and π is the linear polarized component.

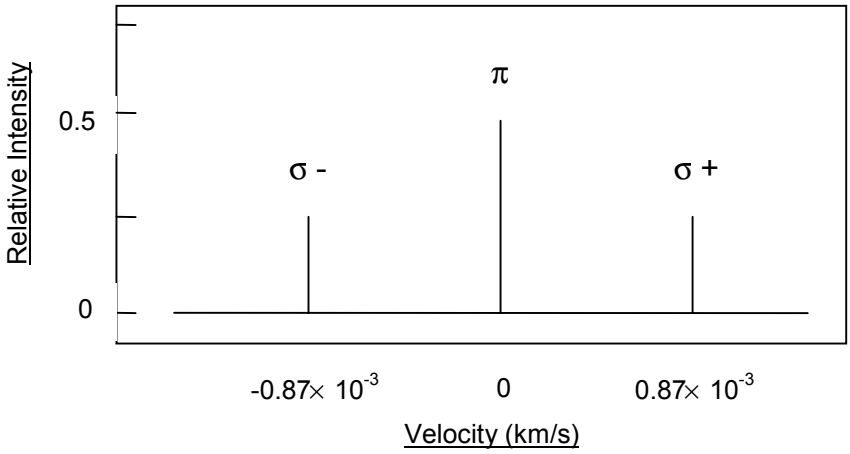

Fig. 3.3. Relative intensity and position of three components in the SO(1_0-0_1) transition for B =100μG. As mentioned above, if the frequency offset is small compared to the linewidth, only the line-of-sight magnetic field, B_{los}, can be deduced. A further calculation based on the new result shows comparable large Zeeman splitting factor A_{mol} = 12.425 km $s^{-1}G^{-1}$ in the equation (Fiebig, 1990),

As mentioned above, if the frequency offset is small compared to the linewidth, only the line-of-sight component of magnetic field, B_{los}, can be deduced. A further calculation based on the new result shows comparable large Zeeman splitting factor A_{mol} = 12.425 km s^{-1} G^{-1} in the equation (Fiebig, 1990),

$$\frac{|T_V|}{T_I} = A_{mol}\frac{B_{los}}{\Delta v}, \tag{3.1}$$

where T_V is the amplitude of the difference spectrum between the RCP and LCP emission, equivalent to the Stokes parameter "V". T_I is the total power amplitude of the two polarized emissions, equivalent to the Stokes parameter "I". Δv is the observed linewidth. From eq(3.1), we see not only large Zeeman splitting factor A is favored in a Zeeman measurement, but also high intensity and narrow linewidth. Table 3.1 presents a comparison of Zeeman characteristics of the SO 1_0-0_1 line with other species tracing dense core gas. In Fig. 3.4 we show the relation of the normalized V profile and the magnetic field strength B for different linewidths.

Table 3.1. Dense region tracers with suitable Zeeman splitting factor. For the CN molecule, the A value listed here is the component with largest g-factor and strongest intensity.

Tool	Transition	Frequency (GHz)	A_{mol} (km s^{-1} G^{-1})	Notes
SO	**$J_K = 1_0$-0_1**	30.0014	12.425	**Ideal tool for dense cores**
SO	$J_K = 2_1$-1_1	13.0440	31.7	
CCS	$J_K = 1_0$-0_1	11.119	15.7	Good tracer for TMC-like cores
CCS	$J_K = 2_1$-1_0	22.344	7.9	Chemically absent otherwise
CN	NJF=$1\frac{3}{2}\frac{3}{2}$-$0\frac{1}{2}\frac{1}{2}$	113.488	4.2	Tracing $n(H_2)$~$10^{5\text{-}6}$ cm^{-3}

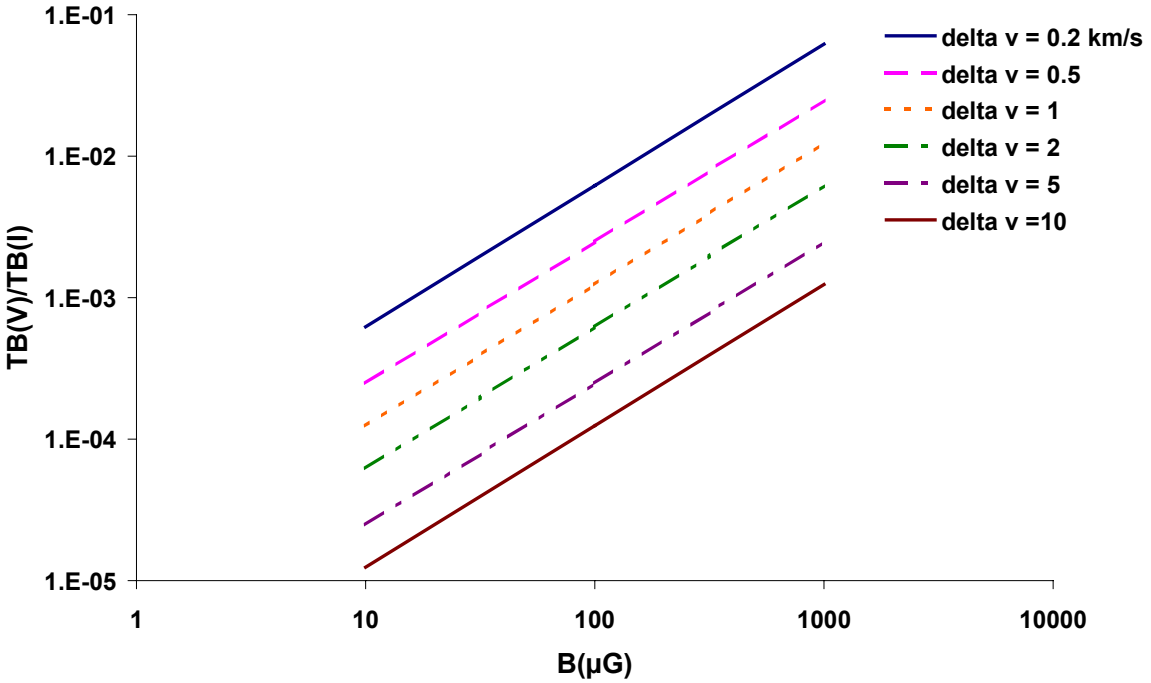

Fig. 3.4. Normalized amplitude of V-spectra $\frac{|T(V)|}{T(I)}$ vs. magnetic field strength B(=B_{los}) for different linewidths.

3.2 New 30GHz Zeeman Receiver

In order to perform Zeeman measurements using the SO 1_0-0_1 line at 30 GHz, the old dual-channel 30GHz receiver with dual-horn feed in Effelsberg (Fig.3.6(a)) was modified and upgrated to a dual circularly polarized (RCP, LCP) receiver by replacing the old horns with a new single-horn feed with polarizer (Fig.3.6(b)). The work was performed in the Microwave Laboratory at the MPIfR from December 2001 to March 2002. The old frontend amplifiers were also replaced by new 4-stage HEMT amplifiers with lower noise temperature. New bandpass filters (29.5-31.8 GHz) were added between polarizer and amplifiers in both channels, therefore the new receiver is working in single-side-band (SSB) mode to get rid of the noise from the other sideband. Some waveguide structure was modified to fit the new feedhorn and polarizer. Otherwise we kept most of the old mechanical stucture and vacuum design unchanged. The polarizer is a custom product for 1cm wavelength. The ellipticity is less than 0.3dB and the isolation is better than 30dB at 30GHz. Under this configuration, one can measure both polarized signals simultaneously.

From the measurements in the Microwave Laboratory, the noise temperature of the new amplifiers (T_{amp}) at 30GHz are 40K/34K for channel A/B with optimal biasing. The performances of the amplifiers are not as good as expected due to the frequency mismatch in the old circuit layout, which was designed for 32 GHz. There was no time to check if the characteristics of the new transistors are similar to the old ones. This mis-match may increase the noise level. In the new receiver, channel A (CH-A) receives the RCP signals and channel B (CH-B) receives the

LCP signals in the lab. In Effelsberg, since the new Zeeman receiver was situated in the prime focus cabin, the wave from the sky experiences one reflection on the main dish, CH-A will receive LCP signals from the sky and CH-B will receive RCP ones.

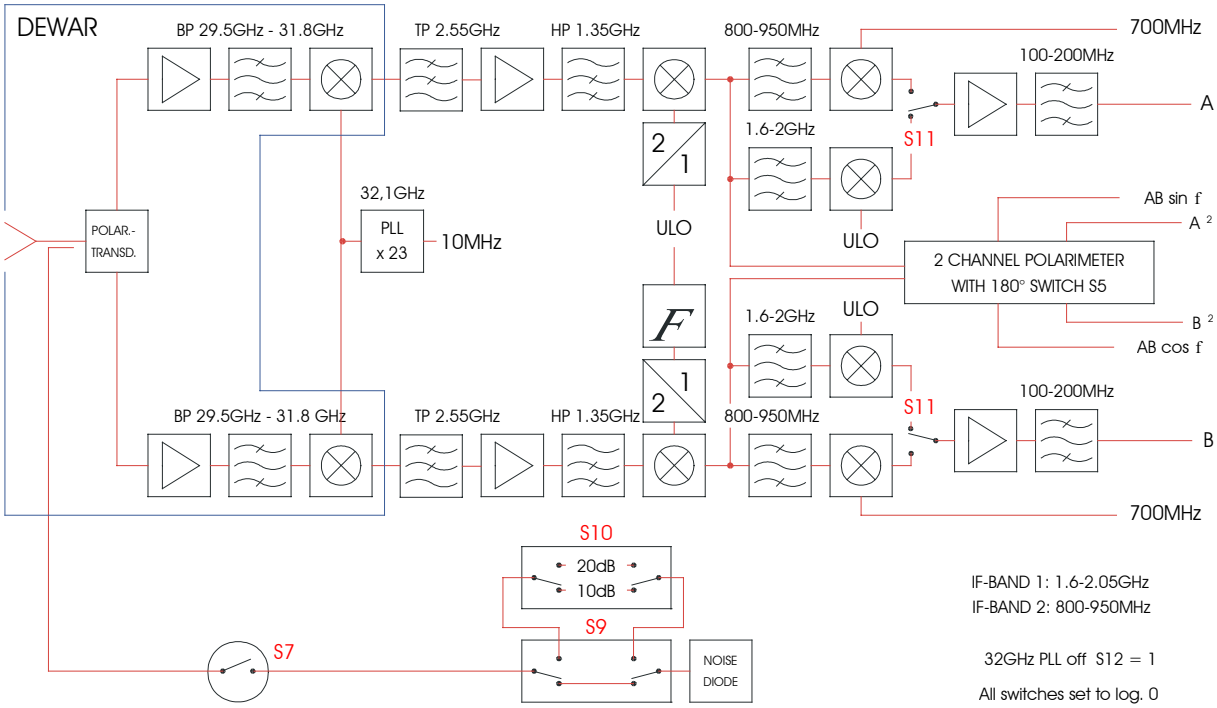

Fig. 3.5. The block diagram of the new Zeeman receiver.

A hot-cold measurement was also performed in the Microwave Laboratory to determine the noise temperature of the receiver (T_{rx}). The scaling factor from counts in the autocorrelator to Kelvin (T_{cal}) of the two channels was also determined. And a long-term measurement of T_{cal} was performed to check the stability of the system. In these measurements, the bandwidth was 100MHz. The performance of channel B is better than that of channel A, but the reason is unclear. Some important parameters are shown in Table 3.2 and 3.4. The noise temperature of the amplifier at channel B is suspicious, because the receiver temperature T_{rx} is lower than T_{amp}!

Table 3.2. Basic characteristics of the new Zeeman receiver for channel A and B, all values are measured at 30GHz with a 100MHz filter.

	CH-A (RCP)	CH-B (LCP)
T_{amp} (K)	40	34
Gains of HEMT amp.(dB)	33.5	32
T_{rx} (K)	55.3	33.2
T_{cal} (K)	12.66	12.6

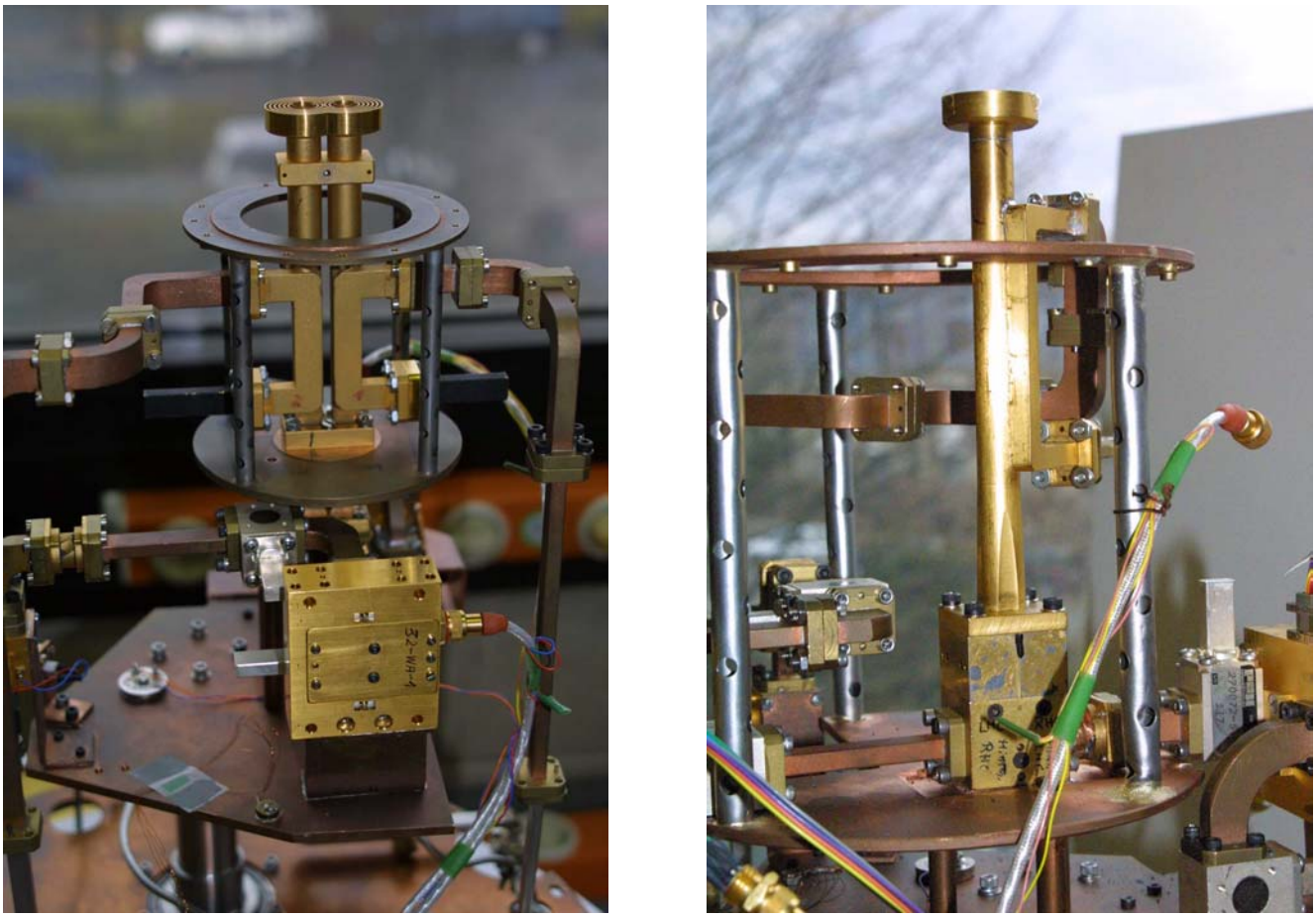

Fig.3.6. Left**: (a)** Dual-horn system in old configuration.
Right**: (b)** New single-horn system with polarizer. The new HEMT amplifiers are not shown in the picture.

3.3 The Performance of the New 30 GHz Receiver in Effelsberg

3.3.1 The System Temperature, Beamwidth

The Effelsberg 100-meter radio telescope is one of the world's largest single-dish telescopes. The large collecting area provides the best chance to perform Zeeman effect measurements in the centimeter range on the earth. The new 30 GHz receiver is a prime focus receiver. The first test of the new receiver at the Effelsberg 100m telescope took place on 19 and 25-27 March 2002. In order to measure the system temperature of the receiver, we observed different sources on the sky with various elevation angles. Here we assume the relation between T_{sys} and Airmass (=1/sin(elevation)) is

$$T_{sys} \cong T(\text{zenith}) + T_{atm} \times (\text{Airmass}-1), \tag{3.2}$$

where T(zenith) is the system noise temperature at zenith (Airmass=1). The weather was excellent during those sessions. The system temperature versus Airmass is plotted in Fig. 3.7 for different days. By regression, the system temperatures at zenith are 101-124 / 79-95 K channel A/B respectively, instead of the expected values of 70/50 K. The system temperature changes with time as shown in Table 3.3.

Based on previous experience at 1cm wavelength, it is unlikely that the telescope and the sky will add another 50 K in both channels if the weather is not extremely bad. If there are no other noise sources in the prime focus cabin, it is hard to explain the increase in noise temperatures in both channels. The illumination pattern of the new feed horn shall be investigated to rule out major spillover and coupling to the ground.

From the continuum mode observation towards 3C84, we compared the FWHP of two receivers in use in Effelsberg at 30 GHz. Both measurements were performed when the elevation angle of the telescope was around 35°. As shown in Table 3.4, the FWHP of the new receiver is broader than the old one. And the beam efficiency is higher by 15 %. This implies the beam patterns of the two receivers are different. This might give us some clues for the illumination pattern and the reason of the high system temperature. We need more measurements to investigate the reasons.

The increased noise temperature factor of 1.6 (from measurements on 25 Mar. 2002) or 1.8 (from 05 Apr. 2002) is very important in the following Zeeman measurements, since the required integration time is proportional to the square of the noise temperature. With such noise temperatures, we need 2.6 or even 3.4 times more time than expected. And this factor makes the time-consuming Zeeman measurements even more difficult.

Table 3.3. System temperature in channel A and B of the new Zeeman receiver.

	Date	CH-A (K)	CH-B (K)
T_{sys} (zenith)	25,03,2002	101	79
T_{sys} (zenith)	05,04,2002	124	95
T_{sys} (zenith)	25,03,2003	107	93

Table 3.4. Comparison of two receivers at 30 GHz in Effelsberg.

	FWHP in Azimuth (arcsec)	FWHP in Elevation (arcsec)	Main Beam Efficiency	Sensitivity (K/Jy in T_a^*)
27-36 GHz single channel Rx	27.66	28.82	0.53	0.85
29.5-31.8 GHz New Zeeman Rx	29.35	30.54	0.61	0.95

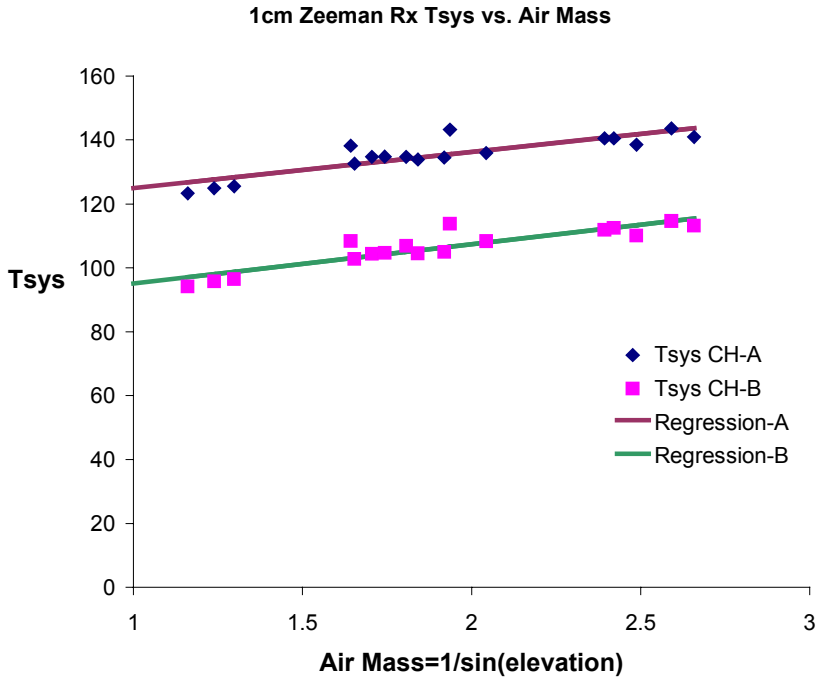

Fig. 3.7. System temperature vs. airmass on 05,04,2002.

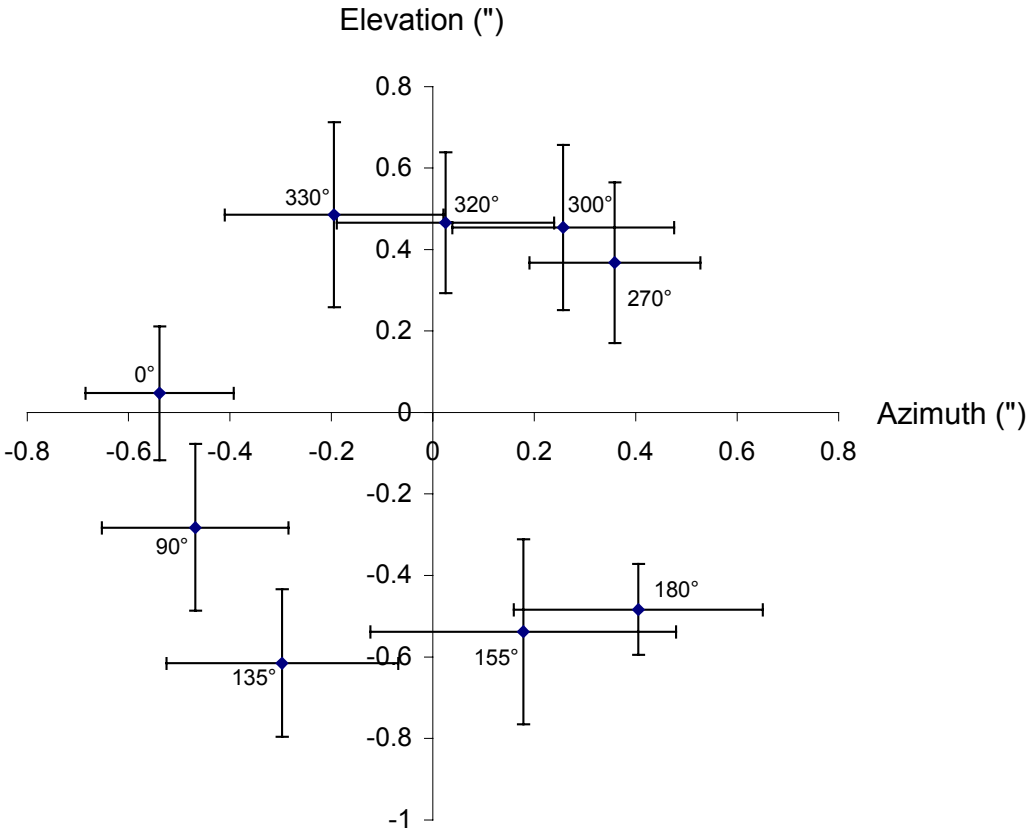

Fig. 3.8. The beam squint effect of the receiver at Effelsberg. The angle by each point is the position angle of the receiver. The best position is 320°. Error bars are also shown.

3.3.2 The Beam Squint Effect

Troland & Heiles (1982) discussed the difficulties encountered in Zeeman measurements using the HI line. Among them, the instrumental effects that come from the different response of two circular polarizations are the most important. The so-called “beam squint effect”, which makes the two polarized beams point towards slightly different positions in the sky (Chu & Turrin, 1973; Adatia & Rudge, 1975; Duan & Rahmat-Samii, 1991; Fiebig et al., 1991; Cwik & Jamnejad, 1997), would produce the same observed effect as Zeeman splitting, if there is a velocity gradient within the source. This effect exists not only in the main beam but also in the sidelobes, so one has to consider this sidelobe effect in HI Zeeman measurements. Since SO emission is weak over most of the sky, the polarized sidelobes of an antenna will not produce significant effects as in HI measurements. Therefore one has to minimize this effect in the main beam before actually performing a Zeeman measurement.

Beam squint occurs when a circularly polarized feed illuminates a reflector system in an asymmetric or offset manner. It occurs in the plane transverse to the plane of asymmetry. Fiebig et al. (1991) reported the beam squint effect for the telescope in Effelsberg with a receiver in the secondary focus cabin. The numerical estimation of the effect is also derived. In this case, one cannot eliminate the effect due to the limitation of the secondary cabin layout. But for a symmetrical reflector system like in Effelsberg with a receiver in the prime focus cabin, in principle one can minimize the effect by rotating, tilting, and shifting the receiver.

We measured the beam squint effect using the continuum pointing source 3C84 in March 2002. By changing the position angle of the receiver in the prime focus cabin (parameter OPOS in the Effelsberg control program), the average of the pointing difference in the two receiver channels are computed by repeated pointing scans. Tilting (SFC3) and shifting (SFC1) the receiver were also tried to minimize the beam squint. However, our measurements show that the squint pattern is almost circular (like for other prime focus receivers), and that we can only minimize the difference between the two channels to 0.47" in elevation direction and 0.03" in azimuth, when the position angle of the receiver (OPOS) is at 320°. The results of beam squint measurements are shown in Fig. 3.8. The offsets between two polarizations are better than 0.8" at all position angles. In another measurement Fiebig (1990) reported the beam squint in Effelsberg is less than 1" with prime focus K-band receiver. Levin et al. (2001) reported 3.6" at DSS-13, the 34 m telescope in Goldstone with 65" beamwidth. It is quite small, but a squint means that one needs double observation time.

Because we can not eliminate the beam squint effect, we have to rotate the receiver during the Zeeman measurements to check if the “detected“ Zeeman pattern comes from real magnetic fields in the source or from a velocity gradient. In the following observations, we chose the position angles of 320° and 155°, which are at the opposite side in the beam squint pattern, to minimize this effect. Since the Effelsberg 100-m telescope has an azimuth-elevation mount, we expect the beam squint effect would smooth out and will average to zero.

3.4 Zeeman Observations on DR21(OH)-RC and Orion B

3.4.1 Observation

The Zeeman observations were performed between April 2002 and March 2003 with the 100-m telescope of the MPIfR (Max-Planck-Institut für Radioastronomie) at Effelsberg. The summer

data suffer from bad weather conditions and high noise temperature. Thus for the data reduction process described in the following, they are excluded. The beam size is ~ 30" at 30 GHz, with main beam efficiency of 0.6. Both RCP and LCP signals were observed simultaneously with the 8192 channel autocorrelator as backend, and the velocity resolution in the spectra is ~ 4.8×10^{-2} km s^{-1}. All the data were carried out in frequency switching mode to gain a factor of two in observation time. The system temperature is reported in §3.3.1. The calibration continuum sources were NGC7027 and 3C120. Pointing was checked every hour with nearby continuum sources. The pointing accuracy was better than 10". All data were reduced using standard procedures in the GILDAS software package (http://www.iram.fr/IRAMFR/GS/ gildas.htm).

From eq.(3.1) we can see that the best candidate sources for Zeeman measurements should have line profiles with high intensity (large T_l) and narrow linewidth (small ΔV). Based on the data in Table 2.2 and the CN results from Crutcher et al. (1999), we chose the DR21(OH)-RC and Orion B regions as first candidate sources for Zeeman measurements. Crutcher et al. (1999) performed Zeeman measurements towards these two sources using the CN radical, which also traces the dense regions. They obtained B_{los} = -450 ± 150 μG (with positive sign away from observer) on DR21(OH)-RC with the 23" beam at the IRAM 30m telescope, but they had no detection on Orion B. However, being a star-forming region, one expects magnetic fields there too.

Table 3.5. The SO(1_0-0_1) line parameters with single gaussian fit from Table 2.1 and expected magnetic field strengths from Crutcher et al. (1999) in the candidate sources.

Source name	R.A. (1950)	Dec (1950)	V_{LSR} (km/s)	ΔV (km/s)	T_a^* (K)	B_{los} (μG)
DR21(OH)-RC	$20^h37^m13^s.0$	+42:12:00	-3.2	2.9	0.78	– 450 ± 150
Orion B	$05^h39^m13^s.5$	-01:57:15	9.9	1.6	1.16	+ 270 ± 330

3.4.2 Data Reduction

The RCP and LCP signals are reduced separately. The Zeeman measurements require high precision in data reduction, therefore any biased step applied in the reduction process would eliminate or generate fake Zeeman S-profiles in the Stokes-V spectrum as shown in Fig.3.1. Besides instrumental effects, the subtraction of a baseline will also affect the results. The situation is even more critical for frequency switched observations, where there is baseline offsets due to the shifted bandpass.

We found that the results differ a lot when different baselines of different orders are subtracted from the spectrum. To avoid this uncertainty, data are reduced with only a single phase at a time. This avoids the high order baselines after folding a frequency switch scan. After the baseline is removed, the spectra are summed up and shifted to the "correct" velocity and intensity.

3.4.3 Least-Squares Fitting of Stokes-V Profile

Once one has obtained the high signal-to-noise ratio RCP and LCP data, the least-squares fitting algorithm described in Sault et al. (1990) is applied to determine the magnetic field strength from the observed data. The Stokes-V spectrum can be written as,

$$T_V(\nu) = \frac{1}{2}\cos\theta\left[T_I(\nu+\delta\nu) - T_I(\nu-\delta\nu)\right], \tag{3.3}$$

where θ is the angle between the magnetic field and the line of sight, δν is the frequency shift between the split and unsplit lines which equals the Zeeman splitting coefficient Δν times magnetic field stregth B.

If the splitting δν is small compared to the line width, the derivative of T_I is a good approximation to the difference term in eq.(3.3), and furthermore it can be approximated by the measured spectrum I, which equals ½ (I_{RCP}+I_{LCP}). Including the leakage term caused by the leakage of linear polarization into circular polarization, and considering the spectra in terms of channels instead of velocity, we can write eq.(3.3) as

$$V = \alpha\frac{dI}{dn} + \beta I, \tag{3.4}$$

where V equals (I_{RCP}+I_{LCP}), n is the channel number in the spectrum, α =δν cosθ, and βI is the leakage term. Applying the least-squares technique, the problem is now to find the best values of α and β which minimize

$$\varepsilon^2 = \sum_i (V_i - \alpha\frac{dI_i}{dn} - \beta I)^2, \tag{3.5}$$

in which i is the index to the total number of channels N in the spectrum.

If the leakage term βI is negligible, Sault et al.(1990) show that the best estimation value α_{est} is

$$\alpha_{est} = \frac{\sum_i V_i \frac{dI_i}{dn}}{\sum_i \left(\frac{dI_i}{dn}\right)^2} \tag{3.6}$$

and for a typical well-sampled line and if the signal-to-noise ratio $\eta = \frac{1}{\sigma}(\frac{dI}{dn})_{rms}$, in the derivative spectrum of I is high, the variance σ_α^2 of α is

$$\sigma_\alpha^2 = \frac{\sigma^2}{\sum_i \left(\frac{dI_i}{dn}\right)^2}. \tag{3.7}$$

in which σ^2 is the variance in I the spectrum. Then, with the Zeeman splitting factor $2\Delta\nu\ B^{-1}$ =1.740 Hz μG^{-1} and the resolution Δf in the spectrum, the corresponding magnetic field strength B_{los} and σ_B are,

$$\frac{B_{los}}{\mu G} = \frac{2\times\alpha_{orion-B}}{1.74}\times(\frac{\Delta f}{MHz})\times 10^6 \tag{3.8}$$

$$\frac{\sigma_B}{\mu G} = \frac{2\times\sqrt{\sigma_\alpha^2}}{1.74}\times(\frac{\Delta f}{MHz})\times 10^6. \tag{3.9}$$

In order to have a reliable result, Sault et al. simulated the fitting procedure by changing the signal-to-noise ratio and resolution in the spectra. Some requirements in the fitted spectra are listed quantitatively by Sault et al. We summarize here only the important conclusions:

(1) To have a good approximation in deriving the derivative of the Stokes-I profile involved in the fitting procedure with numerical differentiation, the FWHM linewidth ΔV should be larger

than 10 channels, and the ratio of the line splitting to the linewidth ΔV should be less than 0.1. They are good sampling and small splitting criterions.

(2) It is the signal-to-noise ratio in the derivative spectrum which is important. Sault et al. defined a quantity η, which is the ratio of the root-mean-square value in the derivative spectrum to σ. To have a reliable result, this quantity should be larger than 10. When the measure is low, the result is biased.

(3) From the numerical simulations, if the signal-to-noise ratio is low, the variance of the least-squares estimate in magnetic field strength seems to be biased low. That is, we can not judge the reliablity of the results from the error estimate directly.

To verify these conclusions we performed numerical simulations by examining the relation between noise level and results. We chose the line profile of Orion B as template here. With this, we hope to find a more reliable way in dealing with Zeeman data.

In all simulation cases, a field strength of -450 μG was inserted into the spectra. We added white noise in each original RCP and LCP spectrum. In each row in Table 3.6 average values of 10 and 100 independent tests are recorded with different noise levels. Each block contains data with 4 different resolutions using the same initial spectra to simulate the effect of data smoothing which can be used to increase the signal-to-noise ratio. The magnitude and error of the field obtained from each test was also recorded to see if the inserted field strengths is within the range. After 10 or 100 repeated tests, we calculated the possibility of successful detection and it is classified into four groups from A the best (75-100%) to D the worst (0-25%). This "confidence index" is shown in the last column in the table.

From the simulation results, we confirm the validity of our least-squares algorithm and verify the conclusion of Sault et al. (1990) above. For conclusion (3) from Sault et al., we tried to improve the error estimate in the algorithm via simulation. In Table 3.6, the error σ_B in column (4) is 1σ level from eq(3.7). But from column (3) of Table 3.6 we also see that, independent of the known error from σ_B, the actual variance in B_{los} is $2\sigma_B$. This error is independent of noise level and repeat number N. From the experience of the simulation, we found the sum of the two error sources reflecting the true error estimate. To be at the safe side, we will take the total variance $3\sigma_B$ instead of $1\sigma_B$ for the error estimate in the following. We also find that for all the cases with confident index better than 50%, $\eta_{cri} \geq \eta$ If these conditions are matched, we believe that the results from the fitting procedure are reliable and correct.

Table 3.6(a). Simulation results of Orion B with different noise levels with N = 10 tests.

B = -450 μG	**noise 0.01**					
ΔV (channels)	**σ (10^{-3}K)**	**B_{los} (μG)**	**σ_B (μG)**	**η**	**η_{cri}**	
35	6.7 ± 0.8	-656 ± 121	99 ± 12	4.5 ± 0.6	8.8 ± 1.7	D
18	4.8 ± 0.5	-296 ± 160	105 ± 11	11.8 ± 1.3	103 ± 183	D
12	3.7 ± 0.8	-473 ± 202	102 ± 22	23.2 ± 5	44.3 ± 18.6	D
9	3.1 ± 0.7	-504 ± 245	102 ± 24	35.5 ± 7.7	196 ± 432	D

B = -450 μG	**noise 0.008**					
ΔV (channels)	**σ (10^{-3}K)**	**B_{los} (μG)**	**σ_B (μG)**	**η**	**η_{cri}**	
35	5.6 ± 0.5	-389 ± 183	83 ± 8	5.3 ± 0.5	22.2 ± 22.9	D
18	3.9 ± 0.5	-472 ± 185	85 ± 11	14.8 ± 1.9	29.7 ± 14	C
12	3.1 ± 0.6	-410 ± 205	86 ± 15	27.2 ± 4.4	84.1 ± 123	C
9	2.4 ± 0.6	-467 ± 129	78 ± 20	49.2 ± 20.9	60.9 ± 31.7	C

B = -450 μG	**noise 0.005**					
ΔV (channels)	**σ (10^{-3}K)**	**B_{los} (μG)**	**σ_B (μG)**	**η**	**η_{cri}**	
35	3.2 ± 0.3	-488 ± 139	49 ± 5	9.0 ± 0.9	13 ± 5.2	C
18	2.4 ± 0.3	-413 ± 123	53 ± 6	23.7 ± 2.6	30.7 ± 10.5	B
12	1.9 ± 0.5	-467 ± 92	51 ± 13	46.8 ± 10.9	39.1 ± 8.2	B
9	1.5 ± 0.2	-484 ± 120	47 ± 8	75.1 ± 11.6	54.3 ± 14.6	B

B = -450 μG	**noise 0.004**					
ΔV (channels)	**σ (10^{-3}K)**	**B_{los} (μG)**	**σ_B (μG)**	**η**	**η_{cri}**	
35	2.8 ± 0.3	-419 ± 91	44 ± 5	10.2 ± 1.1	14.1 ± 2.8	B
18	2.0 ± 0.3	-446 ± 84	43 ± 7	29.7 ± 4.9	27.0 ± 5.7	B
12	1.5 ± 0.3	-475 ± 110	38 ± 8	63 ± 15.1	39.5 ± 11.3	B
9	1.3 ± 0.3	-485 ± 87	44 ± 10	83 ± 20	52.6 ± 10.1	B

B = -450 μG	**noise 0.0025**					
ΔV (channels)	**σ (10^{-3}K)**	**B_{los} (μG)**	**σ_B (μG)**	**η**	**η_{cri}**	
35	1.7 ± 0.2	-441 ± 57	27 ± 4	16.5 ± 2.2	13.1 ± 1.8	A
18	1.2 ± 0.3	-471 ± 48	25 ± 6	51.4 ± 5.5	24.9 ± 2.4	A
12	1.0 ± 0.2	-436 ± 53	27 ± 7	89.8 ± 24	40.8 ± 5	A
9	0.9 ± 0.2	-458 ± 78	28 ± 6	131 ± 33	55.5 ± 10.8	A

Table 3.6(b). Simulation results of Orion B with different noise levels with N = 100 tests.

B = -450 μG	**noise 0.01**					
ΔV (channels)	**σ (10^{-3}K)**	**B_{los} (μG)**	**σ_B (μG)**	**η**	**η_{cri}**	
35	6.9 ± 0.8	-450 ± 220	103 ± 12	4.3 ± 0.5	38.9 ± 132	D
18	4.8 ± 0.8	-480 ± 211	105 ± 18	12.0 ± 2.2	36.9 ± 44	D
12	3.7 ± 0.9	-490 ± 250	102 ± 24	23.6 ± 5.9	66.4 ± 153	D
9	3.1 ± 0.8	-448 ± 241	101 ± 27	37.1 ± 12	82 ± 89	D

B = -450 μG	**noise 0.008**					
ΔV (channels)	**σ (10^{-3}K)**	**B_{los} (μG)**	**σ_B (μG)**	**η**	**η_{cri}**	
35	5.6 ± 0.6	-421 ± 170	84 ± 9	5.2 ± 0.6	17.4 ± 14.4	D
18	3.8 ± 0.6	-437 ± 182	83 ± 13	15.3 ± 2.5	30.6 ± 20	D
12	3.1 ± 0.6	-452 ± 191	84 ± 16	28.3 ± 6.0	75.4 ± 255	D
9	2.5 ± 0.5	-475 ± 212	81 ± 18	45.2 ± 10.7	67.8 ± 56.5	C

B = -450 μG	**noise 0.005**					
ΔV (channels)	**σ (10^{-3}K)**	**B_{los} (μG)**	**σ_B (μG)**	**η**	**η_{cri}**	
35	3.4 ± 0.4	-441 ± 118	51 ± 7	8.6 ± 1.1	14 ± 5.3	C
18	2.4 ± 0.5	-445 ± 119	52 ± 10	24.9 ± 6.1	28.8 ± 11.7	C
12	1.9 ± 0.4	-480 ± 107	53 ± 11	44.6 ± 11.1	38.5 ± 9.3	B
9	1.6 ± 0.4	-472 ± 115	51 ± 12	71.9 ± 18.7	56.3 ± 18.8	C

B = -450 μG	**noise 0.004**					
ΔV (channels)	**σ (10^{-3}K)**	**B_{los} (μG)**	**σ_B (μG)**	**η**	**η_{cri}**	
35	2.8 ± 0.4	-446 ± 92	43 ± 5	10.3 ± 1.3	13.3 ± 3.1	B
18	2.0 ± 0.4	-444 ± 102	44 ± 8	28.9 ± 5.7	27.7 ± 7.2	B
12	1.6 ± 0.3	-456 ± 98	44 ± 9	54 ± 11.5	40.6 ±10.7	B
9	1.3 ± 0.3	-491 ± 88	43 ± 10	86 ± 21	51.8 ± 9.7	B

B = -450 μG	**noise 0.0025**					
ΔV (channels)	**σ (10^{-3}K)**	**B_{los} (μG)**	**σ_B (μG)**	**η**	**η_{cri}**	
35	1.7 ± 0.2	-441 ± 57	27 ± 4	16.5 ± 2.2	13.1 ± 1.8	A
18	1.3 ± 0.2	-468 ± 62	29 ± 4	43.6 ± 6.9	25.3 ± 3.6	A
12	1.0 ± 0.2	-466 ± 56	28 ± 6	83.3 ± 19	38.2 ± 4.8	A
9	0.8 ± 0.2	-470 ± 60	27 ± 6	134 ± 32	53 ± 7	A

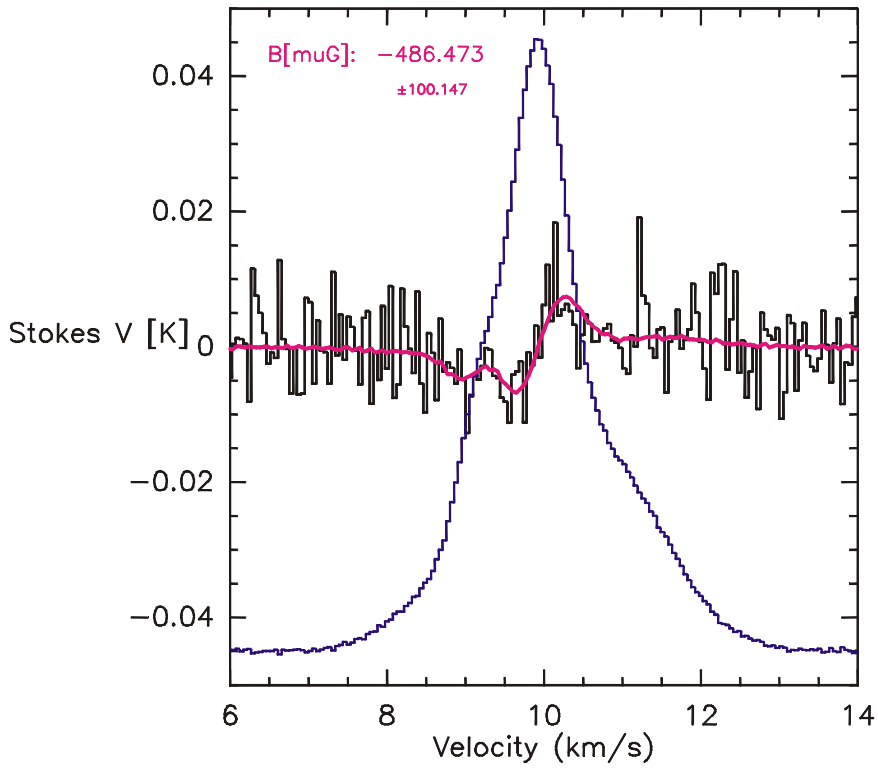

Fig. 3.9(a). An example from the simulation with noise level 0.004 K in RCP and LCP spectra using Orion B spectrum as template. The two spectra in the middle are the Stokes-V spectrum (black) and the best fitting result from least-squares algorithm (pink). The Stokes-I spectrum is also shown for reference (blue). The error shown here is 3σ.

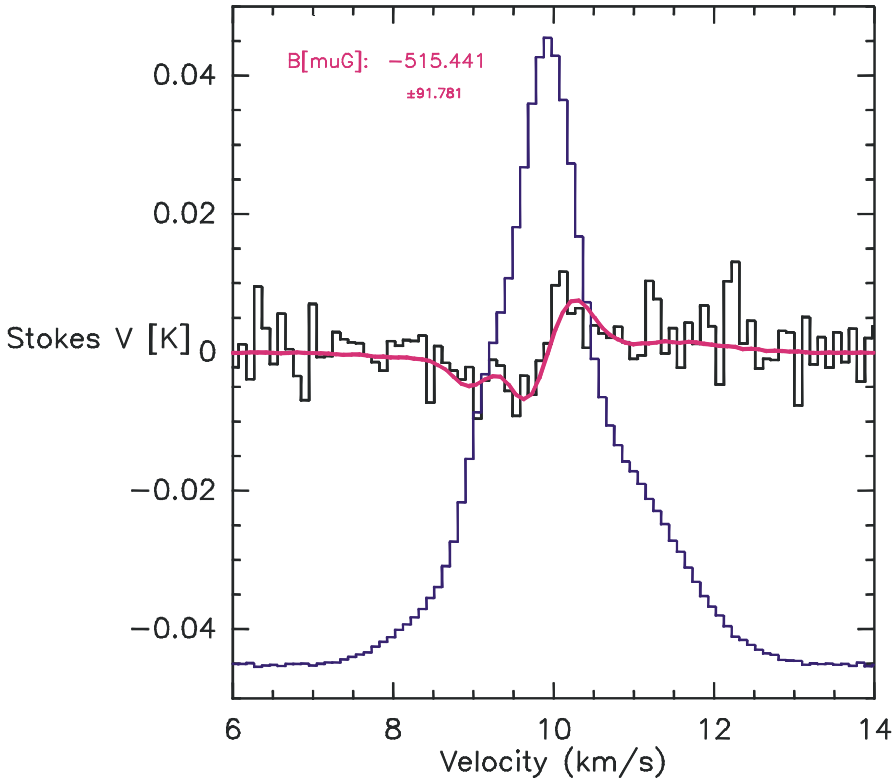

Fig. 3.9(b). The identical data set as in fig.3.9(a), but smoothed into half resolution to get better signal-to-noise ratio. The error estimate does not decrease as signal-to-noise ratio goes up.

Smoothing the spectrum into lower resolution is commonly used to enhance the signal-to-noise ratio in data reduction. Although it can reduce the noise level in the spectrum, but it cannot reduce the error in the results. We can see this point in eq.(3.7), $\sum_i \left(\frac{dI_i}{dn}\right)^2$ will decrease with the same order as σ^2 after smoothing the spectrum. Though the quantity η increases, η_{cri} also increases. Thus smoothing the spectrum can help us to detect the magnetic field only in cases where η and η_{cri} are already comparable. Furthermore it is possible that smoothing the spectrum may also smooth out the Zeeman S-profile feature in the Stokes-V spectrum. Therefore smoothing the spectra or observing with lower resolution cannot improve the error estimate, nor can it help us to detect the magnetic field with less integration time. From the simulation and experience, the linewidth $\Delta V \approx$ 20 to 40 channels is the best resolution for Zeeman measurement, depending on the complexity of the line profile.

In Table 3.6, we can see the first case with the confidence index better than 50% is the noise = 0.004 K case (Fig.3.9(a) and (b)). With the aid of simulation, one can estimate the total integrating time in a more reliable way.

3.4.4 The Results

With the least-squares algorithm and simulations we have established a reliable procedure to analyse the observational data. The total integration time on the source, the line-of-sight magnetic field strengths and 3σ errors are listed in Table 3.7. In DR21(OH)-RC, the magnetic field is detected in only one velocity component, whereas we failed to detect magnetic field towards Orion B. The results according to different receiver position (OPOS) angle, rising and setting source are also shown to examine the beam squint and other instrumental effects.

Table 3.7. Preliminary results from least-squares fits. In the case of DR21(OH)-RC, all the magnetic field strengths derived here are fitted to the – 3.45 km/s component from Table 3.8.

(a)DR21(OH)-RC

	Time (hr)	σ (10^{-3}K)	B_{los} (mG)	$3\sigma_B$ (mG)	η	η_{cri}
Total	45.5	3.9	-2.1	1.2	1.2	1.8
OPOS = 320°	26.7	8.1	-2.0	3.9	0.3	1.8
OPOS = 155°	18.8	5.0	-2.8	2.4	0.6	1.1
Rising	26.9	6.4	-1.7	4.3	0.3	2.1
Setting	18.6	8.0	-3.2	1.4	0.6	2.4

(b)Orion B

	Time (hr)	σ (10^{-3}K)	B_{los} (μG)	$3\sigma_B$ (μG)	η	η_{cri}
Total	31.6	3.5	-155	192	7	35
OPOS = 320°	14.3	4.0	-512	258	15	23
OPOS = 155°	17.3	5.8	108	282	5	48
Rising	12.4	5.7	44	270	6	125
Setting	19.2	6.3	-247	312	5	23

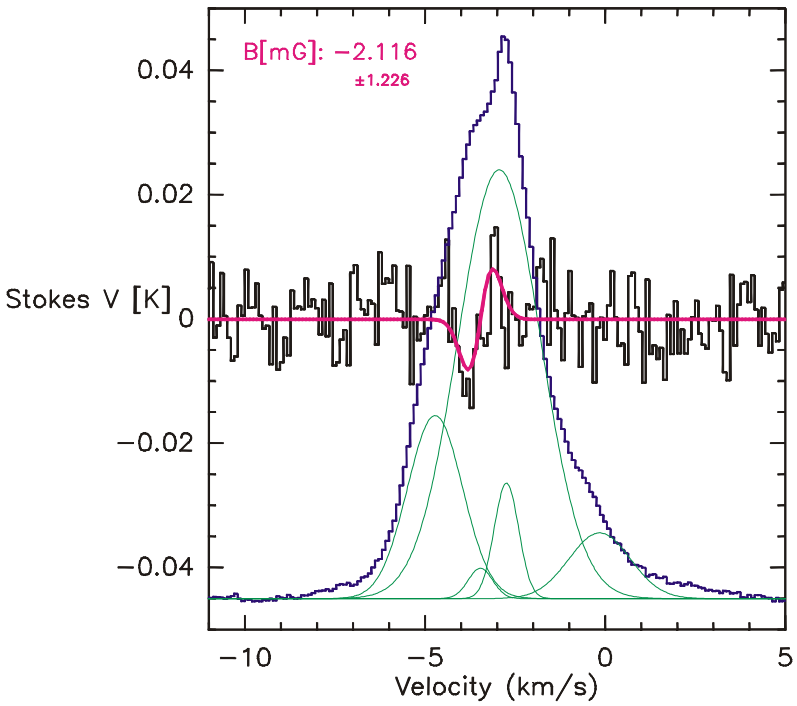

Fig. 3.10(a). The results of DR21OH-RC with total integration time. The Stokes-I spectrum is decomposed into five velocity components (green). The other spectra are as shown in Fig. 3.9.

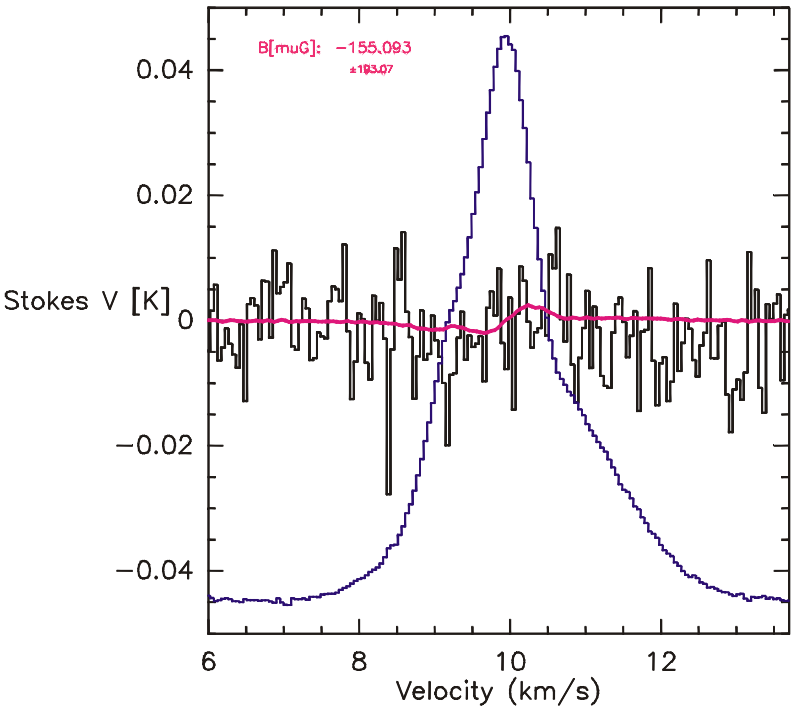

Fig. 3.10(b). The results of Orion B with total integration time. No Zeeman effect is detected in this case.

(1) DR21(OH)-RC

After data reduction with the procedure described in §3.4.2, we observed a clear Zeeman S-curve in the Stokes-V profile (Fig.3.10(a)). The narrow Zeeman profile in the Stokes-V spectrum forced us to fit the Stokes-I profile with a –3.45 km/s velocity component with narrow line width. We therefore tried to decompose the Stokes-I profile of DR21(OH)-RC into five velocity components with the aid of optically-thin ^{34}SO, $C^{18}O$ and $C^{34}S$ data (Padin et al. 1989; Wilson & Mauersberger, 1990; Padin et al., 1989; Chandler et al., 1993). The line parameters are listed in Table 3.8. With these five line parameters we can fit a magnetic field strength of -2.1 ± 1.2 mG. Within the errors, this result holds for the data with OPOS = 320° and OPOS = 155° taken separately.

To check for a fake Zeeman effect from the beam squint effect towards DR21(OH)-RC (§3.3.2), we mapped the surrounding area in a 3×3 grid with quarter beamwidth spacing (~ 7.5 arcsec) to measure the velocity structure. Then we derived the velocity gradient using the same technique as for the Zeeman measurements. However in this case we attribute the difference in two channels to the velocity and intensity gradients. From the artificial Stokes-V profile produced in this fashion we can estimate the maximum velocity gradient to be 3.2 m/s in 0.6 arcsec, which is the beam squint distance from Fig. 3.8, if the whole line shifts. This gradient is from the northeast to the southwest of the source. On the other hand, if all the magnetic field strength we detected in Fig. 3.10(a) comes from the velocity gradient, it corresponds to a velocity gradient of 8 m/s over 0.6 arcsec. Hence the instrumental effect is smaller. But if we compared the results from the two receiver position angles (OPOS= 320° and 155°) and different position angle of the source (rising and setting), we see the beam squint effect exists, but it is not large.

However, with the information above we still cannot exclude the possibility that the narrow component at –3.45 km/s shifts rapidly within the beam squint distance of 0.6 arcsec and produces the S-curve we see in the spectrum. In the estimate of the velocity gradient we have assumed the whole line profile shifting over the range, and we also know there are several independent velocity components in the spectrum. The weak component at –3.45 km/s might have large velocity or intensity gradients at the center position and might thus produce the fake S-curve in the Zeeman measurements. The contribution of this part is too week to be detected in the large scale estimation of the velocity gradient. We cannot exclude any possible scenario before investigating thoroughly the velocity/intensity structure.

If this is not the case, we can say that the results derived in Table 3.7 and 3.8 is coming from real Zeeman effect. With this velocity gradient estimate, we can derive that the maximum uncertainty from the instrumental effect is ~ 40%. In fact, we expect only half of this value due to the azimuth-elevation mount at Effelsberg 100-m telescope, because the source changed its position angles when observing. The direction with the steepest gradient in velocity did not always align with the beam squint direction. At the end we concluded that the magnetic field strengths of the line-of-sight component (B_{los}) is -2.1mG towards DR21(OH)-RC, with ± 0.4 to 0.8 mG uncertainty from beam squint effect, and ± 1.2 mG (3σ) uncertainty from the noise.

Table 3.8. The results from Zeeman measurments of DR21(OH)-RC with five velocity components.

	line 1	line 2	line 3	line 4	line 5
V_{lsr} (km/s)	-4.67	-3.45	-2.90	-2.73	0.0
ΔV (km/s)	1.8	0.8	2.9	0.8	2.0
Intensity (K) (in T_a^* scale)	0.31	0.05	0.78	0.2	0.11
B_{los} (mG)	-	-2.1 ± 1.2	-	-	

(2) Orion B

No Zeeman feature is found in Orion B data after 30 hours integration (Fig. 3.10(b)). The best fitting result is B_{los} = -155 ± 192 μG. And only the upper limit (< 350μG) can be derived. Comparing the results from different receiver position angle (OPOS), and different viewing angle (when the source is rising or setting), it seems that the beam squint effect dominates the results. More integration time is required in this case. Together with results from Crutcher et al. (1999), we can conclude that the magnetic field strength in the line-of-sight towards this region is very low.

3.4.5 Discussion

Since the Zeeman effect is only marginally detected towards DR21(OH)-RC, we concentrate our discussion on that region.

The center position of our measurement is ~ 20" southeast of the peak position in the continuum emission in order to match the best line intensity to linewidth ratio in this area. From the high resolution interferometer map, two compact cores MM1 and MM2 (Woody et al., 1989) can be resolved at the prominent position. The $C^{18}O$(2-1) measurements by Padin et al. (1989) shows that these two cores have velocities of –4.6 and –1 km/s, respectively. MM1 is not included directly in our measurements. The $C^{18}O$(2-1) emission is strong only at the edge of the beam near MM2, and then fades out away from the dense cores. The spatial distribution of mm continuum and $C^{18}O$(2-1) emission is consistent with the the picture desribed in §3.4.4 that the direction of the maximum velocity and/or intensity gradient is from NE to the SW within our 30" beam.

As shown in Table 3.8 the intensity of the velocity component which we detected the Zeeman effect is low. Thus the corresponding magnitute of the magnetic field strength is high. Though we have already rough estimations for the density and temperature in chapter 2, these parameters can apply to the three intense components with V_{LSR} = -4.7, -2.9 and 0.0 km/s without any question. The -4.7 km/s and 0.0 km/s components should be related to the known dense cores DR21(OH)MM1 and DR21(OH)MM2, respectively. The other three components in the center are found only with CS and SO lines. About the densities, mass, temperature and sources sizes, it is still poorly known. From the figure in the review by Crutcher (1999), where he compiled 15 detections of Zeeman measurements in molecular clouds (Fig.3.11), this strong field strength is expected existing in very dense region (the position of the star in Fig. 3.11, above 10^6 cm^{-3}).

The CN radical is the only molecule with successful Zeeman measurement towards the region. Crutcher et al. (1999) found the magnetic field strength of -450 ± 150 μG at the same position as us with a similar beamwidth (Fig. 3.14). They detected two velocity components at V_{LSR} = -4.66 and -0.96 km/s. These velocities are similar to the ones seen towards MM1 and

MM2 by Padin et al. (1989). Though MM1 is not in their beam, from the CN line profiles Crutcher et al. suggested that some of the cloud related to MM1 is still included in the spectrum due to the agreement of the velocity.

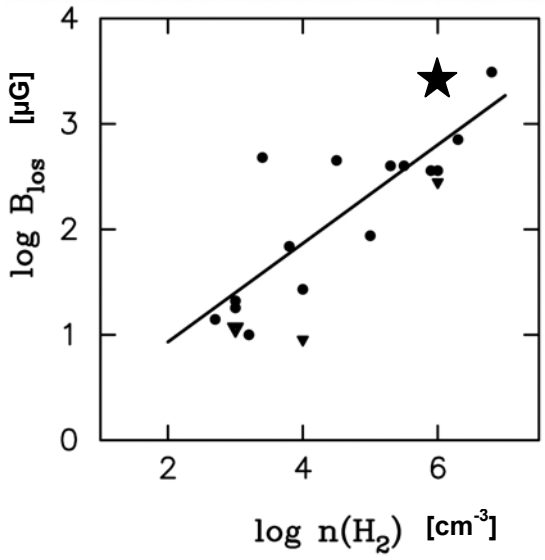

Fig. 3.11. Line-of-sight magnetic field strength vs. cloud density from Crutcher (1999). The straight line is the best fit for the power law between magnetic field strength and gas density, $|B| \propto \rho^{\kappa}$, here $\kappa = 0.47 \pm 0.08$. The possible position of our results towards DR21(OH)-RC is marked by a star.

Comparing the CN spectrum in Crutcher et al. (1999) with the $C^{32}S$(2-1) data by Chandler et al. (1993), at the first glance, it seems that the CN transition in Crutcher's observation might be optically thick and shows a self-absorption feature. But based upon the hyperfine line intensity ratios and the $C^{18}O$ data by Padin et al. (1989), Crutcher concluded that the opacity of CN emission is small or moderate. On the other hand, Chandler et al. (1993) compared their self-absorbed CS line data with ammonia and $C^{18}O$ data, and pointed out that towards this region many molecular lines including ammonia and $C^{32}S$ lines are optically thick. $C^{18}O$ may also possibly be optically thick (Mangum et al., 1992; Chandler et al., 1993). Therefore we cannot exclude the possibility that the high resolution $C^{18}O$(2-1) data from Padin et al. (1989) referred by Crutcher is also optically-thick at the prominent region. From comparison of different line profiles, we think SO (maybe together with CS) and CN (maybe together with CO) may trace totally different parts of the clouds towards this complicated region. Thus one cannot compare the results from SO and CN directly, or use the physical parameters derived from $C^{18}O$ by Padin et al. in our discussion.

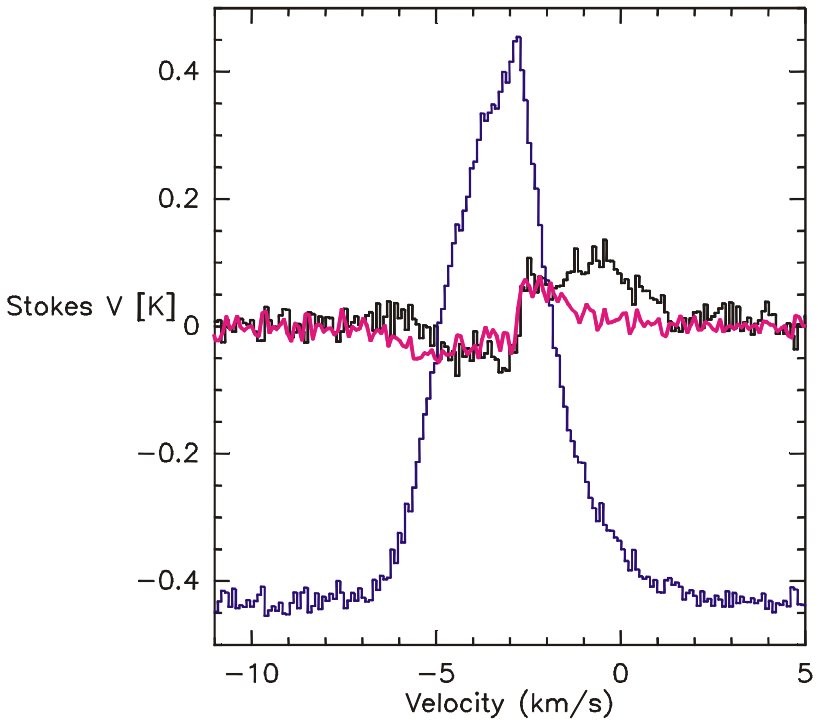

Fig. 3.12(a). The final spectra in the calculation of the velocity gradient in the NE-SW direction towards DR21(OH). Here we compared the two spectra at the north-east and south-west edge in the 3 × 3 grid around the central position spacing in quarter beamwidth. The distance of the two spectra is $15\sqrt{2}$ arcsec. From this figure, we derived the velocity gradient of -3.2 ±0.4 m/s over 0.6" from NE to SW. This is also the steepest direction in velocity gradient.

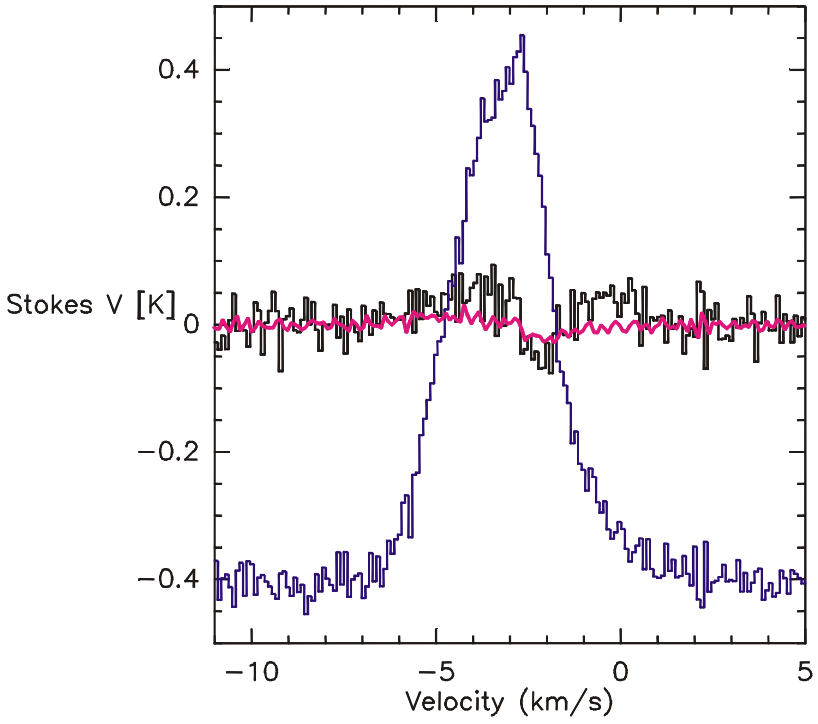

Fig. 3.12(b). As in Fig. 3.12(a) but with the NW-SE direction. Two spectra are at the north-west and south-east edge in the 3 × 3 grid. The distance of the two point is also $15\sqrt{2}$ arcsec. The velocity gradient of +1.5 ±0.5 m/s (3σerror) over 0.6" is derived from NW to SE. In this direction the velocity gradient is smoother.

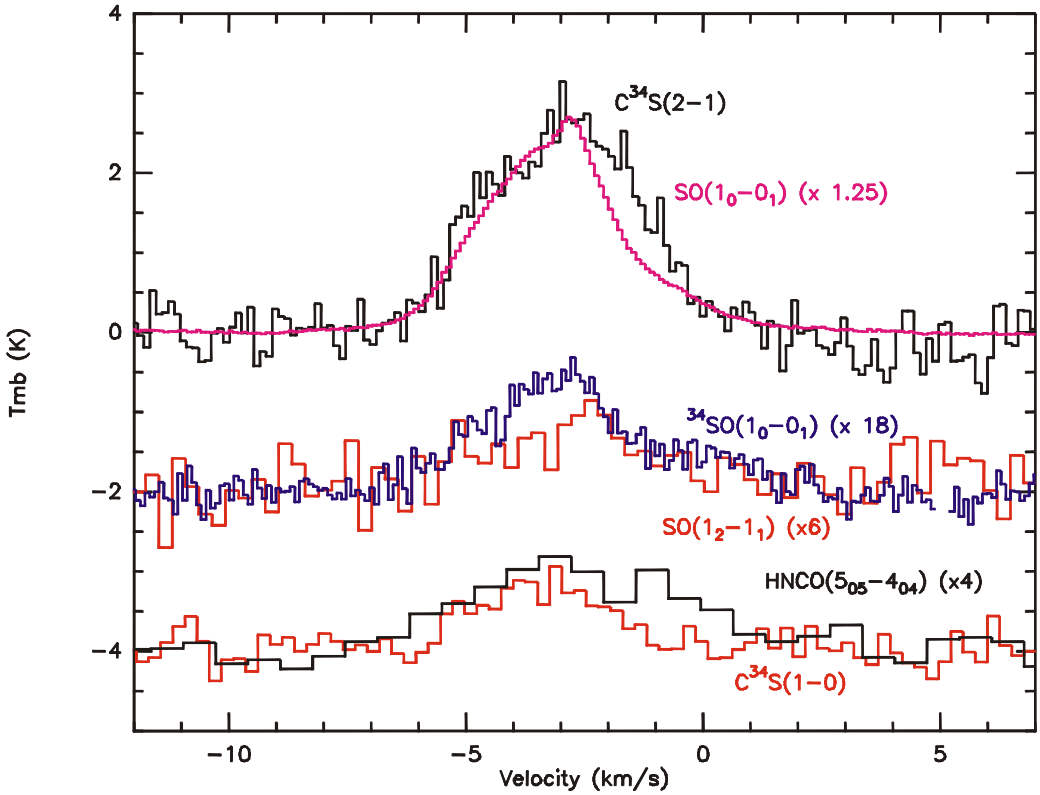

Fig. 3.13. Comparison of line profiles of SO(1_0-0_1) and other transitions towards the DR21(OH)-RC region.

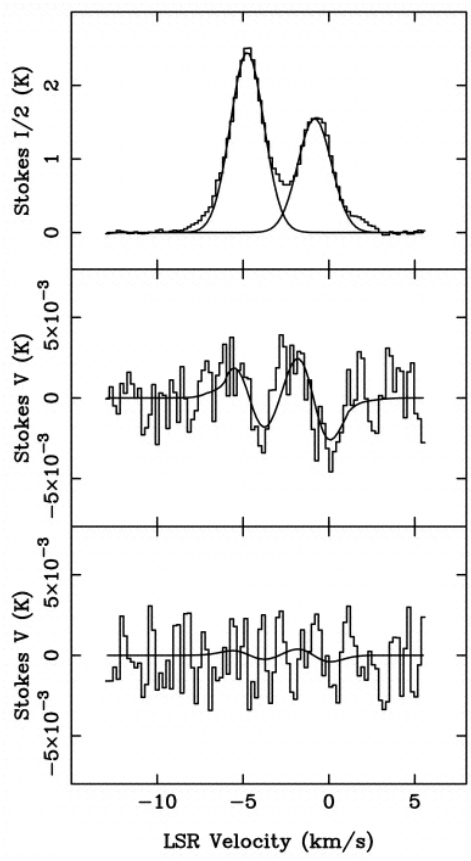

Fig. 3.14. CN Zeeman measurement result towards DR21(OH)-RC from Fig.1 in Crutcher et al. (1999). The top shows the CN Stokes-I spectrum and Gaussian decompositions. The middle shows the Stokes-V spectrum of sensetive hyperfine lines and the best fits of corresponding velocity components. The lower shows the Stokes-V spectrum of non-sensitive hyperfine lines.

In view of this, we tried to obtain useful information from CS data. As mentioned in §2.4, the spatial distribution of SO 30 GHz line is often similar to that of CS. The SO and CS spectra are shown in Fig. 3.13. The line profile of the $C^{34}S$(2-1) transition is very similar to our SO(1_0-0_1) transition. Chandler et al. (1993) observed this region in CS and $C^{34}S$ and found self-absorption features in optically-thick CS(2-1) and CS(1-0) transitions, whereas in their isotopic $C^{34}S$ transitions, they did not find such features and the center velocity of optically-thin isotopic lines was at the center of the optically-thick lines. In our measurements, by comparing the isotopic line intensities and profiles in Fig.3.13 towards the DR21(OH)-RC region, the opacity of SO(1_0-0_1) emission is also small (Table 2.1(b)). The estimate of optical depth from an LVG program also confirms this suggestion. Due to the complexity of the region, Chandler et al. (1993) cannot conclude if it shows the hints of collapsing cloud. However, they fitted the data successfully by a two-component LTE model with a warm (T_{ex}~ 20 K) background layer and cooler (T_{ex}~ 5 K) absorbing foreground gas. They suggest further that the region is in virial equilibrium on large scales. The magnetic field strength needed against collapse is a few hundred μG. The optically thin transitions of SO(1_2-1_1) (Uchida, 1994), HNCO (Zinchenko et al., 2000) and $C^{34}S$(1-0) are also shown in Fig. 3.13 for comparison.

Chandler et al. informed us about the spatial distribution of CS calculated by their two-component model. The peak position is southeast of the peak position in the mm continuum and CO maps. The rotational temperature of CS at our center position is ~17 K, which is close to the rotational temperature of SO derived in Table 2.4. Assuming the abundance of CS is 5×10^{-9} (Irvine et al., 1987), the column density of molecular hydrogen at our center position is ~ 1.5×10^{23} cm^{-2}, which is very high. But because of the low velocity resolution in the CS data, with the information it is still difficult to identify the density and the size related to the –3.45 km/s component and support the suggestion that we have measured the magnetic field in dense core.

From Fig. 3.10(a), we can see that the position of the Zeeman S-curve is close to the position where Stokes-I profile shows a rapid change in slope. It is possible that we just detected the rapid change at the velocity between the distance of 0.6 arcsec. Or this is a slightly self-absorbed feature, thus we decomposed the line profile in the wrong way and then cannot find the correct velocity component related to the Zeeman effect we detected. It is probably not the case because at the same velocity there is also a rapid change in slope in the ^{34}SO spectrum (Fig. 3.13). We need interferometer to investigate the velocity structure in high resolution.

3.5 Future work

Since the physical parameters of the clouds in wjich we detected Zeeman effect are uncertain, we cannot follow the discussion in Crutcher (1999) to investigate the role of magnetic field plays in the cloud and verify the existing star-forming theories. To have a clear view on the effect of beam squint and velocity structure in the region, high resolution interferometer maps of SO or CS emissions are needed. EVLA is the only interferometer that can perform high resolution SO 30 GHz measurements in the future. The noise source in the new 1-cm Zeeman receiver should be investigated at Effelsberg to improve the sensibility of the system. Then with the experience from our work, it is also worth to apply the state-of-the-art in the instrumentation technique to set up a maser type receiver at Effelsberg. Using the maser type receiver, the typical receiver temperature can be reduced to ~ 5K at the 1cm wavelength (Levin et al., 2001). Then the system temperature would be reduced to ~ 50K so that it would allow to explore the calm dark cloud cores using SO(1_0-0_1) line with the sensitivity down to the 50 μG range. In general, the velocity gradient is

often smaller in these regions. Therefore one can avoid the beam squint effect easily. More efforts are needed to prove that SO 30GHz transition is a promising tool for Zeeman observations.

Reference

Adatia, N. A., Rudge, A. W., October, 1975, *Electronics Letters*, vol.11, no.21, 513.

Bel, N., Leroy, B., 1989, A&A, 224, 206.

Brogan, C. L., and Troland, T. H., 2001, ApJ, 550, 799.

Brogan, C., Frail, D. A., Goss, W. M., Troland, T. H., 2000, ApJ, 537, 875.

Brogan, C., Troland, T. H., Roberts, D. A., Crutcher, R., 1999, ApJ, 515, 304.

Chandler, C., J., Moore, T. J. T., Mountain, C. M., Yamashita, T., 1993, MNRAS, 261, 694.

Chu, T.-S., Turrin, R.H., May, 1973, *IEEE Trans. Antennas Propagat.*, vol. AP-21, 339.

Clark, F. O., Johnson, D. R., Heiles, C. E., Troland, T. H., 1978, ApJ, 226, 824.

Claussen , M. J., Frail, D. A. and Goss, W. M., 1997, ApJ, 489, 143.

Crutcher, R. M., Troland, T. H., Goodman, A. A., Heiles, C., Kazès, and Myers, P. C., 1993, ApJ, 407, 175.

Crutcher, R. M., Troland, T. H., Lazareff B., Kazès, I., 1996, ApJ, 456, 217.

Crutcher, R. M., Troland, T. H., Lazareff, R., Paubert, G., Kazès, I., 1999, ApJ, 514, L121.

Crutcher, R. M., 1999, ApJ, 520, 706.

Cwik, T., Jamnejad, V., 1997, TDA Progress Report, 42, 128.

Duan, D.-W., Rahmat-Samii, Y., May, 1991, *IEEE Trans. Antennas Propagat.*, vol. AP-39, 612.

Fiebig, D., Güsten, R., 1989, A&A, 214, 333.

Fiebig, D., 1990, Ph.D. Thesis, Univ. Bonn.

Fiebig, D., Rohlleben, R., Prata, A., Rusch, W. V. T., June, 1991, *IEEE Trans. Antennas Propagat.*, vol. AP-39, 774.

Güsten, R., Fiebig, D., and Uchida, K. I., 1994, A&A, 286, L51.

Heiles, C., Goodman, A. A., McKee, Ch. F., Zweibel, E. G., 1991, IAUS, 147, 43.

Irvine, W. M., Goldsmith, P. F., Hjalmarson, Å., 1987, in *Interstellar Proces*, eds. D.J., Hollenbach, H. A., Thronson, Dordrecht, pp. 561.

Levin, S. M., Langer, W. D., Velusamy, T., Kuiper, T. B. H., Crutcher, R. M., 2001, ApJ, 555, 850.

Mangum, J. G., Wooten, A., Mundy, L. G., 1992, ApJ, 388, 467.

McKee, C. F., Zweibel, E. G., Goodman, A., A., Heiles, C., 1993, in Protostars and Planets III, ed. E.H. Levy & J. I. Lunine, 327.

Mestel, L., Spitzer, L., 1956, MNRAS, 116, 503.

Mestel, L., 1966, MNRAS, 133, 265.

Mouschovias, T., Ch., 1985, A&A, 142, 41.

Mouschovias, T. Ch., Spitzer, L., Jr., 1976, ApJ, 210, 326.

Mouschovias, T. Ch. 1987, in *Physical Processes in Interstellar Clouds*, ed.: G. E. Morfill and M. Scholer, 453.

Padin, S., Sargent, A.,I., Mundy, L. G., Scoville, N. Z., Woody, D. P., Leighton, R. B., Masson, C. R., Scott, S. L., Seling, T. V., Staphelfeldt, K. R., Terebey, S., 1989, ApJ, 337, L45.

Sault, R. T., Killeen, N. E. B., Zmuidzinas, J., and Loushin, R. 1990, ApJS, 74, 437.

Shinnaga, H., Tsuboi, M., and Kasuga, T., 1999, Proc. of Star Formation, 175.
Shinnaga, H., and Yamamoto, S., 2000, ApJ, 544, 330.
Shu, F. H., Allen, A., Shang, H., Ostriker, E. V., Li, Z.-Y., in *The Origin of Stars and Planetary Systems*, eds. C. J. Lada and N. D., Kylafis, pp.193-226.
Solomon, J. E., Johnson, D. R., and Lin, C. C., "Low-Field Zeeman Effect of the Microwave Spectrum of the SO Radical", 1968, J. Mol. Spectrosc., 27, 517.
Tomisaka, K., Ikeuchi, S., Nakamura, T., 1988, ApJ, 335, 239.
Troland, T. H., Heiles, C., 1982, ApJ, 252, 179.
Uchida, K.I., 1994, unpublished data.
Uchida, K. I., Fiebig, D., and Guesten, R., 2001, A&A, 371, 274.
Wilson, T., L., Mauersberger, R., 1993, A&A, 239, 305.
Zinchenko, I., Henkel, C., Mao, R. Q., 2000, A&A, 361, 1079.

Chapter 4
CO(4-3) and CI($^3P_1$-$^3P_0$) observations on W51 region with CHAMP

4.1 Introduction

4.1.1 The CHAMP array

CHAMP (the Carbon Heterodyne Array of the MPIfR) is a 16-element SIS heterodyne array for operation in the 625 μm atmospheric window (Güsten et al., 1998). The array consists of 2 × 8 elements, with $(2\theta_{mb})^{1/2}$ spacing of the pixels on the sky, where θ_{mb} = 16" is the beamwidth of the pixel. The L.O. tuning range covers the astronomically important CI($^3P_1$-$^3P_0$) and the CO(4-3) transitions, and an IF bandwidth of 2 GHz (1200 km s^{-1}) permits mapping of extragalactic systems. With CHAMP in SSB (single-sideband) operation mode and good submillimeter weather conditions, the receiver temperatures are well below 1000 K, and the mapping speed is enhanced by more than an order of magnitude compared to current single-pixel detectors. The CHAMP array was installed at the Caltech Submm Observatory (CSO) 10.4m sub-mm telescope on Mauna Kea (Hawaii) from the end of 1998, and had its first-light in Febuary 1999 on Orion-KL. Until now, a wide variety of sources has been observed. The prominent galactic star forming cloud W51 was observed in spring 2001.

4.1.2 The W51 Complex

The W51 complex is a giant molecular cloud (GMC) and massive star-forming region located in the Sagittarius spiral arm ~7.5 kpc away (Genzel et al., 1981; Schneps et al., 1981. 1"~ 0.036 pc). W51 is divided into four components (Kundu & Velusamy, 1967). The radio continuum sources G49.4-0.3 and G49.5-0.4 are classically referred to as W51A. W51B consists of the G49.2-0.3, G49.1-0.4, and G48.9-0.3 subcomponents. W51C consists of G49.0-0.5 and G49.2-0.7, and is a supernova remnant (SNR). W51D contains the subcomponent at G48.6+0.0. In this chapter, only the G49.5-0.4 component is investigated.

The structure of W51 is complex because the line of sight intersects the Sagittarius arm tangentially (Burton & Shane, 1970). There are at least four different clouds towards the center of G49.5-0.4 (Arnal & Goss, 1985; Okumura et al., 2001). In the high resolution centimeter observation towards W51A, several discrete components are detected in the 6 cm band and assigned as W51 **a** to **g** (Martin, 1972). West of W51**e** by ~ 30", W51**e1** and **e2** are two small ultra-dense contracting molecular cores with masses of ~10^2 $M_\odot$ (Scott, 1978). From IR observation (Wynn-Williams et al. 1972), the peaks IRS1 and IRS2 correspond well to W51**e** and **d** in the centimeter map. Water maser emission is also detected towards these two regions and denoted as W51South and W51Main (near **e1**/**e2**) and W51N (near **d** and IRS2) (Genzel & Downes, 1977), respectively. The spatial distribution of free-free emission from ionized gas at 6cm (Mehringer, 1994) and Mid-IR (21.3 μm) emission from warm dust (MSX, Midcourse Space Experiment) resemble each other.

Thus, the W51A/G49.5-0.4 region (hereafter simple W51) can be divided into three regions of interest: (1) the W51**e** (IRS1) region, (2) the W51**e1**/**e2** (W51Main/South) region, and (3) the W51**d** (IRS2,W51N) region. W51**e** is a long curving structure, where the free-free emission dominates. Though IRS1 is the brightest source in the 6 cm map, it does not contain much mass, as traced by cool dust (Jaffe et al., 1984). From the infrared and radio continuum observations,

Genzel et al. (1982) suggested that W51**e** is powered by an embedded cluster of early O stars from the east. W51**d** and W51**e1**/**e2**, where dense molecular clouds shroud O and B stars, are the densest regions revealed by the ammonia and dust emission observations ($n(H_2) \sim 10^6$ cm^{-3}. Zhang & Ho, 1997; Sievers et al., 1991). The maps of high density tracers also show compact distributions with peaks near W51**e1**/**e2** and W51**d** (Rudolph et al., 1990; Zhang et al., 1998). As the 400 μm emission shows (Jaffe et al., 1984), the dust temperature of the W51**d** region (50 to 60 K) is warmer than the W51 **e1**/**e2** region (~ 35 K). The total luminocity of W51 **e1**/**e2** and W51**d** are 2×10^6, and 4×10^6 $L_\odot$, respectively. The W51**d** region contains a smaller amount of mass than W51**e1**/**e2** (Jaffe et al., 1987).

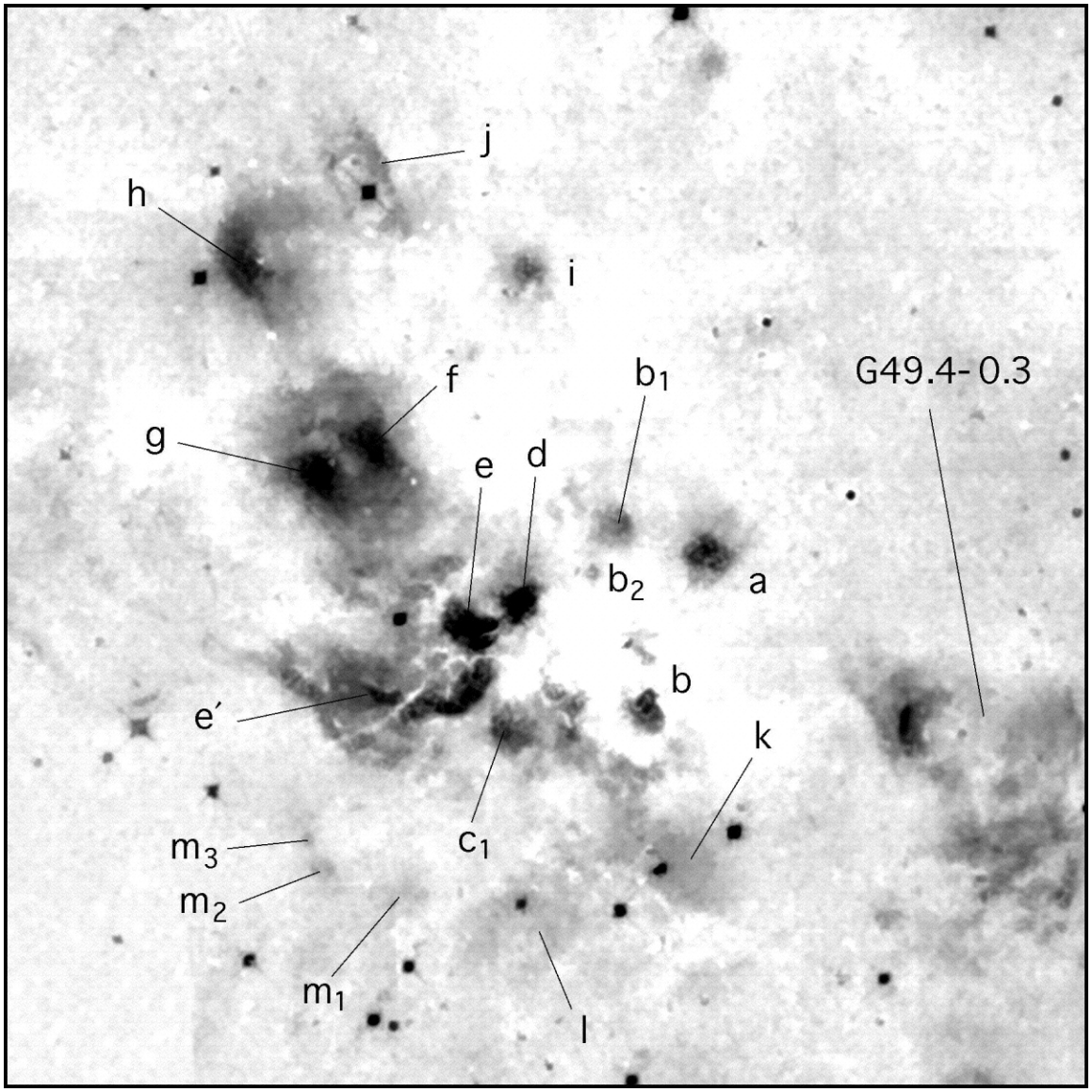

Fig. 4.1. Near-infrared K'-band image of the central part of the W51A complex from Okumura et al. (2000). The notation **a-i** are the HII region components identified by Martin (1972). The notations **j-m** are the HII region components identified by Okumura et al. (2000).

Many observations show the existence of several discrete velocity components in the W51 molecular clouds. Carpenter & Sanders (1998) performed a large scale map with CO(1-0) and ^{13}CO(1-0) at 45" resolution. They separated the velocity components at 7, 15-25, 44, 49, 53, 58, 60, 63 and 68 km/s by Gaussian decomposition. The 58, 60 and 63 km/s components are defined as the W51 giant molecular cloud (GMC). The 53 km/s feature belongs to another G49.4-0.3 cloud in the south-west of W51 GMC. The relation between the 53 km/s and the W51GMC clouds is unclear. The 68 km/s cloud belongs to the "high-velocity stream". From the recombination line data (Arnal & Goss, 1985; Koo, 1997), the cloud with higher velocity is closer to the earth. Arnal & Goss (1985), Carpenter & Sanders and Okumura et al. (2001) suggested that star-forming activities in the region were triggered by collisions of the clouds.

4.1.3 The origin of atomic carbon in the interstellar medium

Here we present new CO(4-3) and CI($^3P_1$-$^3P_0$) CHAMP observations of W51. In this measurements, CO(4-3) emission is a tracer of the warm (T~ 50 K) and dense (n ~ 10^5 cm^{-3}) molecular gas, whereas CI exists mainly in the photodissociation regions (PDR, or photon dominated regions) in the outer parts of the molecular clouds. Photodissociation of CO is believed to be the main mechanism to form atomic carbon. According to the prediction by standard PDR models (Tielens & Hollenbach, 1985; and many subsequent papers), carbon is primarily in the form of atomic carbon near the surface (A_v~ 2-7) of molecular clouds. A simple one-dimensional morphology of a photodissociation region is shown in Fig. 4.2(a) (Tielens & Hollenbach, 1985).

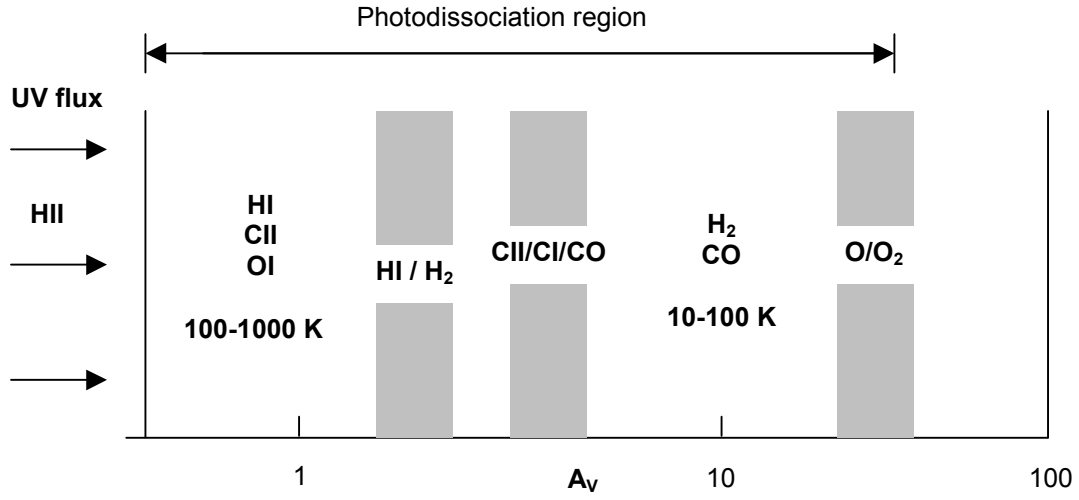

Fig. 4.2(a). A schematic drawing of a photodisscіation region from Tielens & Hollenbach (1985). The PDR is illuminted from the left. The numbers show the gas temperature.

In the PDR, molecular gas is dissociated by far-ultraviolet (FUV) photons from nearby stars. Because the ionization energy of carbon is very close to the photodissociation energy of CO, atomic carbon is expected to exist only in a thin layer at the surface of molecular clouds, if the atomic carbon is produced via the photodissociation of CO. Observational data show that atomic carbon abudances are still high deep within the clouds (Philips & Huggins, 1981; Genzel et al., 1988 etc.). These observations cannot be explained with standard PDR models. Stutzki et al. (1988) and Genzel et al. (1988) explained it by clumpy structure that allows far-UV photons to

penetrate into the interiors of the clouds. Then Meixner & Tielens (1993, 1995) and Spaans (1996) proposed clumpy PDR models to explain the unexpected spatial distribution of the atomic carbon emission. Other explanations to the high CI abundance in the interior of a dense cloud are time-dependent chemistry models (Lee et al. 1996; Störzer et al. 1997) and the bistable solutions in the models (Pineau des Forêts et al., 1992; Le Bourlot et al., 1993; Flower et al., 1994). Because the chemical timescale converting CI to CO is comparable to the dynamical timescale of a dense core of $n(H_2) \sim 10^4$ cm^{-3}, the time-dependent model predicts that the carbon can coexist with CO for a while even after UV radiation is shielded. It provided good explanation for the chemically young cloud like Heiles cloud 2 (Maezawa et al., 1999). The bistable model predicts that there are two phases in the chemical equilibrium state, high-ionization phase (HIP) and low-ionization phase (LIP). In the HIP cloud, it provides good explanations for the high constant CI/CO ratio (~ 0.1) found in the deeply embedded dense cores. These models (PDR, time-dependent and bistable models) can also be combined together.

In general, the viewing angle to the line of sight of the observed PDR is unknown. Thus, one has to confirm first from which layer the emission comes to correctly interprete the observational data. For example, Fig. 4.2(b) shows a two dimensional "onion" PDR model. The line-of-sight would go through several layers of the PDR, depending on the opacity of the tracing molecules. The optically thin lines would probably sample the whole cloud throughout, whereas the optically thick emission contains only the information of the foreground gas. When one observes the core region where the PDR is seen face-on, the CO and CI emission is homogeneous and co-spatial. Towards the edge, however, where the PDR is viewed edge-on, the relative intensity of CI/CO and the column density of CI would show dramatic changes within short distance. In the ideal case, like the Orion Bar region, one might observe the parallel layers (excitation source / ionization front / HI layer / H_2 emission / CO emission) predicted by the PDR model (Hollenbach & Tielens, 1997). In general, however, one seldom observes such a beautiful morphology.

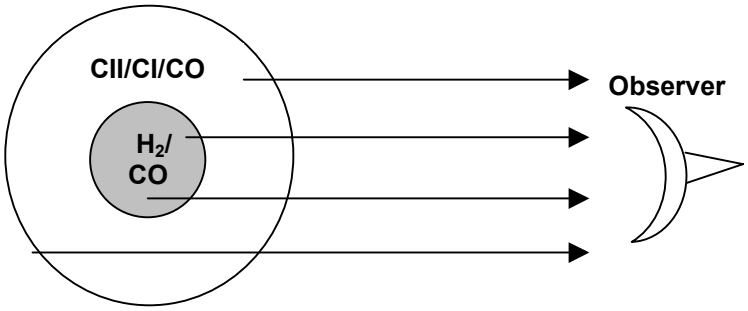

Fig. 4.2(b). The "onion" PDR model (not to scale). With different molecules and different viewing angles, different PDR layers are included in one beam.

Hollenbach et al. (1991) performed calculations with plane parallel PDR models and showed that the CI column density increases by only a factor of 2 as the illuminated UV field strength G_0 increases by five orders of magnitude. Increasing G_0 simply increases the depth into the cloud where the CII/CI/CO transition occurs, but the column density across this transition remains constant. The density dependence of N(C) is also weak. The CI column density predicted by plane parallel PDR models illuminated on one side is $\sim 2 \times 10^{17}$ cm^{-2}, when $n(H_2) = 10^4$ cm^{-3}. The spatial difference of N(C) in the observation may mainly come from the geometrical effect as discussed above.

4.2 CHAMP Observations towards the W51 region

4.2.1 Observations and data reduction

We used CHAMP to observe the CO(4-3) (461 GHz) and CI($^3P_1$-$^3P_0$) (492 GHz) lines in April 2001. In this frequency range the half-power beamwidth is ~16" to 18" (~ 0.6 pc at 7.5 kpc). The MACS (MPIfR AutoCorrelation Spectrometer) backend provides high spectral resolution (~ 0.15 km/s). In the CHAMP array, the beam efficiency varies slightly from pixel to pixel. From the measurements with Jupiter and Mars, the average beam efficiency is ~0.5 (Güsten, priv. comm.). Since the final spectrum at each position in the map is obtained from the average of several spectra from different pixels, we used the average value for the following calculations.

The center position of the observation is R.A.(1950) = $19^h21^m22.3^s$ Dec.(1950) = 14°25'15". The CO(4-3) data were observed in the on-the-fly frequency switching mode, whereas CI data were mapped using the frequency switching mode at a grid of positions spaced by 16". In the on-the-fly observations, the spectra in the beginning or at the end of the map in each subscan were selected carefully as reference scans to subtract the bandpass. The reference scan for the CI reduction is (0,-500") away from the center position. The "chopper-wheel" calibration procedure was employed (Ulich & Haas, 1976) in the observation every half an hour. The data reduction was carried out using the OTFCHAMP program.

4.2.2 Results

The integrated intensity maps (v = 45 to 75 km/s) and spectra at selected points are shown in Fig. 4.3. The peak temperatures, central velocities and FWHM linewidths obtained by Gaussian-fitted decomposition at the selected positions are listed in Table 4.1. The line profiles in the region are complex, but in general, all the spectra can be decomposed into two or three components. CO is observed at velocities of ~ 50, 54, 60 and 69 km/s. CI components are at velocities of ~ 50, 56, 62 and 68 km/s. All the spectra are within a velocity range from 45 to 75 km/s, in good agreement with other CO observations (Carpenter & Sanders, 1998; Okumura et al., 2001).

The line profiles differ quite dramatically in the region. Towards some positions, CI shows profiles that are similar to those of CO (i.e. (-100",0), (100",-50")). In some position like W51**e**, the lineshapes are totally different. Here the CO profile shows two discrete components or a deep absorption feature at 65 km/s, whereas CI shows only a single feature covering most of the velocity range of the CO emission (Fig. 4.3). The high velocity stream (at ~68 km/s) is obvious in all CO(4-3) spectra, only at the eastern part its intensity is weaker (i.e. (150",0)). However, in CI this 68 km/s component is evenly distributed and the intensity is generally low (between 1 to 1.5 K).

The most prominent area of the CO(4-3) emission is between W51**d**, W51**c1**, (100",50") and (-50",-50"). The signal-to-noise ratio in CI is lower than that of CO(4-3), because CI emission is at the edge of the atmospheric window. The data at the map edge are therefore neglected and the contour level of CI starts from 50% of the peak value. The region of strongest integrated CI emission is offset to the east from the peak position of CO(4-3) emission by ~ 30" (1.1 pc). This distance is larger than the beamwidth of the pixel in CHAMP array, thus we do not think this comes from pointing or instrumental errors.

Table 4.1. A comparison of CI ($^3P_1$-^3P_o) and CO(4-3) line parameters for the W51 region. For simplicity, all lines are assumed to be Gaussian and neglect the self-absorption features.

	T_a* (K)		V_{LSR} (km/s)		ΔV (km/s)	
Position (offset in arcsec)	**CI ($^3P_1$-^3P_o)**	**CO(4-3)**	**CI ($^3P_1$-^3P_o)**	**CO(4-3)**	**CI ($^3P_1$-^3P_o)**	**CO(4-3)**
W51b (-108,-68)	1.8 (0.3)	7.9 (0.8)	48.7 (0.1)	50.8 (0.2)	7.2 (0.4)	8.1 (0.4)
	1.4 (0.3)	15.2 (0.8)	61.0 (0.1)	58.7 (0.1)	3.6 (0.3)	4.6 (0.1)
	1.3 (0.3)	10.6 (0.8)	68.2 (0.1)	67.5 (0.1)	4.5 (0.4)	9.2 (0.2)
W51c1 (21,-83)	1.9 (0.1)	18.0 (1.0)	53.5 (0.1)	51.2 (0.2)	9.8 (0.3)	8.3 (0.3)
		24.0 (1.0)		60.0 (0.2)		8.7 (0.3)
	1.5 (0.1)	6.8 (1.0)	65.3 (0.1)	70.2 (0.2)	9.4 (0.3)	3.7 (0.3)
W51d (0,0)	2.7 (0.2)	16.1 (0.5)	50.5 (0.1)	50.5 (0.1)	5.8 (0.1)	7.7 (0.2)
	3.6 (0.2)	28.2 (0.5)	60.7 (0.1)	58.7 (0.1)	7.4 (0.2)	7.5 (0.1)
	1.5 (0.2)	8.9 (0.5)	68.1 (0.2)	69.3 (0.1)	6.4 (0.3)	7.2 (0.1)
W51e (30,-32)	1.0 (0.1)	21.4 (0.7)	51.5 (0.2)	52.9 (0.2)	8.1 (0.2)	10.1 (0.2)
	3.6 (0.1)	16.4 (0.7)	59.9 (0.2)	58.5 (0.2)	12.3 (0.2)	7.2 (0.2)
	1.5 (0.1)	6.6 (0.7)	66.5 (0.2)	69.1 (0.2)	8.2 (0.2)	5.8 (0.2)
W51e1/e2	3.7 (0.1)	19.6 (0.6)	54.4 (0.1)	51.9 (0.1)	7.8 (0.1)	8.5 (0.1)
(57,-34)	3.0 (0.1)	15.9 (0.6)	61.1 (0.1)	58.1 (0.1)	8.1 (0.3)	8.3 (0.1)
	1.7 (0.1)	5.7 (0.6)	68.3 (0.1)	68.9 (0.1)	5.1 (0.2)	4.9 (0.2)
(50,50)	2.6 (0.2)	14.4 (0.4)	51.4 (0.1)	51.5 (0.1)	4.4 (0.1)	5.6 (0.1)
	4.2 (0.2)	25.2 (0.4)	61.5 (0.1)	60.4 (0.1)	5.7 (0.1)	6.5 (0.1)
	0.9 (0.2)	4.2 (0.4)	68.1 (0.1)	67.5 (0.1)	3.8 (0.4)	1.7 (0.1)
(-50,50)	0.8 (0.2)	7.6 (0.4)	50.7 (0.3)	51.2 (0.2)	4.8 (0.3)	7.6 (0.2)
	1.8 (0.2)	15.9 (0.4)	62.9 (0.2)	61.3 (0.2)	11.2 (0.8)	7.6 (0.2)
		5.8 (0.4)		68.7 (0.2)		5.7 (0.2)
(-50,-50)	1.6 (0.1)	14.6 (0.7)	49.8 (0.1)	49.1 (0.1)	5.8 (0.2)	6.4 (0.1)
	1.7 (0.1)	21.6 (0.7)	64.2 (0.1)	59.0 (0.1)	10.1 (0.2)	9.9 (0.2)
		12.4 (0.7)		71.1 (0.1)		6.0 (0.1)
(0,100)	0.8 (0.2)	8.0 (0.6)	50.6 (0.3)	50.2 (0.2)	4.0 (1.0)	3.5 (0.2)
	1.9 (0.2)	17.0 (0.6)	62.2 (0.3)	60.2 (0.2)	7.8 (0.5)	7.2 (0.2)
		7.0 (0.6)		68.3 (0.2)		2.7 (0.2)
(-100,0)	1.5 (0.2)	9.0 (0.4)	49.9 (0.1)	55.3 (0.1)	4.4 (0.3)	15.0 (0.1)
	2.3 (0.2)	9.0 (0.4)	60.5 (0.1)	59.4 (0.1)	6.5 (0.3)	6.7 (0.1)
	1.2 (0.2)	7.8 (0.4)	68.3 (0.1)	68.9 (0.1)	4.4 (0.5)	7.3 (0.1)
(150,0)	1.0 (0.2)	12.0 (0.5)	52.9 (0.2)	54.7 (0.2)	4.0 (0.5)	8.3 (0.2)
	2.2 (0.2)	13.8 (0.5)	59.4 (0.3)	60.6 (0.2)	9.6 (0.6)	4.9 (0.2)
		1.7 (0.5)		68.8 (0.2)		2.3 (0.2)
(100,-50)	5.1 (0.1)	21.0 (0.6)	55.6 (0.1)	53.5 (0.1)	9.6 (0.1)	8.2 (0.2)
		13.0 (0.6)		61.1 (0.1)		5.3 (0.2)
	1.5 (0.1)	5.1 (0.6)	68.3 (0.1)	68.2 (0.1)	3.9 (0.1)	3.2 (0.2)
(100,-150)	2.9 (0.3)	15.8 (0.7)	55.2 (0.1)	58.0 (0.1)	5.8 (0.1)	11.9 (0.2)
	1.0 (0.3)		61.4 (0.1)		7.7 (1.2)	
	1.8 (0.3)	5.6 (0.7)	68.7 (0.1)	69.7 (0.1)	3.8 (0.2)	3.6 (0.2)
(150,-100)	3.3 (0.4)	13.5 (0.8)	57.7 (0.1)	56.4 (0.3)	8.6 (0.1)	9.4 (0.4)
		13.7 (0.8)		61.4 (0.1)		4.6 (0.2)
	0.8 (0.4)	4.8 (0.8)	67.8 (0.1)	67.7 (0.1)	3.2 (0.3)	1.6 (0.2)
(150,-200)	2.9 (0.3)	9.0 (0.7)	56.4 (0.8)	55.4 (0.2)	3.9 (0.8)	6.5 (0.3)
	1.3 (0.3)	9.4 (0.7)	61.2 (0.8)	62.4 (0.1)	4.8 (0.8)	5.6 (0.3)
	0.7 (0.3)	6.2 (0.7)	69.2 (0.8)	68.9 (0.1)	9.5 (0.8)	6.4 (0.2)

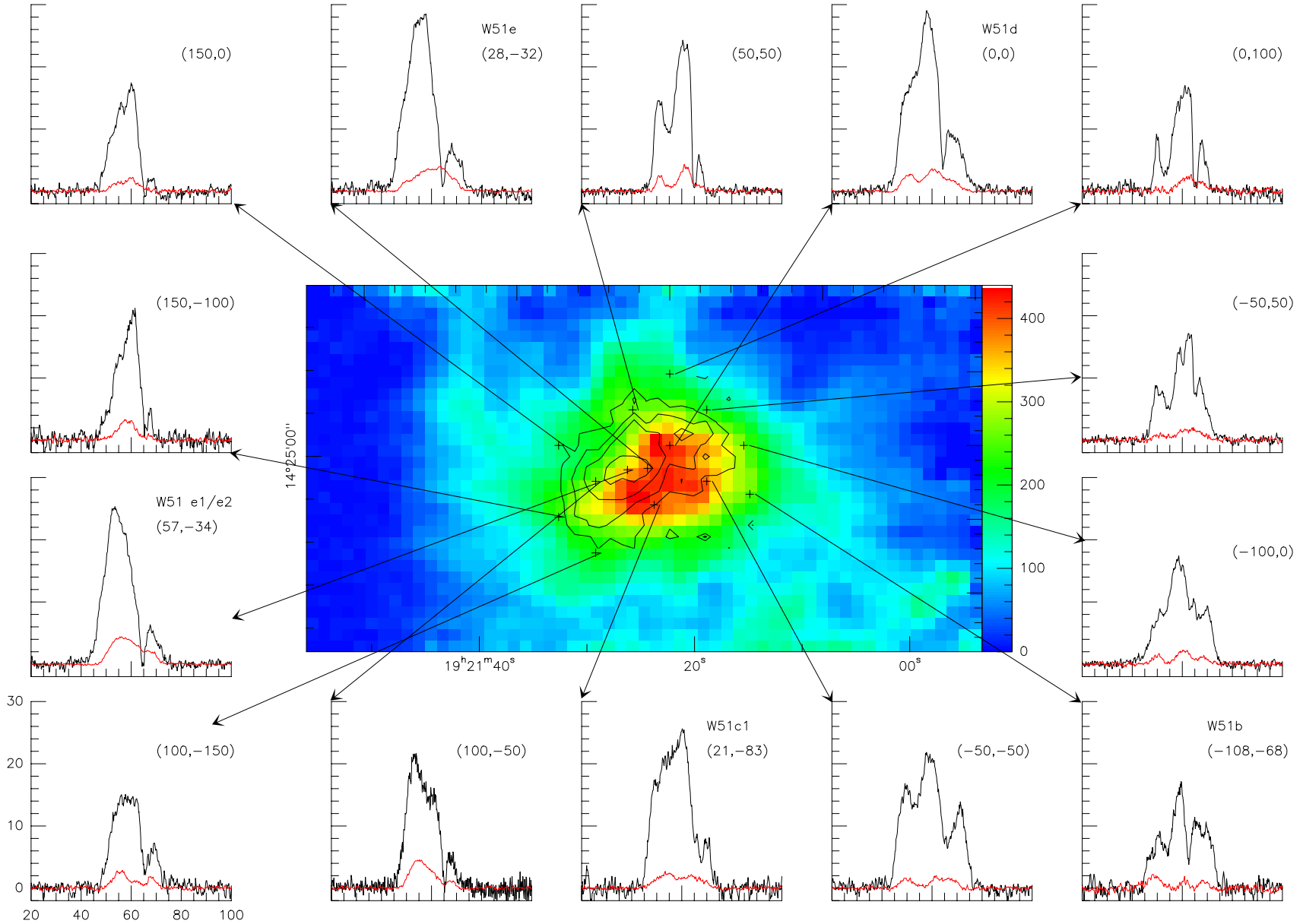

Fig.4.3. CO(4−3) (black) and CI($^3P_1-^3P_0$) (red) spectra (in Ta^* scale) at selected positions toward W51. The horizontal axis in each spectrum is velocity (km/s). The number in the upper right of each spectrum give its position offset in arcsec from W51d. In the center panel shows $\int Ta^*(CO(4-3))dv$ (color) and $\int Ta^*(CI(^3P_1-^3P_0))dv$ (contours, contour levels from 30 to 60 by 10 K kms^{-1}) between v = 45 to 75 km/s

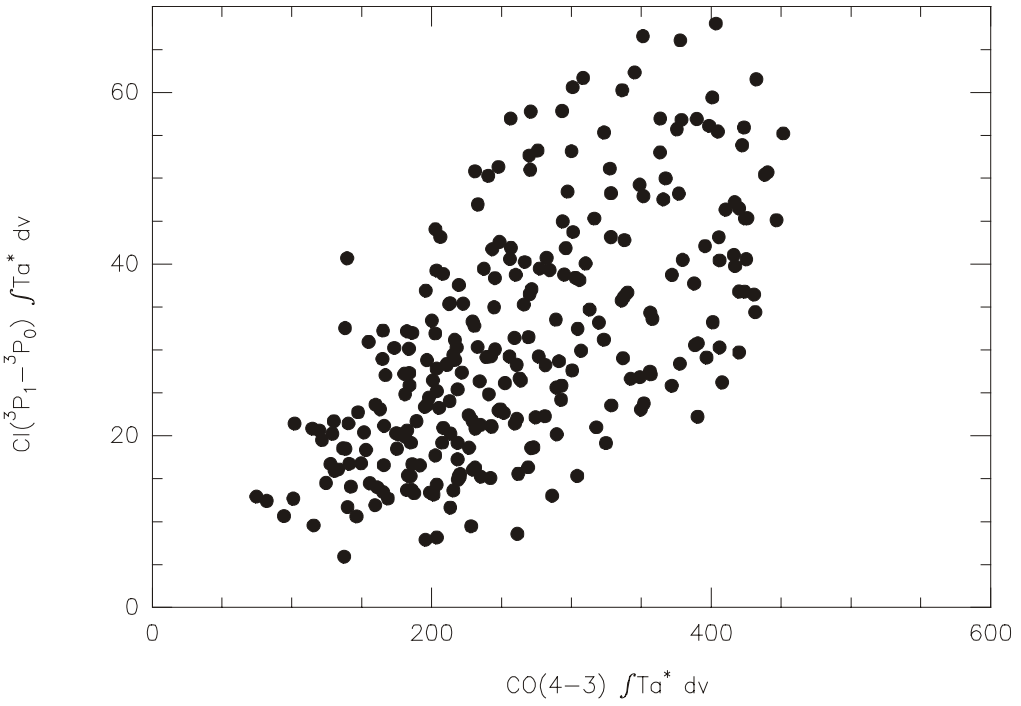

Fig.4.4(a). Correlation of the CI(^{3}P$_1$−^{3}P$_0$) and CO(4−3) maps, integrated between 45 and 75 km s^{-1}.

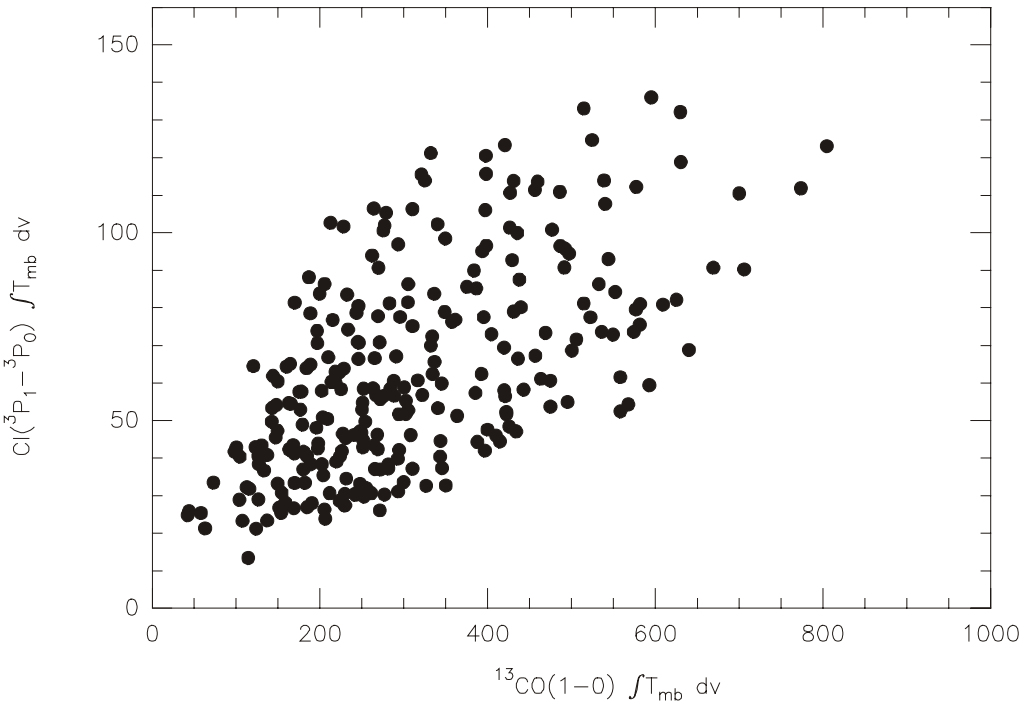

Fig.4.4(b). Correlation of the CI(^{3}P$_1$−^{3}P$_0$) and ^{13}CO(1−0) (Okumura et al., 2001) maps, integrated between 45 and 75 km s^{-1}.

From Table 4.1 we can see that the intensity ratio $T_a^*(CI)/T_a^*(CO(4-3))$ of each component is in the range of 0.1 to 0.25. The ratio of the integrated intensities $I_{CI} / I_{CO(4-3)}$ is plotted in Fig. 4.4(a). The ratio varies from 0.03 to 0.29, with a mean of 0.12 ± 0.04. The ratio is high from the central region to the north-east. It is low to the south-west and low at the edges of the map.

Many observations reported that there is an linear relation between the integrated intensity, line profile and spatial distribution of CI and low level ^{13}CO emission (TMC-1: Schilke et al., 1995; M17, S140: Keene, 1985; S140, W3, NGC2024 and Cep A: Plume et al., 1994, 1999; Orion Bar: Tauber et al., 1995; OMC-1, Oph A and M17: Keene et al., 1996). This may imply that the interstellar medium is clumpy and the gas in the dense cores and the gas in the PDRs are closely related. Together with the ^{13}CO(1-0) data from Okumura et al. (2001) obtained with a 16" beam, we compared the integrated intensity directly and plotted the data in Fig. 4.4(b). In Fig. 4.4(b) we find that the correlation coefficient is 0.54. This correlation is not as striking as in the Orion Bar, M17 and Oph A cases. The best linear fit to the data is $I_{CI} / I_{13CO} = 0.035$. Compared with the observations listed above, whose ratio are generally close to 1, this ratio is very low. This may be caused from the complicated structure of the W51GMC and many unrelated clouds were included in the measurements.

On the other hand, one also knows that in active or star-forming regions like Orion South and regions with massive star formation, the resemblance is generally less significant (Tauber et al., 1995; Ikeda et al., 2002). This is probably due to the presence of very high density ($n > 10^5$ to 10^6 cm^{-3}) gas. The percentage of ^{13}CO molecules relative to atomic carbon in the PDR is lower (Tauber et al., 1995; Keene et al., 1996). In our case, since W51 is a massive star formation region with high density, the weak correlation between CI and ^{13}CO emission shown in Fig. 4.4(b) could be due to this effect. However, the complex structure is likely the most important reason.

4.3 Morphology

4.3.1 CO(4-3) emission

The CO(4-3) emission is extended with a peak between W51**d**, W51**e1**/**e2** and W51**c1** (Fig.4.3). The cloud is irregular and the FWHM size of the cloud ($\Delta\alpha$, $\Delta\delta$) is ~ 5' × 3.5' (10.9 pc × 7.6 pc). In Fig. 4.5, the CO(4-3) is overlaid on ^{13}CO(1-0) (Okumura et al., 2001). Except towards the dense regions W51**e1**/**e2** and W51**d**, where there is an offset of ~ 20" between the peak positions (Table 4.2), the spatial distributions of CO(4-3) and ^{13}CO(1-0) are similar on large scale. The peak of the integrated ^{13}CO(1-0) distribution is located at the W51**e1**/**e2** region.

In Fig. 4.6, the integrated CO(4-3) map was overlaid onto a 6cm continuum map with 5" resolution obtained with the VLA (Mehringer, 1994). We find that in the central region, the two peak positions of CO(4-3) are shifted to the south-west of the compact HII regions **d** and **e** by 12" and 40" respectively. There appear to be no counterparts in the CO map corresponding to **a**, **b**, **c1**, **f** and **g** in the 6 cm image. As mentioned before, the Mid-IR emission arising from the warm dust (image resolution ~20") is very similar to that of the 6 cm map, especially around W51**d** and **e**. Therefore we do not show it here.

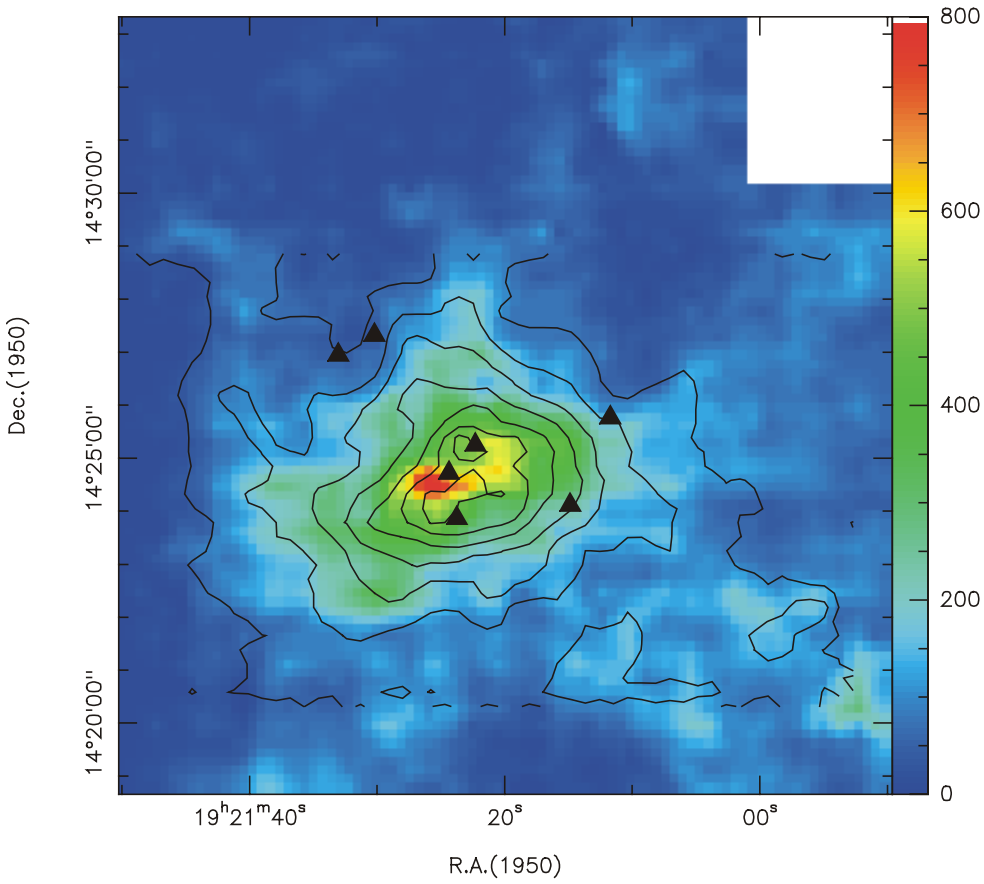

Fig.4.5. Color: $\int T_{mb}(^{13}CO(1-0))dv$ from Okumura.
Contour: $\int Ta^{*}CO(4-3)dv$ as in fig. 4.3,
contour levels from 60 to 480 by 60 K kms^{-1}.
The triangules show W51a–g found in 6cm.

The spatial distribution of mm wavelength continuum data from Sievers et al. (1991) at 1.3 mm can give us information related to the cold gas. There are two dominant regions in the mm-wave map, the north one is near W51**d** and the east one is near W51**e1**/**e2** (Fig. 4.7). By comparing Sievers' 1.3 mm data with CO(4-3), on large scales we can also see that the 1.3 mm map follows well the broad clouds in the south shown in CO(4-3). Though the whole spatial distribution of the 1.3 mm continuum emission is slightly different from those of CO, it looks like a superposition of CO(4-3) and ^{13}CO(1-0). Therefore it may trace the same general volume as these two CO lines. For the 6cm continuum **a**, **b**, **c**, **f** and **g** HII regions, one finds no counterparts in the 1.3 mm dust emission. Table 4.2 is a summary of the peak positions in various survey towards the W51 region. From the slighty different spatial distribution of the maps, for the two dense region W51**e1**/**e2** and W51**d**, we suggest that the W51**e1**/**e2** region is cold, therefore 1.3 mm and ^{13}CO(1-0) peak in that region. Towards W51**d** region the cold and warm gas seems to be well mixed, because CO(4-3) and 1.3 mm both peak there.

One can see the spatial distribution of these velocity components in the channel maps in Fig. 4.8. Neglecting the clouds at the south-west (at 53 km/s) and eastern (at 65 km/s) edge, the clouds traced by CO(4-3) can be roughly divided into four different velocity components at 50, 56, 61 and 68 km/s. The other channel maps in between can be treated as linear combinations of these clouds. This classification of the clouds is similar to Arnal & Goss (1985) and Okumura et al. (2001).

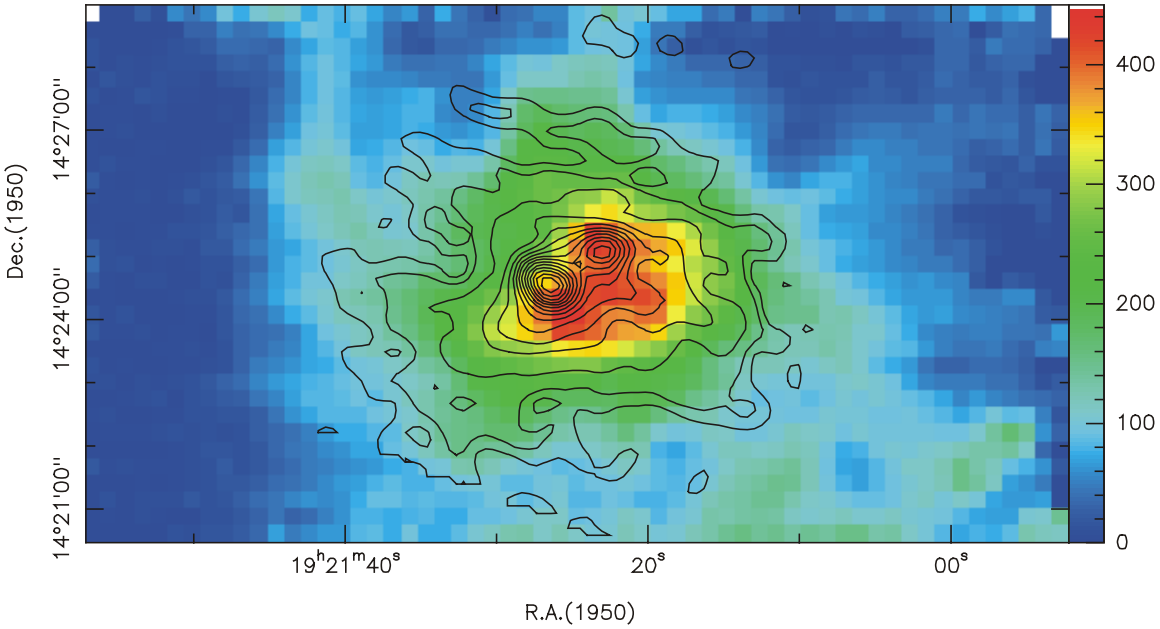

Fig.4.6. Color: $\int Ta^*(CO(4-3))dv$ as in fig. 4.3.
Contour: 1300μm observation from Sievers et al. (1991).
contours are 500, 1000 and 2000 to 30000 by 2000 mJy/beam.

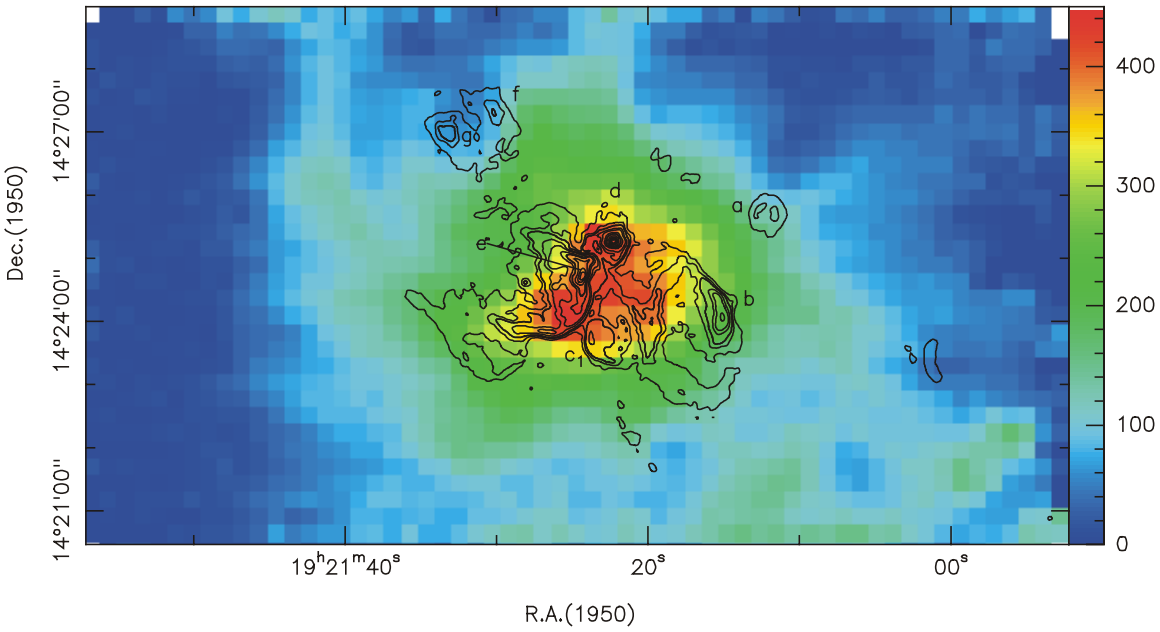

Fig.4.7. Color: $\int Ta^*(CO(4-3))dv$ as in fig. 4.3.
Contour: 6cm observation from Mehringer (1994),
contours are at 0.01, 0.03, 0.05, 0.1, 0.15, 0.3, 0.45,
0.75, 1.05, 1.35 1.65, 1.95 Jy/beam.

Table 4.2. Summary of peak positions in different observations.

	R.A. (1950)	Dec(1950)	Note
W51d	19h 21m 22s.3	+14° 25' 15"	IRS 2
1.3 mm	19h 21m 23s.0	+14° 25' 05"	Sievers et al. (1991)
W51N	19h 21m 22s.3	+14° 25' 19"	Genzel and Downes (1977)
^{13}CO(1-0)	-	-	
CO(4-3)	19h 21m 23s.0	+14° 25' 09"	**CHAMP**, extended to the west
CI($^3P_1$-$^3P_0$)	19h 21m 21s.2	+14° 25' 31"	**CHAMP**

	R.A. (1950)	Dec(1950)	Note
W51e	19h 21m 24s.2	+14° 24' 43"	IRS 1
W51e1	19h 21m 26s.1	+14° 24' 33"	dense star-forming core
W51e2	19h 21m 26s.2	+14° 24' 41"	dense star-forming core
1.3 mm	19h 21m 26s.5	+14° 24' 33"	Sievers et al. (1991)
W51Main	19h 21m 26s.3	+14° 24' 43"	Genzel and Downes (1977)
^{13}CO(1-0)	19h 21m 25s.7	+14° 24' 28"	Okumura et al. (2001)
CO(4-3)	19h 21m 25s.2	+14° 24' 06"	**CHAMP**
CI($^3P_1$-$^3P_0$)	19h 21m 26s.4	+14° 24' 43"	**CHAMP**

The channel maps give us a totally different view of W51. For v = 49 to 53 km/s, the peak of CO(4-3) is around the UC HII region W51**e1**/**e2**. It implies that the densest region of the 50 km/s cloud is also at the W51**e1**/**e2** region (Mehringer, 1994). This could be a projection effect, because the recombination line of the UC HII W51**e1**/**e2** region is at v ~ 56 km/s. For v = 55 to 63 km/s, the cloud is more extended to the north and in the east-west direction. These parts of the cloud belong to W51GMC according to Carpenter & Sanders (1994). The 56 and 62 km/s clouds are closely related, hence we cannot distinguish them from the channel maps easily. The peak position seen in the v = 54 km/s map is shifted slowly to the northwest and to the south (58 km/s map). One of the new peak regions of CO(4-3) is between W51**d** and **e**, and extended to its northeast. The other is the filament-like structure east of W51**c1** (see 58 km/s map). They form an arc-like structure (easily seen in the 60 km/s map). The dense region between **d** and **e** is a new feature in the CO(4-3) map. From the data of ^{13}CO(1-0) and 6 cm observations, there are no peaks towards this region. The structure east of **c1** is clearly shown in the 6cm and IR maps as a part of the curving structure associated with the W51**e** HII region (Fig. 4.7). The velocity of the recombination line H92α (Mehringer, 1994) of this region is 58 km/s, showing close relation between the W51**e** HII region and the W51GMC. This association has also been supposed by Genzel et al. (1982) and Arnal & Goss (1985).

In the channel maps above 64 km/s, the cloud shifts slowly to the south-west. It is the "high velocity stream" at 68 km/s, a filament-like stream along galactic latitude b = –00°22' (Carpenter & Sanders, 1994). It seems that the densest region of the cloud is located south out of the mapped region as seen in the channel maps. In our map, the cloud is fragmented and the peak of the cloud is between W51**d** and W51**b**. W51**b**, together with W51**c1**, is believed to be associated with the high velocity stream from the recombination line observations (v ~ 65 km/s. Arnal & Goss, 1985; Mehringer, 1994). Finally, from the channel maps, there is no strong evidence showing the outflowing gas around the W51**e1**/**e2** and W51**d** region.

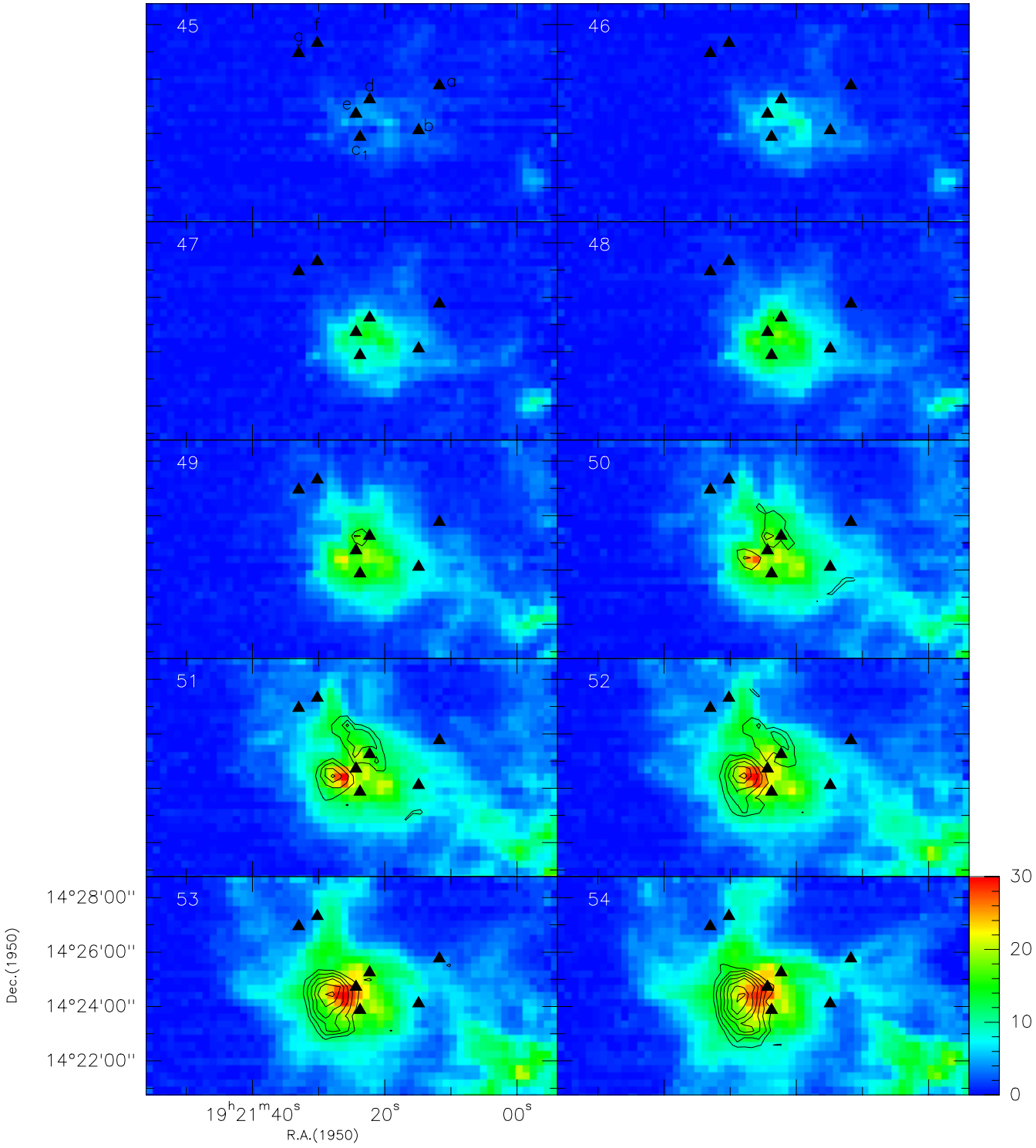

Fig. 4.8. Channel maps of CO(4−3) (color) and CI($^3P_1-^3P_0$) (contours) with a velocity interval of 1 km/s. Contour level from 2 to 5 by 0.5 K km/s. The triangles mark the positions of HII regions W51a−g (see Fig. 4.1).

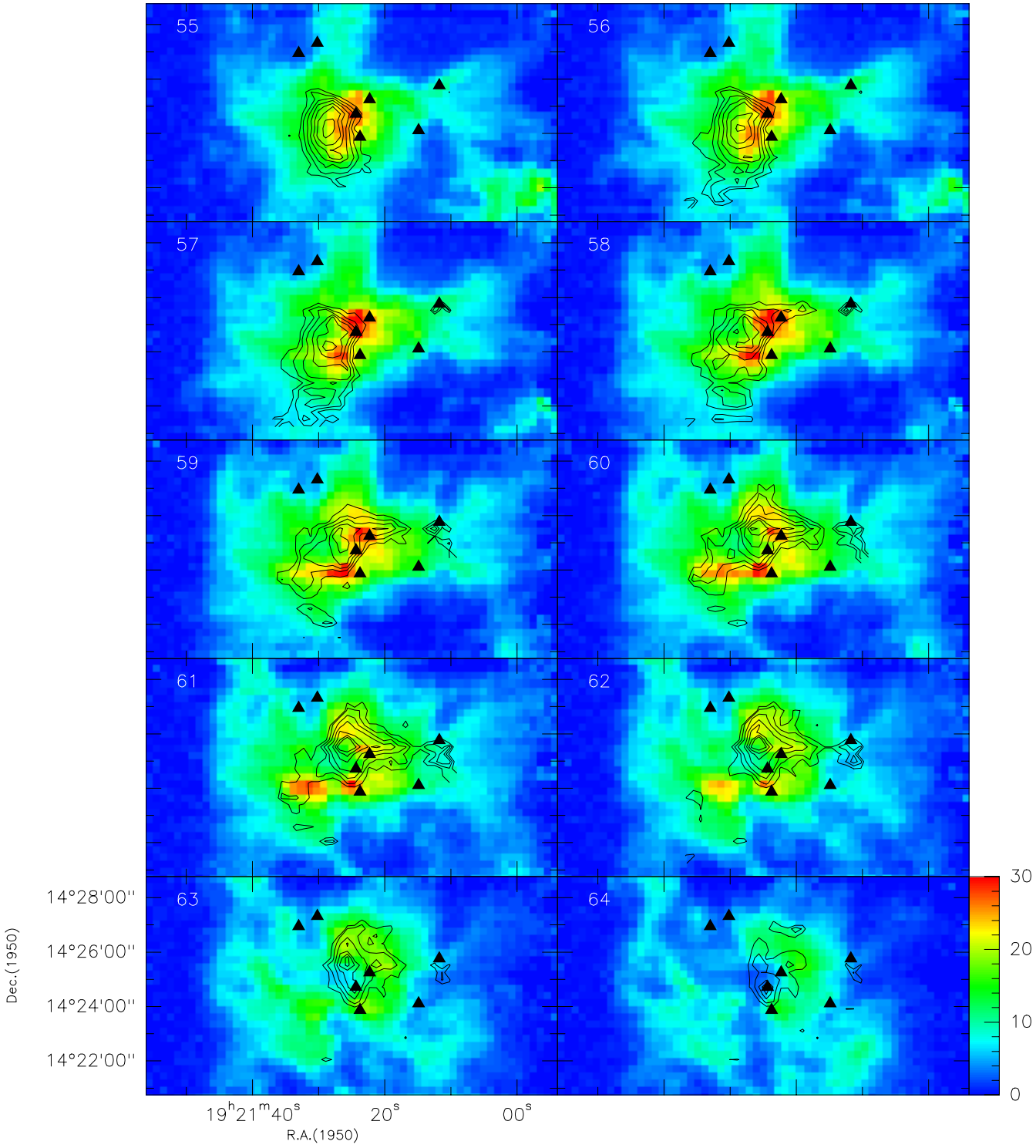

Fig. 4.8. (continued)

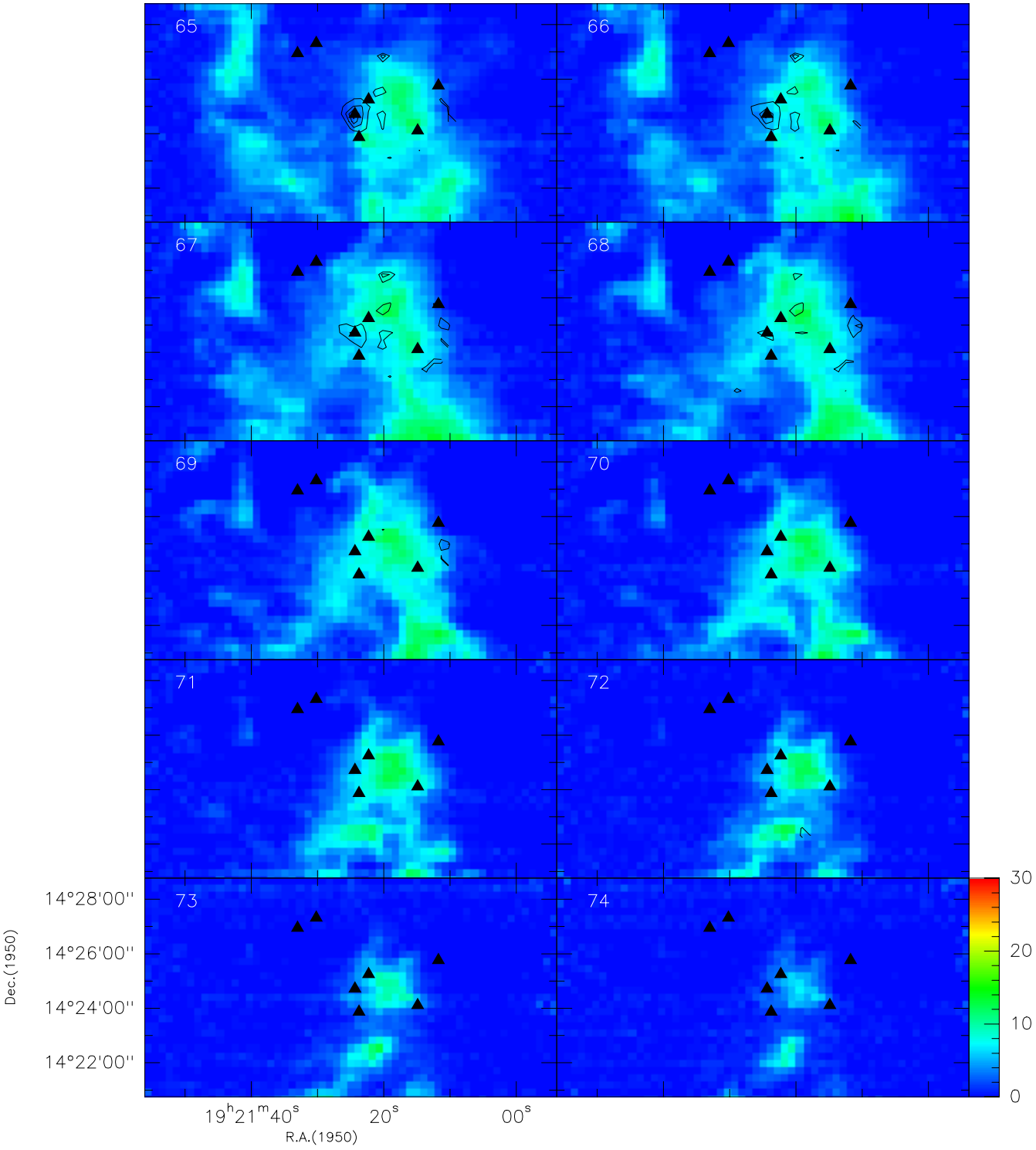

Fig. 4.8. (continued)

Having the same resolution as the ^{13}CO(1-0) data by Okumura et al. (16"), we expect the CO(4-3) emission to trace the warmer and maybe denser parts of the cloud. The difference in spatial distribution of the two observations should show the density and temperature difference towards these regions. We selected four velocities for comparing the channel maps of CO(4-3) and ^{13}CO(1-0) in Fig. 4.10. On large scales we find the resemblance of the two channel maps is striking, especially towards the edge of the cloud. This may imply that the emission in both lines has similar optical depth, and originates from similar parts of the cloud. We will check this point by calculating the total mass from CO(4-3) and ^{13}CO(1-0) in §4.4.1. On small scales, CO(4-3) and ^{13}CO(1-0) show different features towards the densest regions. The prominent regions in the CO(4-3) map are usually at the steep edges of the ^{13}CO(1-0) distribution in the v = 52, 58 and 62 km/s maps. It might be due to an optical depth effect. Only in the 68 km/s map, both peaks are in the region between W51**b** and **d**. From Fig.4.10, it seems that ^{13}CO(1-0) is more sensitive to the cold dense gas W51**e1**/**e2**, whereas CO(4-3) traces better the warm regions like W51**e** (IRS1) and its associated HII regions. We will revisit the channel maps again in §4.4.

We made CO(4-3) position-velocity maps (Fig. 4.9) and compared them with the ^{13}CO(1-0) data from Okumura et al. (2001). In the P-V map through W51**e** (Fig.4.9(c) and Fig.3(c) in Okumura et al.), a blending of the 56 and 61 km/s components around W51**e** is observed. The arc-like structure is shown at 60 km/s at the northern and sourthern sides. We did not include the whole 56 km/s cloud to the south, as it is shown in the ^{13}CO figure by Okumura et al. The 50 km/s cloud shown in the ^{13}CO data is not prominent in our maps. The 68 km/s cloud is better recognized and well separated in the P-V map of CO(4-3) from the south to the north. The morphological difference of the 50 and 68 km/s, the "high-velocity stream", clouds is probably due to the low temperature and/or the low density of the 50 km/s cloud and the high temperature and/or high density of the 68 km/s cloud.

The cut along the galactic longitude l = 49°29'30" goes through W51**d** and **e** (Fig. 4.9(b)). We cannot recognize the 50 km/s cloud, which is obvious in the ^{13}CO map (Fig.3(b) in Okumura et al., 2001). The cloud is more compact in CO(4-3) than in ^{13}CO(1-0). In the map we can identify the W51**e** region at 56-58 km/s (center-left of the map) and the arc-like structure east of W51**c1** as part of 61 km/s cloud in the map. This structure can be recognized at 56 km/s in the ^{13}CO map. The 68 km/s cloud is weak as in ^{13}CO map.

The major axis of the "high-velocity stream" is along galactic latitude b = –00°22'00". Therefore it is easy to recognize it in the P-V map along this axis as shown in Fig. 4.10(a). One can see in the figure that the end of the cloud at l = 49°29'30" coincides with the densest cores of the 56 and 61 km/s clouds. With the recombination line data, the W51**d** region is located at ~ 52 km/s to the left of the map, whereas the W51**b** region is at ~ 65 km/s is within the high velocity stream. In Fig. 4.9(d), a P-V map along the filament-like structure east of W51**c1** is plotted. The cut also goes through the W51**b**, **c1** and south of **e1**/**e2** regions. The star-forming regions W51**b**, **c1** are believed to be associated with the interaction between W51GMC and high velocity stream because the velocity of its recombination line is between 61 to 66 km/s. We see they are right at the narrow belt between the W51GMC and 68 km/s cloud in the map. The arc structure east of W51**c1** actually consists of two different clouds, one at 60 km/s and the other at 52 km/s. Together with the channel maps, it seems they are isolated.

In summary, we recognize at least four or five different clouds at 50, (53), 56, 61 km/s and the high-velocity stream towards the central region of W51. In the CO(4-3) maps, a new warm dense region at 58 km/s is detected between W51**d** and **e**. It seems that 53 km/s cloud is localized at the map center and peaks at the dense region W51**e1**/**e2**. The other three clouds are extendedly distributed. It seems that W51**e** (IRS1) region is the point where many different clouds coincide.

It is closely associated with the 56 and 61 km/s clouds revealed by the position-velocity maps. Whereas W51**d** (IRS2), another IR source and star forming region, is isolated. It seems that there is no association between the W51**d** HII region (v = 53 km/s) and the molecular cloud (v = 56 to 61 km/s) towards W51**d**. W51**b** and W51**c1** coincide with the interface between the W51GMC and high velocity stream both in velocity and geometry. From the the channel maps of ^{13}CO(1-0) and CO(4-3), on large scales, the maps of CO(4-3) are very similar to ^{13}CO(1-0). On small scales, the peaks of CO(4-3) are at the edge of ^{13}CO(1-0).

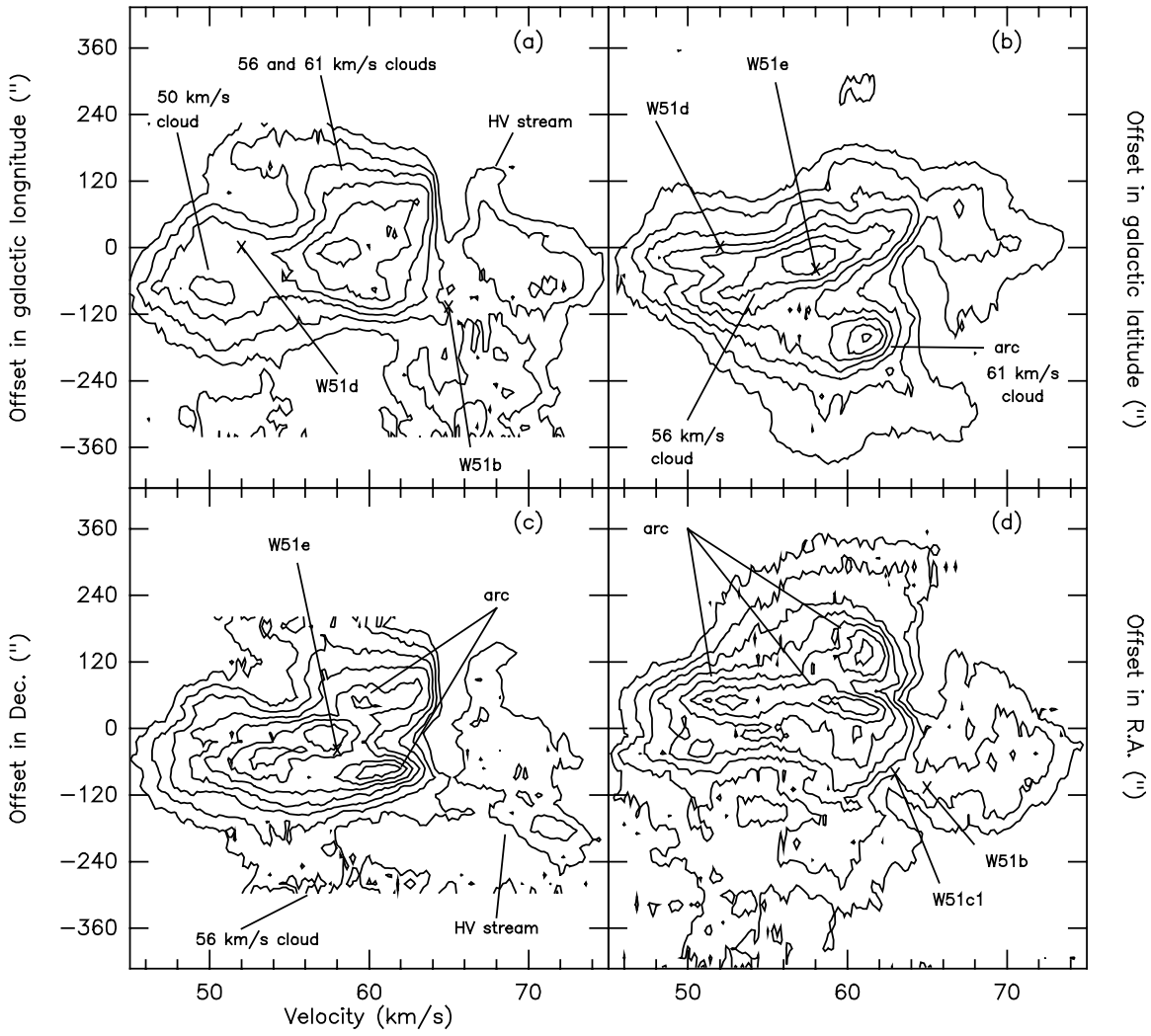

Fig. 4. 9. Position−velocity maps for CO(4−3) at (a) b = −00°22'00", (b) l = 49°29'30", (c) R.A.(1950) = 19:21:24.5, (d) Dec.(1950) = 14:24:00. Y−axis give the offset to W51d (l = 49°29'24", b = −00°22'8.4"). The contour intervals are 4 K, with 4 K as the lowest contour level (all in T_a^* scale).

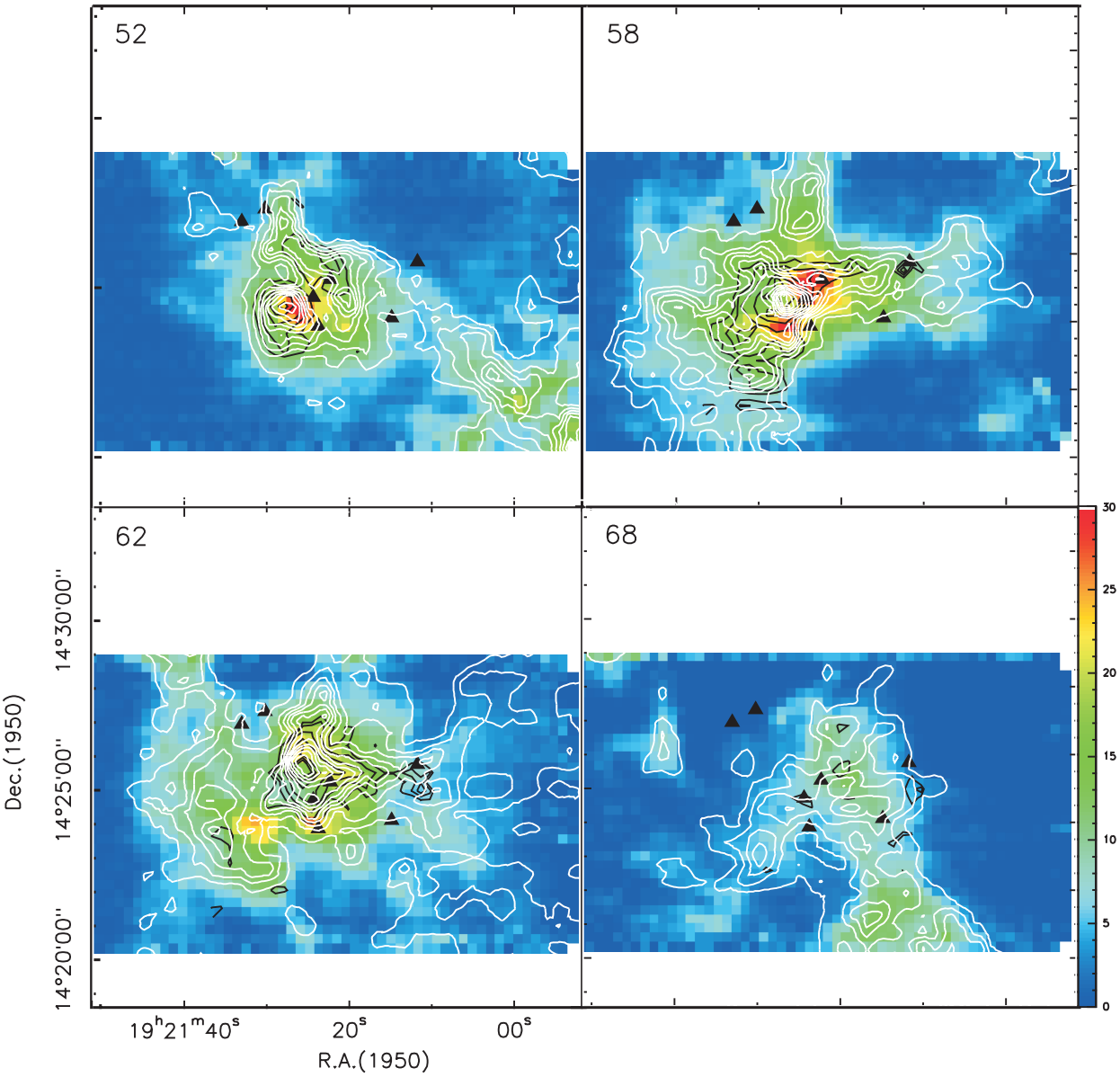

Fig. 4.10. Comparison of the velocity channel maps of CHAMP data (color: CO(4−3), black contour: CI, as in Fig. 4.8) and ^{13}CO(1−0) (white contours, the contour intervals are 5 K km/s, with lowest contour at 5 K km/s, Okumura et al., 2001).

4.3.2 CI($^3P_1$-$^3P_0$) emission

In Fig. 4.11, the CI data are superposed on the ^{13}CO(1-0) data. In Figs. 4.12 and 4.13, CI spectra are compared again with the continuum data from Mehringer and Sievers. The signal-to-noise ratio in the CI map is low as mentioned before (§4.2.2). The contour levels start from 50% of the peak value. The peak position of the CI emission is east of W51**e**, close to the W51**e1**/**e2** region.

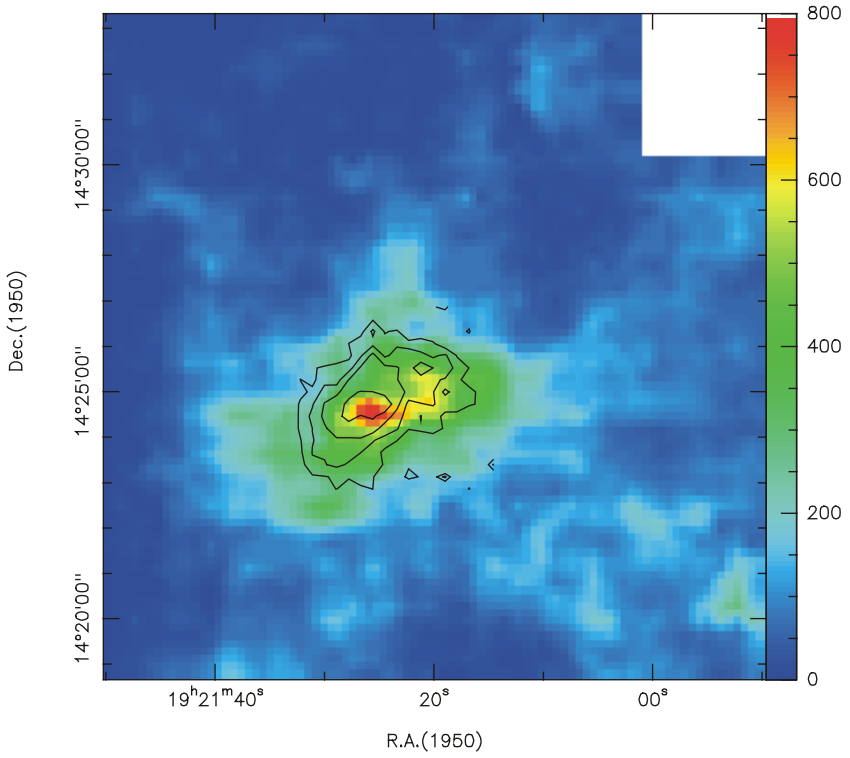

Fig.4.11. Color: $\int$Tmb(^{13}CO(1−0))dv from Okumura et al. (2001).
Contour: $\int$Ta*(CI($^3P_1-^3P_0$))dv as in fig. 4.3.
Contour level from 30 to 60 by 10 K kms^{-1}.

The CI, ^{13}CO(1-0) and 1.3 mm line distributions all peak at the W51**e1**/**e2** dense region. But outside of this region, the correlation between CI and the other two observations is low. Compared with the 6 cm data, the CI emission is constrained in the north-east direction of the W51**d**/**e** region. Towards W51**b** and **c1**, one sees no correlation between them.

Instead of taking the total integrated intensity map, the CI emission may be better understood by the velocity channel maps (Fig. 4.8(a)). Compared with CO(4-3), CI emission is often enhanced at the edges of the molecular clouds traced by the CO(4-3) line. At 51 km/s, the CI emission is strong at the northern and eastern edges of the 50 km/s cloud. Then the northern emission fades out but the eastern becomes prominent at the eastern edge of the dense core at 55 km/s. As the velocity increases, the region of strong emission shifts gradually to the north-east of W51**d** and **e**, to the south-eastern side of the newly discovered CO arc-like region. The projected morphology of the CI emission changes from elliptical to irregular shape. Now the area seems to follow well the edge defined by W51**d**, **e**, **d**, **c1** and the arc-like region (it is easily recognized in the 60 km/s map). The CI emission is constrained at its north-eastern side and no strong emission is found beyond it. In the higher velocity maps, the CI emission fades and one cannot find any structure. It is interesting to note that the CI emission concentrates on the W51**e** region at 65 km/s.

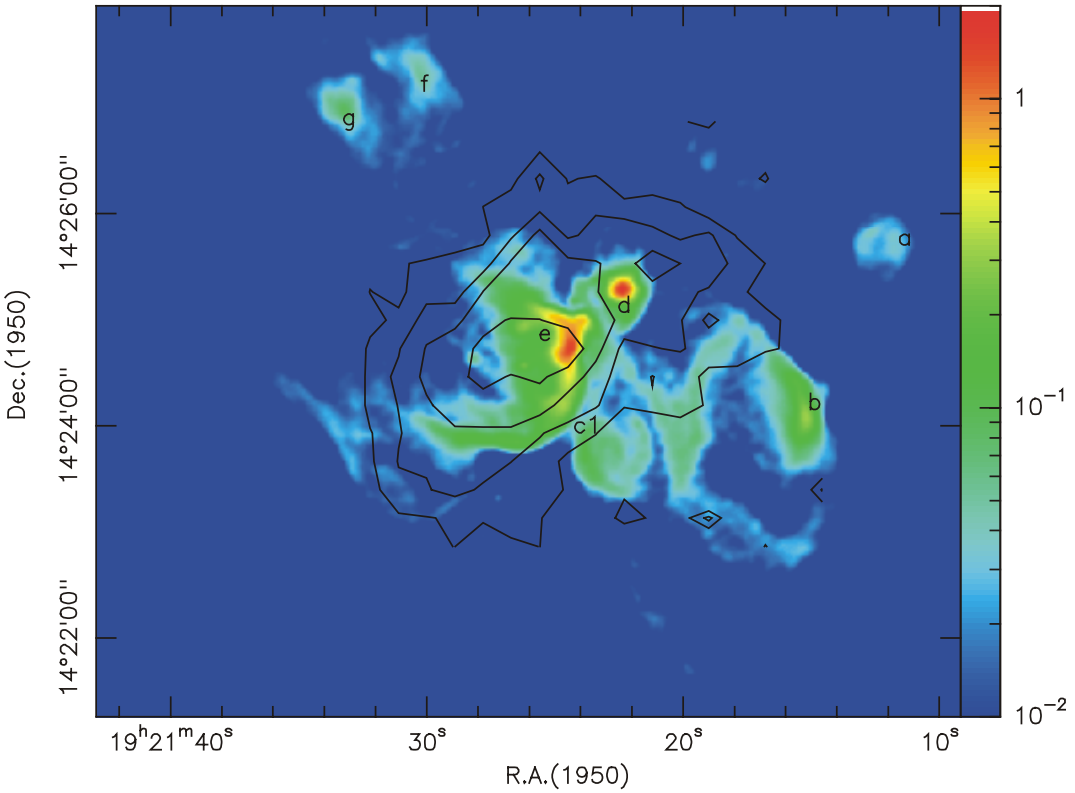

Fig.4.12. Color: 6cm observation from Mehringer in Jy/beam.
Contour: $\int Ta^*(CI(^3P_1-^3P_0))dv$ as in fig. 4.3,
contour level from 30 to 60 by 10 K km/s

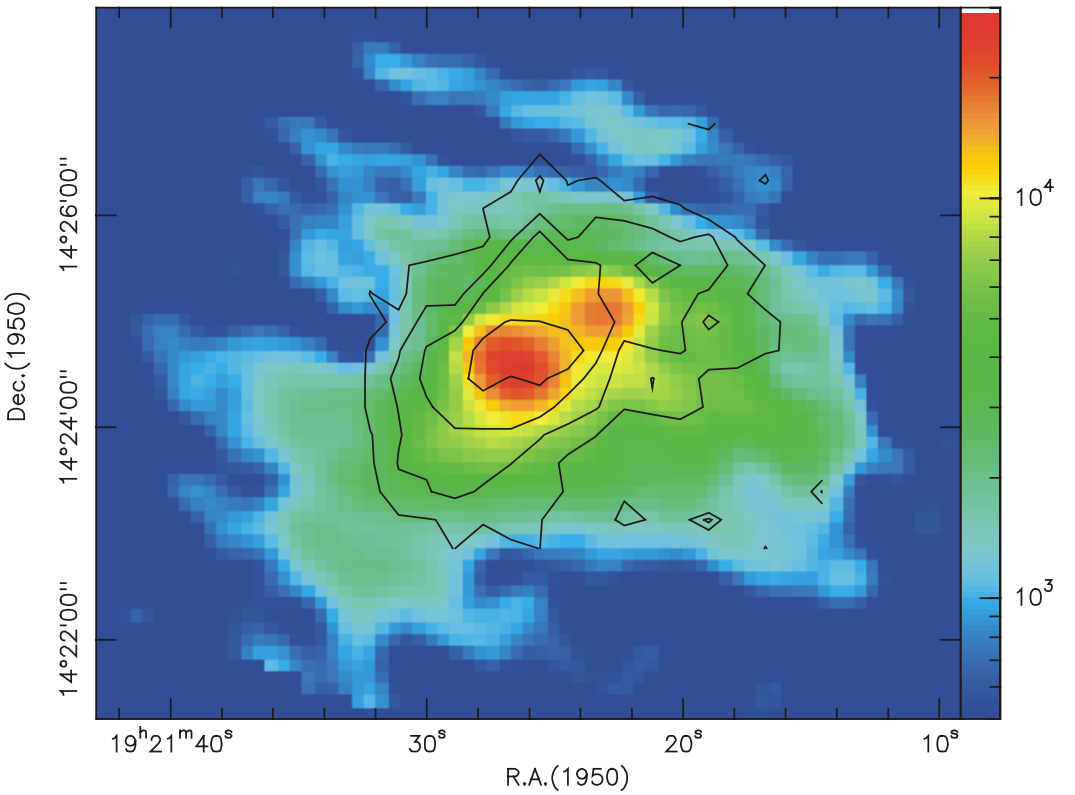

Fig.4.13. Color: 1.3mm data from Sievers in mJy/beam.
Contour: $\int Ta^*(CI(^3P_1-^3P_0))dv$ as in fig. 4.3,
Contour level as in Fig.4.12.

There is good agreement between CI and ^{13}CO(1-0) emission. When one compares the velocity channel maps of CI and ^{13}CO(1-0) (Fig.4.9) for v = 52, 58, and 62 km/s, their similarity towards the dense region is striking. There is almost no offset between the peaks in these figures. This phenomenon was already noted by other authors (§4.2). In the integrated intensity map (Fig.4.11) we failed to identify the similarity between them. It is maybe due to the complicated structure and implies that not all the molecular clouds towards this region are clumpy. From the channel maps, the peak intensity ratio of the two transitions $T_{mb}(^{13}CO(1\text{-}0)) / T_{mb}(CI)$ is ~ 6 for all three maps. It would be interesting to compare the spectra of the two transitions directly.

For v = 68 km/s, one cannot see any relation between CI and ^{13}CO(1-0) emission. There is not much spatial fine structure in the CI emission at this velocity. This is due to the low signal-to-noise ratio in the map. Higher signal-to-noise ratio measurements are required to investigate the correlation of the two transitions at this velocity in some detail.

The relation between HII region and CI emission seems to be restricted to the W51**e1**/**e2** region. The hydrogen recombination line (Mehringer, 1994) is seen at 53 to 58 km/s towards this region. Towards the W51**d** region, the velocity of the recombination line is at ~ 54 km/s, but we found no CI emission at 54 km/s. As for the higher velocities, the correlation between HII and CI emission is weak. In summary, except at the higher velocities, the CI emission is very similar to ^{13}CO(1-0).

4.4 Analysis

4.4.1 Mass estimation using CO(4-3) line

We start our estimation of molecular masses from the evaluation of the column density of CO. According to Rohlfs & Wilson (2000), for a optically-thin transition between two rotational levels J→J-1, the column density N(CO) is

$$N(CO) = \frac{3h}{8\pi^3\mu^2}\frac{Z}{J}e^{\frac{E_L}{kT_{ex}}}[1-e^{\frac{-h\nu_{J,J-1}}{kT_{ex}}}]^{-1}[J_\nu(T_{ex})-J_\nu(T_{bg})]^{-1}\int T_{MB}dv\,,$$

where Z is partition function, given by $Z = \Sigma N_i$ for all levels, N_i is the column density of level i. T_{ex} denotes the exitation temperature, T_{bg} stands for the cosmic microwave background temperature, $J_\nu(T)=\frac{h\nu}{k}(\exp(\frac{h\nu}{kT})-1)^{-1}$, μ is electric dipole moment of CO (0.112 debye), E_L is the energy state of the lower level, and T_{MB} is the main beam brightness temperature. All the parameters of CO used here were taken from Lovas & Krupenie (1974) and Pickett et al. (2000).

We can then estimate the total mass of the molecular cloud M_{cloud} if the molecular hydrogen contains most of the mass and the contribution of helium is neglectable,

$$M_{cloud} = X\cdot N(CO)\cdot m_{H_2}\cdot D^2\theta^2\,,$$

where $X=[H_2]/[CO]$, is the ratio of number of molecular hydrogen to carbon monoxide molecules. m_{H2} is the mass of an individual hydrogen molecule. D is the distance to the source, and θ is the size of the source in radius. For W51 we assume $X\sim10^4$ (Dickman, 1978).

For the CO(4-3) line measured by CHAMP at 461 GHz, the optical depth is unknown because the isotopic lines are hard to observe from ground-based telescopes. Only low resolution data (beamwidth ~ 5') from a balloon-borne telescope is available (Olofsson et al., 1998).

Therefore first we assume it is optically thin in order to derive a lower limit for the mass, which is likely a gross underestimate. If we deal only with the central part of W51 as shown in Fig. 4.3 and neglect the clouds at the south-western edge of the map, in the optically-thin case the total mass of the cloud is around 4×10^3 $M_\odot$, assuming T_{ex}= 50 K. The total mass of the cloud with different T_{ex} is shown in Table 4.3.

On the other hand, we also estimate the total mass from ^{13}CO(1-0) which was obtained by Okumura et al. (2001) with the same procedure. Here we include the same part of the cloud as in the CO(4-3) estimate, and [^{12}CO]/[^{13}CO] ~ 50 is assumed in W51 (Wilson & Rood, 1994). For T_{ex} = 50 K, $M_{cloud} \sim 7.9 \times 10^5$ $M_\odot$, showing that CO(4-3) has an optcal depth of at least 100.

Table 4.3. Molecular masses of W51 obtained from CO(4-3) (lower limits) and ^{13}CO(1-0) with different excitation temperature.

T_{ex} (K)	M_{cloud} (CO(4-3))	M_{cloud} (^{13}CO(1-0))
25	6.4×10^3	4.5×10^5
50	4×10^3	7.9×10^5
75	4.2×10^3	1.1×10^6

From the dust observation, which is optically-thin, Schloerb et al. (1987) and Jaffe et al. (1984) estimate the total mass to be 5×10^4 $M_\odot$ at 1300 μm and 10^5 $M_\odot$ at 400 μm respectively. The dust temperature is estimated to be 45-55 K by Schloerb and 35 K by Jaffe. Sievers et al. (1991) estimate the total mass in this region to be 1.7×10^5 or 6.6×10^4 $M_\odot$ with dust temperature of 20 K or 57 K from their mm wavelength observations.

From large scale (83 × 114 pc) ^{12}CO(1-0) and ^{13}CO(1-0) observations (Carpenter & Sanders, 1998), they estimated the total mass to be 1.2×10^6 $M_\odot$ assuming ^{13}CO/H_2 ratio of 1.5×10^{-6} and lower temperature T_{ex}=10 K. Compared with their estimates, the total mass of W51 from CO(4-3) is obviously too low. The opacity of the CO(4-3) line is likely high and thus traces only the outer part of the molecular clouds, while ^{13}CO(1-0) from Okumura et al. gets closer to the optically thin case.

To investigate the excitation condition, we perform the LVG calculations using the CO(4-3) and ^{13}CO(3-2) (Wang et al., 1994. Beamwidth ~ 22") lines towards the W51**d** dense region. The main-beam brightness temperautre T_{mb} is 33 K on W51**d**. In Fig. 4.14 we plot the intensity ratio (T_{mb}(CO(4-3))/T_{mb}(^{13}CO(3-2)) and line intensity as function of column density per linewidth, N(CO)/Δv, and kinetic temperature, T_k, with the molecular hydrogen density n(H_2) = 10^4 and 10^5 for the v = 59 km/s component. In Fig. 4.14 we see T_k is sensitive to the line ratio, therefore we plot also the 10% error for the intensity ratio in the figures. In this density range, T_k is between 65 to 80 K. N(^{12}CO) is better constrained between 1 and 2.5×10^{19} cm^{-2} by applying Δv ~ 8 km/s (Table 4.1). The opacity of CO(4-3) is 80 and 45 for n(H_2) = 10^4 and 10^5 cm^{-3}, respectively. It confirms the high optical depth of CO(4-3).

Therefore we conclude that the opacity of the CO(4-3) line is large, whereas the opacity of the ^{13}CO(1-0) line is small or moderate. Therefore towards the dense regions W51**d**, W51**e** and W51**e1**/**e2**, the morphologies of the two transitions are different. On the other hand, the high opacity in the CO(4-3) emission may reduce slightly the critical density. Hence the high opacity of the CO(4-3) transition may explain the similarity between the CO(4-3) and ^{13}CO(1-0) in terms of their spatial distribution towards the outer regions where the density is lower.

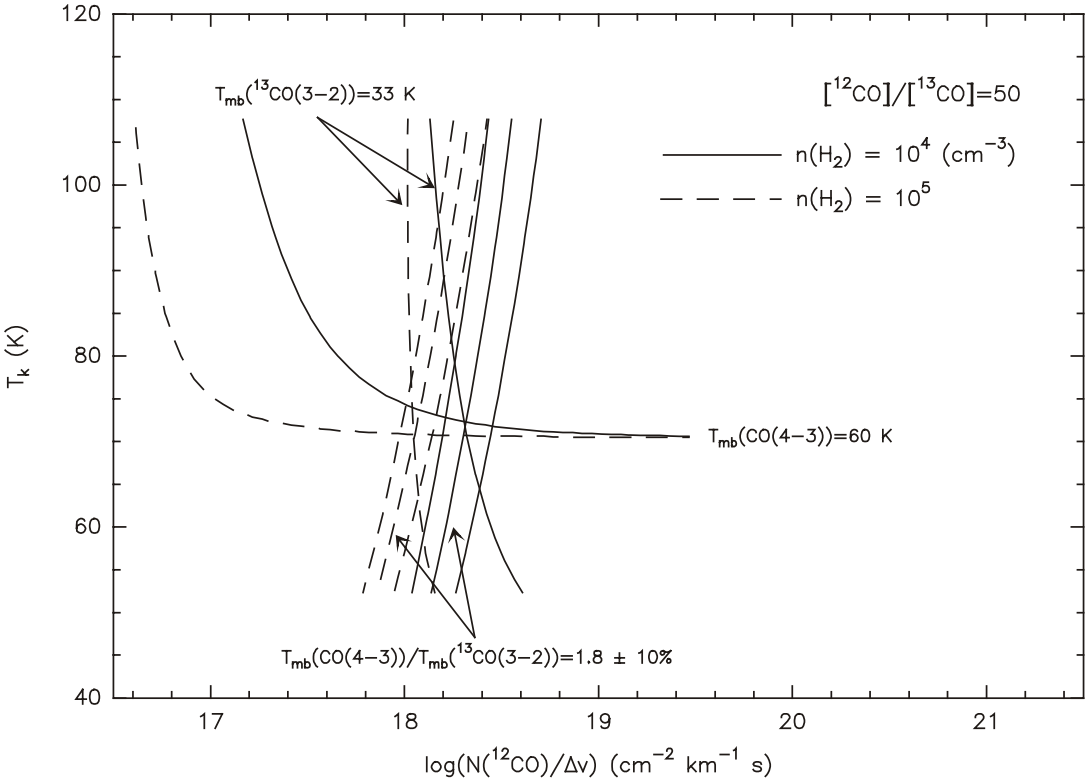

Fig.4.14. LVG solution for the W51d dense region. The ^{12}CO to ^{13}CO abundance ratio is assumed to be 50. T_k is the kinetic temperature, N(CO) is CO column density, and Δv is the linewidth. Two different molecular hydrogen densities are calculated, n(H_2) = 10^4 cm^{-3} (solid line) and n(H_2) = 10^5 cm^{-3} (dashed line). The three parallel curves represent the line ratio T_{mb}(CO(4-3))/T_{mb}(^{13}CO(3-2)) = 1.62, 1.80, 1.98, respectively. T_k is sensitive to the line ratio.

In order to search for the outflowing gas, we calculated the masses for the high velocity gas at 45-50 and 70-75 km/s. The momentum and kinetic energy of the gas are also calculated. They are the lower limits because the optical depth and the projection angle are unknown. The opacity at the high velocity wings is likely lower, because the spatial distribution of the CO(4-3) and ^{13}CO(1-0) emissions are similar both on large and small scales (Fig.4.9). The results by assuming T_{ex} = 50 K is listed in Table 4.4.

Table 4.4. Mass, momentum and kinetic energy of the outflowing gas from CO(4-3) data with T_{ex} = 50 K. The rest velocity of the cloud is assumed to be 60 km/s.

Velocity Range (km/s)	Total Mass ($M_\odot$)	Momentum* ($M_\odot$ km/s)	Kinetic Energy* (ergs)
45 – 50	4.2×10^2	5.6×10^3	6.6×10^{47}
70 – 75	2.6×10^2	3.8×10^3	4.4×10^{47}

*Relative to 60 km/s.

4.4.2 Column density of atomic carbon

The column density of atomic carbon may be determined by assuming that the CI emission is optically thin (Phillips & Huggins 1981):

$$N(CI) = 2\times10^{15}\, e^{E_1/kT_{ex}}\,(1+3e^{-E_1/kT_{ex}}+5e^{-E_2/kT_{ex}})\int T_{MB}dv\ ,$$

where E_1~ 23.5 K, E_2~ 62.5 K, and T_{ex} is the excitation temperature. According to this equation, the column density of carbon does not depend much on the excitation temperature. The results at selected positions are listed in Table 4.5. N(CI) is between 5×10^{17} and 2×10^{18}. With the aid of the optically-thin ^{13}CO(1-0) line, we tried to derive the relative abundance ratio N(CI)/N(CO) with T_{ex} = 50 K. The abundance ratio of atomic carbon to ^{12}CO is 0.02 - 0.05, if ^{12}CO/^{13}CO = 40 (§4.4.1). This corresponds to an atomic carbon abundance of $[CI]/[H_2] = 2 - 5\times10^{-6}$ at these positions if $^{12}CO/H_2 = 10^{-4}$. Compared with the result from CI($^3P_2$-$^3P_1$), N(CI)/N(CO) ~ 0.1 (Genzel et al., 1988), our abundance is low.

With the equations, the integrated intensities of ^{13}CO(1-0), CI and CO(4-3) for the velocity range of 45 to 75 km/s are plotted in Fig. 4.15 through the W51**e** region by assuming T_{ex} = 50 K. CI and ^{13}CO(1-0) show weak correlations along the cross section. The column density of CI is much enhanced at the eastern side. The peak of N(CO(4-3)) is at the local minimum of CI and ^{13}CO(1-0). One cannot recognize the clear CI/CO relation predicted by the PDR model (Fig. 4.1), probably because the column density shown here is a summation of several different unrelated clouds, and not all of the clouds on the line of sight are in the PDRs.

If we follow the prediction from the PDR model by Hollenbach et al. (1991) (§4.1.2), the observed high CI column density should arise from a geometrical effect i.e. the presence of multi PDRs or the tilting of PDRs along the line of sight. Since we have figured out that there are four different parts in the CI data with different velocities and spatial distribution (§4.3.2), the results can be applied here. With the Gaussian decomposition results from Table 4.1, we calculated the column density for each component at the selected positions again. The results are listed in Table 4.5. Since CO(4-3) is optically thick and we have no spectra for ^{13}CO(1-0), we cannot estimate the atomic carbon abundance for each component.

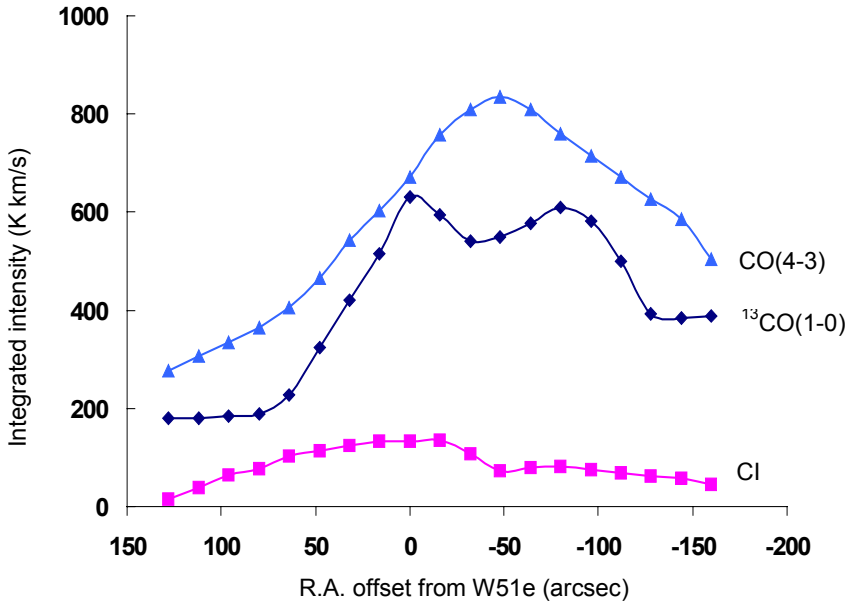

Fig. 4.15. Comparison of the integrated intensity (v = 45 to 75 km/s, in T_{mb} scale) of CO(4-3), ^{13}CO(1-0) and CI along Dec.(1950) = 14°24'43", by assuming T_{ex} = 50 K. The cross section passes W51**e**. The peak positions of ^{13}CO(1-0) and CI are near the W51**e** region, whereas the peak of CO(4-3) is to the west.

Table 4.5. Atomic carbon column density and abundance at selected positions.

Position	Velocity (km/s)	N(C)[a] ($\times 10^{17}$ cm^{-2})	N(^{13}CO)[b] ($\times 10^{17}$ cm^{-2})	N(C)/N(^{12}CO)[c] (10^{-2})
W51b (-108,-68)	Total	6.4	5.9	2.71
	48.9	3.6		
	60.9	1.4		
	68.0	1.6		
W51c1 (21,-83)	Total	11.0	10.5	2.62
	53.5	5.0		
	65.3	3.9		
W51d (0,0)	Total	15.4	12.9	2.98
	50.5	4.4		
	60.7	7.3		
	68.1	2.6		
W51e (30,-32)	Total	18.9	14.2	3.32
	51.5	2.2		
	59.9	12.3		
	66.5	3.4		
W51e1/e2	Total	18.4	21.8	2.18
(57,-34)	54.4	8.6		
	61.1	7.2		
	68.3	2.5		
(50,50)	Total	10.3	6.6	3.91
	51.4	3.2		
	61.5	6.6		
	68.1	0.9		
(-50,50)	Total	6.6	6.1	2.64
	50.7	1.1		
	62.9	5.6		
(-50,-50)	Total	7.4	14.7	1.28
	49.8	2.6		
	64.2	4.8		
(0,100)	Total	6.4	6.5	2.55
	50.6	0.9		
	62.2	4.1		
(-100,0)	Total	7.5	11.2	1.67
	49.9	1.8		
	60.5	4.2		
	68.3	1.4		
(150,0)	Total	8.3	4.0	5.28
	52.9	1.1		
	59.4	5.9		
(100,-50)	Total	16.1	10.5	3.85
	55.6	13.6		
	68.3	1.6		
(100,-150)	Total	9.4	7.6	3.21
	55.2	4.7		
	61.4	2.1		
	68.5	1.9		
(150,-100)	Total	8.0	7.9	2.53
	57.7	7.8		
	67.8	0.7		
(150,-200)	Total	6.9	3.5	4.92
	56.4	3.1		
	61.2	1.7		
	69.2	1.8		

a) T_{ex} = 50 K.

b) from ^{13}CO(1-0) data by Okumura et al. (2001) with T_{ex} = 50 K.

c) assumed N(^{12}CO)/N(^{13}CO)=40.

The column density in each velocity component is between 0.7 and 13.6 $\times 10^{17}$ cm^{-2} with an average column density of 3.8 ± 2.9 $\times 10^{17}$ cm^{-2}. This average is twice of the column density predicted by the PDR model. Towards the central region and its north-east region (i.e., W51**d**, **e**, **c1**, (100,-50), (50,50)), N(CI) can be as large as 1.5 $\times 10^{18}$ cm^{-2} at the peak position. This CI column density is an order higher than the prediction of standard PDR model by Hollenbach et al. (1991). Other PDR models like the inhomogeneous model (Spaans, 1996) have to be introduced to explain the high column density. On the other hand, the column densities at the south-western and far eastern sides, and the components related to the 68 km/s cloud are close to the prediction of the parallel layer PDR model.

4.4.3 The origin of the CI emission

We detected CI emission at all positions. Cosmic rays in a clumpy cloud structure should indeed produce a certain amount of atomic carbon in the region. Since there are embedded clusters of OB stars towards the central region around W51**d**/**e** (Okumura et al., 2000), the embedded stars should account for the enhanced CI emission towards the dense cores like W51**e1**/**e2** and W51**d** with large visual extinction. If all the atomic carbon is produced in the PDRs, the complicated and clumpy structure of W51 should be introduced to explain the high column density of atomic carbon. It is easy to imagine that towards the dense region there are several PDRs from clouds at slightly different velocities along the line of sight. The gaps between the clouds permit UV photons to penetrate and illuminate each cloud even at the positions with very high CO column density.

However, as calculated in Table 4.5, the column density of atomic carbon can be as high as 2 $\times$ 10^{18} cm^{-2}. The atomic carbon column density is still high in each component after a rough line decomposition. We assume that the N(C)/N(CO) ratio can approximately express a ratio of the surface area relative to the volume of the clumps. This ratio is ~ 0.03 at the central region. Therefore, the clump size is of the order of 0.01 pc if the clump density is 10^4 to 10^5 cm^{-3}. This is beyond the resolution of our observation. Furthermore, if the molecular clouds towards the central region are as clumpy as we estimate, one would expect a better relation between the integrated intensity of ^{13}CO(1-0) and CI. Hence, the atomic carbon originating from the PDR can explain the CI column density outside the central region, but is not a very persuading explanation for the high column density towards the central region. For a better understanding, higher resolution measurements are needed.

Therefore it is worth to consider the non-PDR origin of atomic carbon. The time-dependent chemical model and the models with bi-stable solution may also account for high CI/CO ratio in the cloud cores with high A_v (§4.1.3). Since W51 is a massive star-forming region triggered by cloud collisions (§4.4.5), one would expect that some of the clouds are probably chemically young, especially at the eastern side, where more stars are forming. At this side of the cloud, the CI/CO ratio is also generally higher. Therefore we believe the time-dependent model should account for the atomic carbon deep inside the dense cores and explain the good correlation between CI and CO.

4.4.4 The new arc-like feature in the CO(4-3) map

The arc-like feature is seen along the western and southern edge of the W51**e1**/**e2** region. As revealed in the ^{13}CO(1-0) and 1.3 mm maps, W51**e1**/**e2** is probably the densest region. One would expect that the peak of CO(4-3) locates at the W51**e1**/**e2** region, if the transition is

optically thin. As calculated in §4.4.1, the opacity of the CO(4-3) transition would be very large. It is very likely that the arc feature comes from an optical depth effect. When the opacity is large, the peak intensities at the central region reflect the excitation temperature of the gas at the surface. The peak in the integrated intensity map would appear along the edge of the dense region.

Thus, the arc feature identified in the velocity channel maps of CO(4-3) (Fig. 4.8) is probably not a real structure, but traces the edge of the warm dense clouds. If this is true, the optical depth effect can also explain the offset of the peak position in the total integrated intensity map of CO(4-3) from the W51**e1**/**e2** region (Table 4.2 and Fig.4.14) and the difference of the velocity channel maps of CO(4-3) and ^{13}CO(1-0) on small scales.

4.4.5 Collision between the clouds ?

Arnal & Goss (1985), Carpenter & Sanders (1994), and Okumura et al. (2001) suggested that there are interactions between the 56 and 60 km/s molecular clouds within the W51 giant molecular cloud and between the W51 and 68 km/s clouds. The first suggestion was proposed by observing the coincidence of the area of massive star-formation and the cloud interface at W51**e** (IRS1) (Okumura et al.). And the second one was proposed by the positional coincidence of the broken filament structure in the 68 km/s stream with the W51 cloud center on a large scale structure, and considering the scarcity of embedded O stars together with the dense distribution of O stars at the tip of the 68 km/s ridge regions (Okumura et al., 2000; Carpenter & Sanders).

With the CO(4-3) maps we also observe phenomena supporting the collision scenario obtained above. One can see them in the velocity channel and position-velocity maps discussed in §4.3.1. With a highly saturated transition observed with similar resolution as ^{13}CO(1-0) we cannot provide new evidence supporting the collision scenario between the clouds. We also see no clue to suggest the collision between the 50 and 56 km/s clouds. The interface of these two clouds is located around the W51**e** region, but the velocity of the W51**e** cloud is ~ 58 km/s. The W51**d** region has similar velocity, but the locations do not match.

In order to verify the assumptions of cloud collisions, observations tracing the shock wave e.g. SiO should be carried out. Measurements of the ages of the embedded O-type stars towards the interface region should also be performed. If the massive stars were formed in a single event, it would be a strong evidence for the scenario.

4.5 Conclusion

The CO(4-3) and CI($^3P_1$-$^3P_0$) transitions were observed towards the W51 region with CHAMP at the CSO. We separated the complicated velocity structure into at least four components. The relation between the individual clouds is discussed. On large scales, we find similar morphologies for CO(4-3) and ^{13}CO(1-0). On small scales, there is a close relation between CI and ^{13}CO(1-0) emission. The total integrated intensities of the CI and ^{13}CO(1-0) lines is not as strikingly similar as in many well-known cases like the Orion Bar, M17 or Oph A. The ratio of N(C)/N(CO) is 0.02 to 0.07 in all selected positions towards W51 and the ratio is similar to other massive star-forming regions. This ratio is low compared with other observations. It might be because there are several independent clouds along the line of sight and one may just sample several independent layers in one beam. This geometrical explanation might imply that the molecular clouds towards this region are inhomogeneous. Therefore not all PDRs show close relation

between CI and ^{13}CO(1-0). It is, however, hard to make any concrete conclusion from the CI observations alone. ^{13}CO(2-1) observations at IRAM 30 m telescope with similar resolution to CHAMP provide very good chance to fulfill a complete data interpretation.

The CO(4-3) line is highly optically thick and probably reveal the excitation temperature of the clouds. Towards W51**d**, the kinetic temperature is constrained between 65 to 80 K, and N(CO) is between 1 to 2.5 $\times$ 10^{19} cm^{-2} using LVG with CO(4-3) and ^{13}CO(3-2) data for n(H_2) = 10^4 to 10^5 cm^{-3}. We found a new feature in CO(4-3) near W51**d**/**e**. It is located at the edge of the dense region and very likely caused by an optical depth effect. The CI emission is intense towards the dense cloud. It is closely related to ^{13}CO(1-0). Strong CI emission is found even deep in the cloud cores, and it cannot be explained by a single parallel layer PDR model after considering the complicated structure of the region. The cluster of embedded OB stars may be the source of strong UV radiation towards this region. Towards the central region and the north-eastern side of the cloud, PDR models with clumpy structure and time-dependent chemistry are needed to explain the observed CI column density. Higher resolution measurements are needed to check the clump size of the cloud. At the western side of the cloud, the CI emission is evenly distributed and the column density is in good agreement with the prediction of the parallel layer PDR model by Hollenbach et al. (1991). For further investigation of the CI emission, ^{13}CO(2-1) data is urgently needed.

To summarize, the comparison of the CO(4-3), CI and ^{13}CO(1-0) lines shows very complicated and interesting structure in the region. Applying PDR models is worth a try later to investigate the molecular clouds. But even if we can have more data with similar resolution to give more constraints to the model, we have to investigate the structure thoroughly before applying the models. Due to the complicated kinematics in the region, one has to interpret the data very carefully.

References

Arnal, E. M., Goss, W. M., 1985, A&A, 145, 369.

Burton, W. B., Shane, W. W., in "The Spiral Structure of our Galaxy", Proceedings from 38th IAU Symposium Edited by Wilhelm Becker and Georgios Ioannou Kontopoulos. International Astronomical Union. Symposium no. 38, Dordrecht, Reidel, p. 397.

Carpenter, J. M., Sanders, D.B., 1998, AJ, 116, 1856.

Dickman, R.L., 1978, ApJS, 37, 407.

Flower, D. R., Le Bourlot, J., Pineau des Forêts, G., Roueff, E., 1994, A&A, 282, 225.

Genzel, R., Downes, D., 1977, A&AS, 30, 145.

Genzel, R., Downes, D., Schneps, M.H., Reid, M.J., Moran, J.M., Kogan, L.R., Kostenki, V.I., Matveyenko L.I., Rönnäng B., 1981, ApJ, 247, 1039.

Genzel, R., Becklin, E.E., Wynn-Williams, C.G., Moran, J.M., Reid, M.J., Jaffe, D.T., 1982, ApJ, 255, 527.

Genzel, R., Harris, A.I., Stutzki, J., Jaffe, D.T., 1988, ApJ, 332, 1049.

Güsten, R., Ediss, G., Gueth, F., Gundlach, K., Hauschildt, H., Kasemann, C., Klein, T,, Kooi, J., Korn, A., Kramer, I., Leduc, R., Mattes, H., Meyer, K., Perchtold, E., Pilz, M., Sachert, R., Scherschel, M., Schilke, P., Schneider, G., Schraml, J., Skaley, D., Stark, R., Wetzker, W., Wiedenhöver, H., Wiedenhöver, W., Wongsowijoto, S., Wyrowski, F., 1998, Proc. SPIE Vol. 3357, p. 167, Ed. Thomas G. Phillips.

Hollenbach, D. J., Takahashi, T., Tielens, A. G. G. M., 1991, ApJ, 377, 192.

Hollenbach, D. J., Tielens, A. G. G. M., 1997, Annu. Rev. Astron., Astrophys., 35, 179.

Ikeda, M., Oka, T., Tatematsu, K., Sekimoto, Y., Yamamoto, S., 2002, ApJS, 139, 467.

Jaffe, D. T., Becklin, E. E., Hilderbrand, R. H., 1984, ApJ, 279, L51.

Jaffe, D. T., Harris, A. I., Genzel, R., 1987, ApJ, 316, 231.

Keene, J., Blake, G.A., Phillips, T.G., Huggins, P.J., Beichman, C.A., 1985, ApJ, 299, 967.

Keene, J., Lis, D.C., Phillips, T.G., Schilke, P., in *Molecules in Astrophysics: Probes and Processes*: abstract book, IAU symposium 178: 1-5 July 1996, Leiden, The Netherlands. Edited by Ewine Fleur van Dishoeck, pp. 129.

Koo, B.-C., 1997, ApJSS, 108, 489.

Kundu, M. R., Velusamy, T., 1967, Ann. Astrophys., 30, 59.

Le Bourlot, J., Pineau des Forêts, G., Roueff, E., 1993, ApJ, 416, L87.

Lee, H.-H., Herbst, E., Pineau des Forêts, G., Roueff, E., Le Bourlot, J., 1996, A&A, 311, 690.

Lovas, F.A., Krupenie, P.H., 1974, JPC Ref. Data, Vol.3, no.1, 245.

Maezawa, H., Ikeda, M., Ito, T., Saito, G., Sekimoto, Y., Yamamoto, S., Tatematsu, K., Arikawa, Y., Aso, Y., Noguchi, T., Shi, S.-C., Miyazawa, K., Saito, S., Ozeki, H., Fujiwara, H., Ohishi, M., Inatani, J., 1999, ApJ, 524, L129.

Martin, A.H.M., 1972, MNRAS, 33, 289.

Mehlinger, D.M., 1994, ApJS., 91, 713.

Meixner, M., Tielens, A. G. G. M., 1993, ApJ, 405, 216.

Meixner, M., Tielens, A. G. G. M., 1995, ApJ, 446, 907.

Okumura, S.-I., Mori, A., Nishihara, E., Watanabe, E., 2000, ApJ, 543, 799.

Okumura, S.-I., Miyawaki, R., Sorai, K., Yamashita, T., Hasegawa, T., 2001, PASJ, 53, 793.

Olofsson, G., Pagani, L., Tauber, J., Febvre, P., Deschamps, A., Encrenaz, P., Florén, H.-G., George, S., Lecomte, B., Ljung, B., Nordh, L., Pardo, J. R., Peron, I., Sjökvist, M., Stegner, K., Stenmark, L., Ullberg, C., 1998, A&A, 338, L81.

Phillips, T.G., Huggins, P.J., 1981, ApJ, 251, 533.

Pickett, H.M., Poynter, R.L., Cohen, E.A., Delitsky, M.L., Pearson, J.C., Müller, H.S.P. 2000, "Submillimeter, Millimeter, and Microwave Spectral Line Catalog".
Pineau des Forêts, Roueff, E., Flower, D. R., 1992, MNRAS, 258, 45.
Plume, R., Jaffe, D.T., Keene, J., 1994, ApJ, 425, L49.
Plume, R., Jaffe D.T., Tatematsu, K., Evans II, N.J., 1999, ApJ, 512, 768.
Rohlfs, K., Wilson, T. L., 2000, "*Tools of Radio Astornomy*", 3 Ed. , Springer Verlag.
Rudolph, A., Welch, W., Palmer, P., Dubrulle, B., 1990, ApJ, 363, 528.
Schilke, P., Keene, J., Le Bourlot, J., Pineau des Forêts, G., Roueff, E., 1995, A&A, 294, L17.
Schloerb, F.P., Snell, R.L, Schwarz, P.R., 1987, ApJ, 319, 426.
Schneps, M.H., Lane, A.P., Downes, D., Moran, J.M., Genzel, R., Reid, M.J., 1981, ApJ, 249, 124.
Scott, P. E., 1978, MNRAS, 183, 435.
Sievers, A.W., Mezger, P.G., Gordon, M.A., Kreysa, E., Haslam, C.G.T., Lemke, R., 1991, A&A, 251, 231.
Spaans, M., 1996, A&A, 307, 271.
Störzer, H., Stutzki, J., Sternberg, A., 1997, A&A, 323, L13.
Stutzki, J., Stacey, G.J., Genzel, R., Harris, A.I., Jaffe, D.T., Lugten, J.B., 1988, ApJ, 332, 379.
Tauber, J.A., Lis, D.C., Keene, J., Schilke, P., Büttgenbach, T.H., A&A, 297, 567, 1995.
Tielens, A.G.G.M., Hollenbach, D., 1985, ApJ, 291, 722.
Ulich, B. L., Haas, R. W., 1976, APSS, 30, 247.
Wang, Y., Jaffe, D., Graf, U. U., Evans II, N. J., 1994, ApJS, 95, 503.
Wilson, T. L., Rood, R. T., 1994, ARA&A, 32, 191.
Wynn-Williams, C.G., Becklin, E.E., Neugebauer, G., 1972, MNRAS, 160, 1.
Zhang, Q., Ho, P. T. P., Ohashi, N., 1998, ApJ, 494, 636.

Chapter 5 Summary and Future Work

5.1 The Zeeman measurements using SO(1_0-0_1) trasition

In the first part of the thesis (Chapters 2 and 3), a complete procedure in performing Zeeman observations was presented. In chapter 2, dense star-forming regions were explored with the aid of two low-J SO transitions. In the SO(1_0-0_1) survey, we successfully showed that in star-forming regions the low-J SO transitions are often related to the cold dense regions interacting with outflowing gas. The physical conditions towards nine star-forming regions were investigated by rotational diagrams and an LVG analysis. After selecting the best candidates and locating the best positions from the survey, in chapter 3, the SO(1_0-0_1) 30 GHz transition was used as a means to probe the magnetic fields towards the DR21(OH) and Orion B regions via the Zeeman effect. To our knowledge, this was the first attempt to perform the Zeeman measurements with this transition. Though we have obtained persuading hints for the detection of the Zeeman effect towards the DR21(OH) region after 45.5 hours integration on source, we cannot identify the originating cloud with the magnetic field strength of -2.1 ± 1.2 mG (the error is given in 3σ). The SO line profile and the magnetic field strength were different from the only previously existing successful Zeeman measurement towards DR21(OH), using the CN radical. The two transitions probably trace different parts of the clouds. Towards the Orion B region, no magnetic field was detected. An upper limit of 350 μG was derived.

The beam squint effect in the measurements was reduced to a very low level, but the noise source in the new 1-cm Zeeman receiver should be investigated at Effelsberg to improve the sensitivity of the system. Since the spectra of SO and CS are totally different from those of CO and CN towards the DR21(OH) region, high resolution interferometer maps of SO or CS should be obtained to have a closer view onto the DR21(OH) region. The only possible telescope to perform such high resolution measurement at 30 GHz will be the EVLA in the near future. Combining the results from the Zeeman and the polarization measurements, it will be possible to re-construct the three-dimensional magnetic field structure of the source. This will be a powerful tool to investigate the importance of magnetic fields in the star-forming process. In the future, more efforts are needed to prove that the SO 30 GHz transition is a promising tool for Zeeman observations.

5.2 CO(4-3) and CI($^3P_1$-$^3P_0$) observations on W51 region

In the second part of this thesis, W51 data observed with CHAMP were presented. The CHAMP array was built to perform high quality and high efficiency mapping for the CI($^3P_1$-$^3P_0$) and CO(4-3) lines. The structure of the W51 GMC is very complicated. With the aid of the CO(4-3) data, we successfully separated the complicated velocity structure into at least four velocity components. The CO(4-3) line is highly optically thick and traces the warm parts of the clouds. Towards W51**d**, the kinetic temperature is constrained between 65 to 80 K and CO column density between 1 to 2.5 × 10^{19} cm^{-2} using LVG with CO(4-3) and ^{13}CO(3-2) data for $n(H_2) = 10^4$ to 10^5 cm^{-3}. We found a new feature near W51**d**/**e** HII regions in the CO(4-3) map. It is along the edge of the dense region W51**e1**/**e2** and might be entirely due to optical depth effects. On large scales we found similar morphologies for CO(4-3) and ^{13}CO(1-0) towards the W51 region. This is probably due to the high opacity of the CO(4-3) transition, therefore the critical density of the CO(4-3) transition is lowered and is comparable to that of the ^{13}CO(1-0) transition.

The CI emission is strong at the northern and eastern sides of the cloud, whereas at the western and southern side of the cloud, the CI emission is weak and diffuse. On small scales the spatial distributions of the ^{13}CO(1-0) and CI lines are very similar towards the dense regions, but the resemblance between CI and ^{13}CO(1-0) is not as striking as in many well-known cases, probably because along the line of sight not all the observed clouds are in PDRs. This is likely also the reason why the abundance of atomic carbon derived from the whole velocity range (v = 45 to 75 km/s) is low. Cosmic ray ionization and the radiation field from the embedded cluster of young massive stars are probably the source of the observed atomic carbon, but PDR models with clumpy structure cannot explain the high atomic carbon column densities found deep in the cloud cores. Towards these very dense regions, a time-dependent chemical model was applied to explain the high column densities. At other positions with lower densities, the results are in good agreement with the calculation using the parallel layer PDR models by Hollenbach et al. (1991).

The results show the high potential of the CHAMP receiver in observing the 625 μm atmospheric window. New quantitative calculations with PDR models can later be used to investigate the physical conditions of the molecular clouds. ^{13}CO(2-1) data are urgently needed for a better understanding the PDRs towards the W51 region. Later CHAMP will be upgrated to a 2 x 7 pixel array in the 690 and 810 GHz atmospheric windows and it will be moved to the Atacama Pathfinder Experiment (APEX). With more data from other transitions, more constraints can be given towards the W51 region. Because of the complicated kinematics of the region, data have to be interpreted with great care.

Acknowledgements

This work was written in the Max-Planck-Institut für Radioastronomie between September 2000 and September 2003. I would like to thank the director Prof. Dr. K. M. Menten to give me the opportunity to study in Bonn. I would like to show my gratitute to Prof. Dr. Y.-N. Chin and Dr. J. Kerp for their help before and after my arriving Germany. Without them, the work would never start.

I would like to thank particularly Dr. R. Güsten and Dr. D. Muders for all the help and discussion in the study. Rolf always pointed out the exact problems and provided helpful ideas when I met difficulties. His great experience in both science and instrumentation has guided me to the cores of these two field in radio astronomy. Dirk was always ready to discuss with me and the discussion always helped me to elaborate my thoughts. His patience and kindness encouraged me in these three years. Without Dirk, the work would never be started nor be finished.

I would like to thank Dr. C. M. Walmsley for his advice for the thesis. I really learned a lot from him as a scientist. Many thanks to Dr. C. Henkel, too, for his kindly help in the last months of the work. I want to also thank Dr. Mattes, Hösgen, Pilz, Meyer, Lambertz, Tuerk and Schäfer in the Microwave Laboratory and Lochner at the telescope in Effelsberg. Without their help and experience, the work would not be done in such a short time.

As a foreign student in Germany, MPIfR and the region Bonn/Köln provided a friendly environment to start a new life and to live within. I want to express my thanks to all the friends here for their accompanying in the three years, no matter we met regularly or just knew each other by face. Therefore I am sorry that I cannot list all your names here. An end always means another beginning. Thanks that you have brought me so many beautiful memories.

致謝

這篇論文的完成代表著德國三年生活其中一部份，也可能是最重要一部分的總結。從出發前聯絡準備至今，這本論文今天能呈現在大家眼前，對我而言代表的除了是自己在學術上成長的軌跡之外，其實也隱含著無數人的幫助。除了感謝 MPIfR Prof. Dr. K. M. Menten 提供我到德國研究的機會，以及秦一男教授與 Dr. J. Kerp 的協助，讓我能夠在萊茵河邊度過這三年之外，Dr. R.Güsten 與 Dr. D. Muders 這三年來在學術上給予我無數的幫助與指引，以及 Dr. C. M. Walmsley 與 Dr. C. Henkel 在論文上的建議，他們的耐心讓我一個非天文科系出身的學生能夠在短時間之內慢慢熟悉電波天文這個領域，我希望能夠在此表達我與他們的付出來說極為微薄的謝意。

在此其實我特別想要表達的是對同樣懂中文朋友的謝意，無論我們是本就熟識還是是在這塊陌生的地方才有機緣深交，是曾經慢慢淡入又淡出彼此的生活或是持續穩定的支持，這幾年從你們的身上我學到了太多，也對自己心中的平衡有了更清楚的認識。

最後要特別謝謝住在 Essen 的雅芬與表姐夫 Herbert。是這麼多親情與友情的支持，才讓我有機會慢慢在學術的領域裡慢慢成長。